1-1-2014

Large-Angle Beamstrahlung: Simulation And Diagnostics

Ryan Stephen Gillard
Wayne State University,

LARGE-ANGLE BEAMSTRAHLUNG: SIMULATION AND DIAGNOSTICS

by

RYAN S. GILLARD

DISSERTATION

Submitted to the Graduate School

of Wayne State University,

Detroit, Michigan

in partial fulfillment of the requirements

for the degree of

DOCTOR OF PHILOSOPHY

2014

MAJOR: PHYSICS

Approved by:

_____

Advisor Date

_____

_____

_____

_____

ACKNOWLEDGEMENTS

I would like to thank my advisor Professor Giovanni Bonvicini for helping me in all of my research over the last four years and with my dissertation editing. I'd also like to thank my colleague and friend Hussein Farhat who worked side by side with me for much of this research. Additionally, a big thank you to all of my family and friends for their love and support throughout this whole process. Lastly, I'd like to thank my wife Ann for everything she has done for me.

TABLE OF CONTENTS

LIST OF TABLES

LIST OF FIGURES

Chapter 1 : Introduction

1.1 The Standard Model

Currently we understand the Universe as having four fundamental forces that control everything that happens. There is the gravitational force, the electromagnetic force, the weak force, and the strong force. The Standard Model is a quantum field theory concerning elementary particles and their interactions which together comprise the latter three forces. Work is being done to reconcile the Standard Model with our current theory of gravity, but that will not be covered here. Most of the Standard Model was conceptualized and tested for the last half of the 20^{th} century. It began in the 1960s with the quark model [1], their mixing, and a model that combined the electromagnetic and weak forces into something called the electroweak force which uses an SU(2) X U(1) gauge symmetry model [2][3][4]. This model had two generations of quarks and leptons and their force carrier particles called bosons which will be discussed in the next section. In the 1970s Quantum Chromodynamics was formulated as an SU(3) gauge symmetry theory [5][6] and later the model was adapted to have a third generation of fermions from discovery of the bottom quark and τ lepton. It wasn't until the 1990s that the last quark that we know of so far was discovered, the top quark. The τ neutrino also was observed as well as CP-violating observations for mesons that contain a bottom quark [7]. The very last prediction of the Standard Model to be observed was that of the Higgs boson which was first observed in 2012. This particle is supposedly responsible for why some particles have mass.

1.2 Fundamental Particles

The world we know is composed of many different types of particles, however they can be classified into groups. The main two groups are fermions and bosons which have a half-integer spin and an integer spin respectively. Fermions can be split into quarks and leptons. Combinations of quarks are called hadrons and can also be subdivided into two other groups; mesons that are comprised of two quarks or baryons which are comprised of three quarks. Bosons mediate the interactions between the other particles. Figure 1.1 contains a detailed table of the current Standard Model elementary particles.

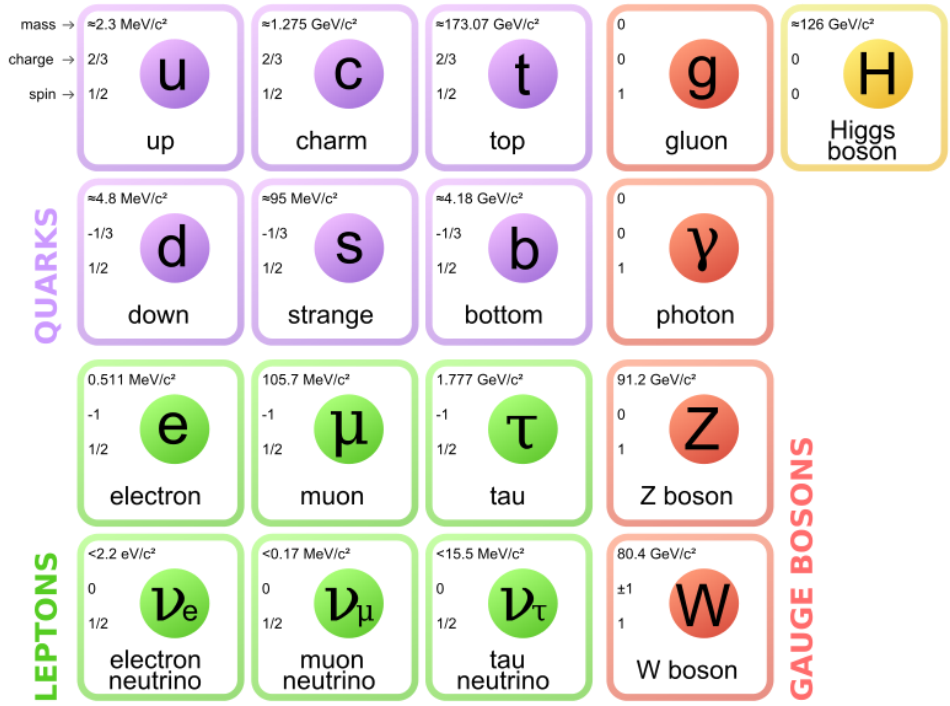

Figure 1.1: The Standard Model of Elementary Particles

1.2.1 Fermions

As mentioned there are two types of fermions: quarks and leptons. Fermions all have half-integer spins and an antiparticle that has the same mass as the particle but opposite electric charge. Quarks are what make up protons, neutrons, and most other important particles. There are six flavors of quarks split into three generations. The first generation contains the up and down quark which are the two lowest mass quarks. The second generation contains the charm and strange quarks and the third generation contains the top and bottom quarks. The up, charm, and top quarks all have an electric charge of +2/3 e and have an isospin direction of up and the down, strange, and bottom quarks all have a electric charge of -1/3 e and an isospin direction of down. Quarks also have a color charge from the strong force which is traditionally labeled as red, green, and blue. Only colorless quark combinations are meta-stable which means that red, green, and blue have to add up the correct way to produce a colorless product. Combinations of quark-antiquark pairs are called mesons and combinations of three quarks are called baryons which make up most of the matter we know. An example of a meson is the pion which has a wave function of $|d\bar{u}\rangle$. The proton is a baryon with the wavefunction $|uud\rangle$ whereas $|\bar{u}\bar{u}\bar{d}\rangle$ is the wavefunction for an antiproton which is an antibaryon. There are theories of other quark combinations such as a pentaquark or a fourth generation [8] but that is beyond this discussion. The energy needed to separate two quarks is much greater than the rest of energy of the quark. Therefore as soon as the quark starts getting pulled away it creates new quarks and antiquarks along the strong force field lines. This inability to isolate a quark is known as quark confinement.

There are two types of leptons; those with electric charge and those without. The uncharged leptons are called neutrinos and have very little mass and are associated with a corresponding charged lepton. For instance, the electron neutrino is in the same generation as the electron and the electron's antiparticle the positron. There is also the muon neutrino which is associated with the muon and the tau neutrino which is associated with the tau. As you can see, just like for quarks there are three generations of leptons and just like for quarks each generation is of a higher mass.

1.2.2 Bosons

Unlike fermions, bosons have integer spin. Bosons are the force mediators of the Standard Model. In other words, they are the particles that facilitate the interactions between the other particles of the Standard Model. The photon is the massless force carrier for the electromagnetic interaction. The weak force has the massive W and Z bosons and the strong force is meditated by gluons. All of these are spin 1 gauge bosons. The Higgs boson however has spin 0 and is responsible for the mass of some particles. Just like fermions, bosons have antiparticle pairs. The photon, gluon, and Z are their own antiparticles whereas the W- is the antiparticle of the W- where the mass is the same but the electric charge is opposite as with fermions. Bosons not only interact with fermions such as quarks and leptons but also can interact with themselves such as several gluons. The interactions of the Standard Model are conventionally drawn as Feynman Diagrams and a table of them all is in Figure 1.2.

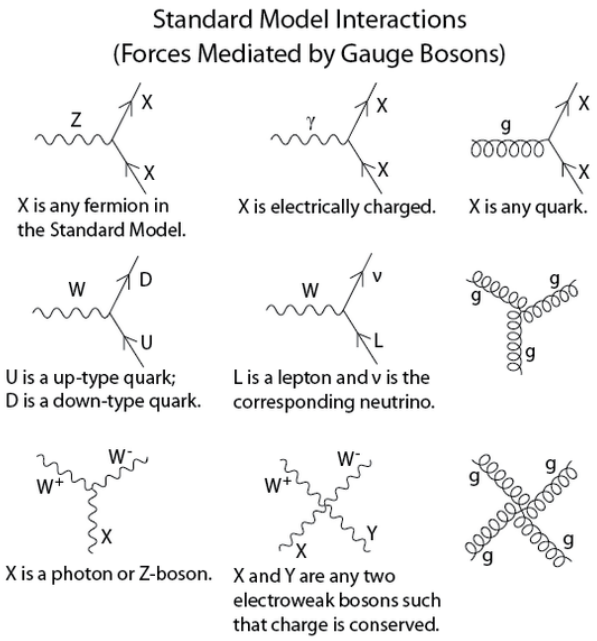

Figure 1.2: Interactions of the Standard Model

In Feynman Diagrams particles interact where they meet at a vertex. External lines only have one end meeting at a vertex and internal lines called propagators have a vertex at both ends of the line. As mentioned there are interactions of fermions and a boson such as in the five diagrams and there are interactions between multiple fermions and bosons in the next four diagrams such as the quadruple gluon interaction in the last diagram.

1.3 Symmetries

When there are physical quantities that are conserved, there is usually an underlying symmetry responsible for this behavior [9]. There are two main types of symmetries; continuous and discrete. A continuous symmetry's invariance remains after a continuous change in the geometry of the system and are mathematically represented as continuous or smooth functions.

On the other hand, a discrete symmetry's invariance remains after non-continuous changes in the system's geometry. This usually happens by a type of swapping called interchanges. A table of different symmetry classes, their invariances, and their conserved quantities is shown in Table 1.1.

Symmetry Class	Symmetry Invariance	Conserved Quantity
Continuous	Translation in Time	Energy
	Translation in Space	Linear Momentum
	Rotation in Space	Angular Momentum
Discrete	C, Charge Conjugation	Charge Parity
	P, Parity	Spatial Parity
	T, Time Reversal	Time Parity

Table 1.1: Symmetries, Invariances, and Conserved Quantities

In particle physics, many of the interactions happen at discrete points of space-time therefore we focus on the three discrete types of symmetry invariance. This is because the Standard Model describes local properties and not global ones. Parity is either -1 or +1, named odd or even respectively, and is determined by the associated operator acting on the wavefunction. Charge conjugation is simply the change of sign of a electrical charge of a particle. This would be its anti-particle since it has the same mass, just opposite charge. Spatial parity happens when we interchange the position vector $\mathbf{r}$ with the parity flipped position vector $-\mathbf{r}$. This is from a switching of direction of axes and is like a mirror image. Lastly, time parity comes about when the direction of time is reversed so rather than time running forward, instead we run time backward.

With our current understanding, the parities are conserved in the electromagnetic and strong interaction however in the weak interaction they are maximally broken [10][11]. Performing composite parities such as CP normally restores the symmetry for weak interactions but even then some particle interactions still have broken symmetry which is termed CP violation. One composite parity however seems to satisfy all interactions which is the combination of C, P, and T into CPT symmetry. CP violation in some select weak interactions is currently a hot area of scientific research and the overarching reason research. It is the proposed explanation for baryonic matter in the universe and not just pure radiation. In other words, it is a possible reason for why there is an extremely larger abundance of matter in the universe over antimatter. Therefore it is a very important research topic that can be studied at particle accelerators. The particle accelerators in turn need to function optimally to increase the chance of discovery which can be aided using our simulations and optics box.

1.4 Accelerators and Colliders

Many fields can benefit from having high energy particles ranging from nuclear and particle physics experiments, medical treatments, materials research, and industrial applications. An accelerator uses electric and magnetic fields to accelerate charged particles such as protons, electrons, and positrons. Neutrally charged particles like atoms cannot be accelerated this way therefore they are usually transformed into electrically charged ions by either adding or subtracting electrons.

A subset of particle accelerators are known as particle colliders which not only accelerate charged particles but then smash them into things. Most of nuclear and particle physics

experiments use these to see how the universe works at a level our most powerful microscopes are blind to. To do this we need to smash particles together at very high energy, gather data from the aftermath, and the reconstruct the initial states.

There are two main types of particle colliders: linear colliders and ring colliders. A linear collider like the one displayed in Figure 1.3 is a very long straight pipe surrounded by powerful magnets that accelerate a group of particles to extremely close to the speed of light until eventually the particles hit a fixed target.

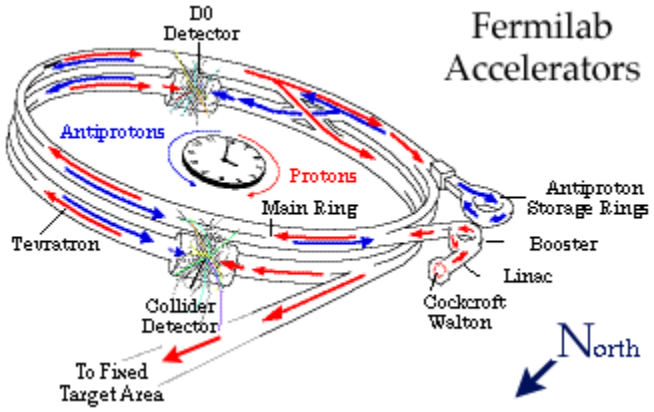

Figure 1.3: Fermilab Fixed Target Collider

This has the advantage of being able to have a large target that isn't moving therefore there should be a total collision easily.

A ring collider like the one shown in Figure 1.4 is a circular pipe with a very large radius surrounded by powerful magnets that bend two groups of accelerated particles in opposite directions to nearly the speed of light until finally the two groups of particles collide.

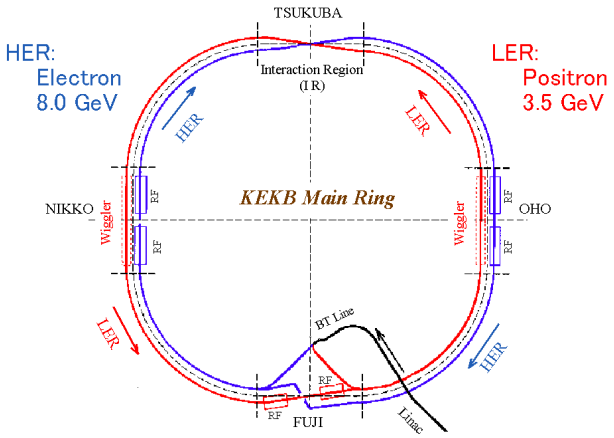

Figure 1.4: KEKB Ring Collider

Obviously it is much harder to make the two moving groups collide, however since both have very high energies the center-of-mass energy will be

$$E_{CM} = \sqrt{s} = \sqrt{2E_1E_2 + (m_1^2 + m_2^2)c^4 + 2\sqrt{E_1^2 - m_1^2c^4}\sqrt{E_2^2 - m_2^2c^4}} \approx 2\sqrt{E_1E_2} \qquad (1.1)$$

where E_1 and E_2 are the energies of the particles in the respective beams and m_1 and m_2 are the respective masses of the particles in each beam.

In a fixed-target collider however the target has no momentum in the lab frame so that when solving for E_{CM} the center-of-momentum energy will be smaller

$$E_{CM} = \sqrt{s} = \sqrt{2E_pm_tc^2 + \left(m_p^2 + m_t^2\right)c^4} \approx \sqrt{2E_pm_tc^2} \qquad (1.2)$$

where the Mandelstam variable $s = (p_1c + p_2c)^2$, E_p and m_p is the energy and mass of the accelerated particles, and m_t is the mass of the target. Note that since there is no momentum for the target that its energy is simply just $E_t = m_tc^2$. Also, if we assume that the energy of the particle is much greater than the mass of the particle and the target then the equation simplifies.

As you can clearly see, even though it is much easier to hit a fixed target, the energy required to achieve the same E_{CM} as a two moving particle collision is much higher. You can get much more center-of-momentum energy from the energy you've put into the particles in a collision.

$$\frac{E_{CM\ collision}}{E_{CMfixed}} = \frac{2E}{\sqrt{2Em_tc^2}} = \sqrt{\frac{2E}{m_tc^2}} \tag{1.3}$$

1.4.1 Accelerator Physics

There are many important steps that first have to happen before we can perform physics experiments with the beams of particles. First, we need to create and accelerate the beams. We then need to effectively maintain the beams in stable orbits. Lastly, we need to be able to manipulate the beams to our choosing such as squeezing them to very small scales.

The first point of business is in the creation of the beams. In our case we will need something to create a beam of electrons and something to create a beam of positrons that travel in the opposite direction of the electrons. This can be facilitated by a piece of complicated hardware called a linac. A linac is where the beams are created and then accelerated to almost their full speed until they are injected into the circulation rings. Figure 1.5 shows the schematic of KEKB's linac.

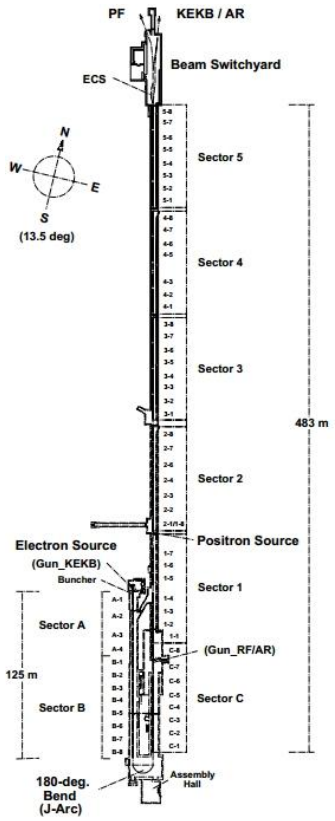

Figure 1.5: Linac at KEKB

The journey begins at a high voltage small metallic tip, the low emittance electron source, with a typical tip radius of 40 nanometers and a typical emitted solid angle of 1 square radian. The electric fields are extremely high for such a small area thus electrons are very easily pushed into a beam by applying pulsed fields to the tip. This beam eventually gets accelerated by RF cavities. An RF cavity is a conducting (warm) or superconducting (cold) metal can that contains a standing electromagnetic wave which is used to accelerate charged particles. The standing wave is timed in such a way that each bunch of particles passes through the cavity and is accelerated. The difference between warm and cold is the Q which is the cavity damping time expressed in number of oscillations. They are made of copper (Q values of order 10^4) for warm and niobium (Q values of order 10^7) for cold. All cavities at KEKB are cold. The cavity itself

dissipates little energy; virtually all of it goes to the beam. Most of the RF cavities for the entire machine are in the linac. There is only one RF cavity group per storage ring to compensate for energy lost during circulation. The beams see an oscillating voltage

$$V_0 \sin\left(2\pi\omega_{rf}t + \varphi_s\right) = V_0 \sin\left(\varphi_{rf}(t) + \varphi_s\right) \tag{1.4}$$

where V_0 is the voltage of the cavity, ω_{rf} is the angular frequency of the RF cavity, t is time, and φ_s is the phase angle with respect to the RF wave for a synchronous particle.

The cavity is set up so that the particle in the center of the bunch acquires an amount of energy equal to the synchrotron losses in the course of a revolution. This particle is called the synchronous particle. $\varphi_s = 0$ when there is no acceleration. Particles that arrive early see $\varphi < \varphi_s$ and get a decreased amount of energy and particles that arrive late see $\varphi > \varphi_s$ and get an increased amount of energy. Therefore, to accelerate we want to ensure that $0 < \varphi_s < \pi$ (for a positron at least) so that the synchronous particle of charge q in the center of the bunch gets a kick equal to

$$\Delta E = qV_0 \sin(\varphi_s) \tag{1.5}$$

Cavities are also used for bunching where particles can be sent through zero voltage so that particles in the back of the beam will be accelerated and particles in front decelerated so that the longitudinal phase space is compressed.

Some of the partially accelerated electron bunches are sent into a tungsten target where a shower of electrons and positrons is created. The positrons are magnetically selected, reinjected into the linac, and then accelerated as well as the electrons down the linac. Each of these two beams will continually get accelerated by further RF cavities. If the electrons get a forward kick at a certain point in the standing wave, then the positrons will get a forward kick when the

standing wave's phase has shifted 180 degrees. At the end of the linac is a series of magnets, shown in Figure 1.5 as the Beam Switchyard, that will divert the electrons one direction into their respective ring and the positrons in the opposite direction into a damping ring first, followed by their respective beam pipe ring. The positrons usually circulate for five damping times, with the damping time for a circular accelerator given by

$$\tau_{damping} = \frac{E}{\delta E}, \qquad \delta E(MeV) = 8.55 * 10^{-2} \frac{[E(GeV)]^4}{\rho(meters)} \tag{1.6}$$

where $E(GeV)$ is the energy of the beam and ρ is the radius of ring [12]. The purpose is to shed most of the transverse momentum before they enter their actual storage ring. Wiggler magnets are used to speed up the damping.

The damping ring has its own magnetic lattice of dipoles and quadrupoles with its own RF cavity. This makes the positron beam much more collimated and stable, whereas the electron beam already was collimated and stable, since creation by the sharp tip gives it a small emittance (defined below).

We now enter the main storage rings, where beams are stored for the duration. Ring accelerators don't usually use the normal *x*, *y*, and *z* orthogonal coordinate system. Instead they use an orbit coordinate system called Frenet-Serret as shown in Figure 1.6.

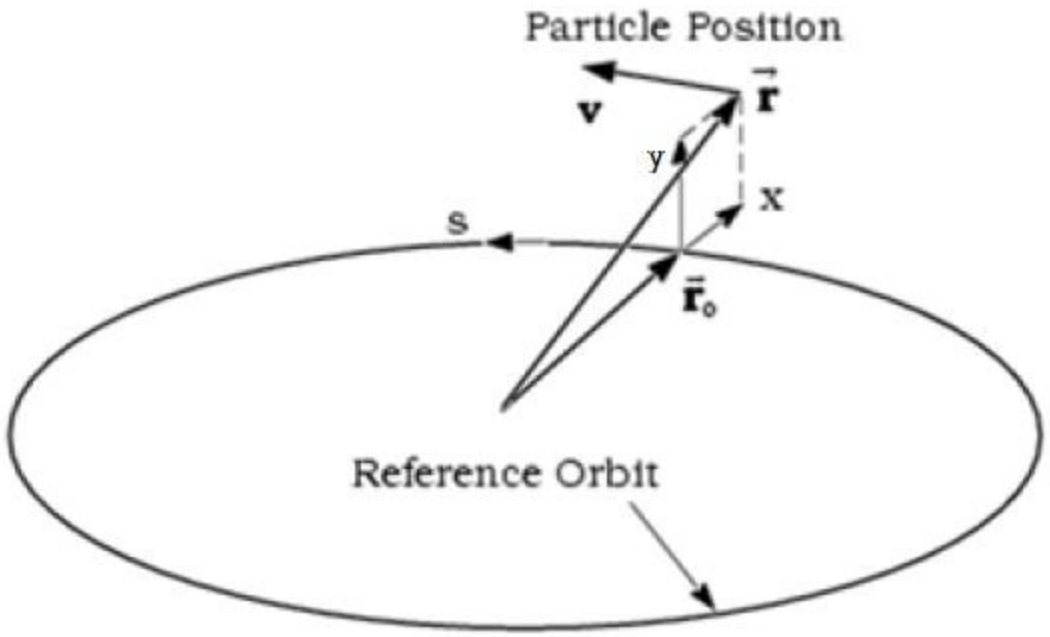

Figure 1.6: Frenet-Serret Coordinate System

The unit vectors of this (x, y, s) coordinate system [13] with reference orbit of radius $\boldsymbol{r_0}$ are

$$\hat{s}(s) = \frac{d\boldsymbol{r_0}(s)}{ds}, \qquad \hat{x}(s) = -\rho(s)\frac{d\hat{s}(s)}{ds}, \qquad \hat{y}(s) = \hat{x}(s) \times \hat{s}(s) \tag{1.7}$$

Now that our beams are within the beam pipe it is very important to make the beams stable. There are three types of magnets arranged in lattices around the rings. Dipoles are used in the curved sections to bend the beam, quadrupoles are used to focus the beam, and sextupoles are used to fix any chromatic errors. There is a large quantity of corrector magnets which are just weaker and smaller versions of the regular magnets for fine tuning and correcting.

When a beam is leaving the straight section of the ring and comes to a turn it needs to bend around the curve or it will strike the beam pipe and will be lost. Dipoles serve this function

and act like a prism. However, just like a prism the beam won't be bent the same amount at all points which can lead to difference in momentum which will need to be corrected by sextupoles.

The storage ring is somewhat like an optical fiber, a device to guide particles over long lengths. In our case we want the beam to remain in circulation well inside the beam pipe in a stable orbit. Quadrupoles act as a lens for charged particles with the ability to focus along one transverse dimension and defocus along the other. Quadrupoles are usually arranged in lattices of triplets with the same two focusing on either end and a defocusing for that dimension in the middle. The triplet arrangement has the crucial property of focusing in both transverse dimensions, effectively maintaining the beam close to the stable orbit and inside the beam pipe. Sextupoles such as shown in Figure 1.7 correct chromatic effects.

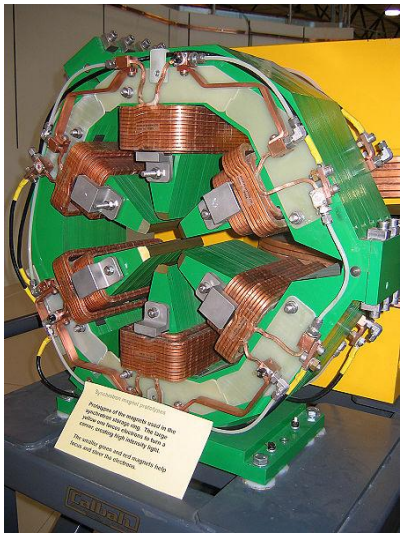

Figure 1.7: Sextupole Magnet

The evolution of the particle beams through the lattice of magnetic elements can be described by the transfer matrix M such that [13]

$$\begin{pmatrix} x_1 \\ x_1' \end{pmatrix} = M \begin{pmatrix} x_0 \\ x_0' \end{pmatrix} \tag{1.8}$$

where the final state $\begin{pmatrix} x_1 \\ x_1' \end{pmatrix}$ is the transfer matrix M multiplied with the initial state $\begin{pmatrix} x_0 \\ x_0' \end{pmatrix}$. Here x' is the angle in the (x, s) plane between the particle trajectory and the s-axis. The true form of the transfer matrix is complex, requiring six dimensions. For the x-component phase space only, the transfer matrix for a pure sector dipole is [13]

$$M_x(s, s_0) = \begin{pmatrix} \cos(\theta) & \rho \sin(\theta) \\ -\frac{1}{\rho}\sin(\theta) & \cos(\theta) \end{pmatrix}. \tag{1.9}$$

The orbiting angle is defined as $\theta = \frac{l}{\rho}$, l being the length of the dipole and ρ being the bending radius.

Quadrupoles have focusing function K and length $l = s - s_0$. The transfer matrix for a focusing quadrupole is [13]

$$M(s|s_0) = \begin{pmatrix} \cos(\sqrt{K}l) & \frac{1}{\sqrt{K}}\sin(\sqrt{K}l) \\ -\sqrt{K}\sin(\sqrt{K}l) & \cos(\sqrt{K}l) \end{pmatrix} \tag{1.10}$$

whereas the transfer matrix for a defocusing quadrupole is

$$M(s|s_0) = \begin{pmatrix} \cosh\left(\sqrt{|K|}l\right) & \frac{1}{\sqrt{|K|}}\sinh\left(\sqrt{|K|}l\right) \\ \sqrt{|K|}\sinh\left(\sqrt{|K|}l\right) & \cosh\left(\sqrt{|K|}l\right) \end{pmatrix}. \tag{1.11}$$

The transfer matrix for drift space is defined as

$$M(s|s_0) = \begin{pmatrix} 1 & l \\ 0 & 1 \end{pmatrix}. \tag{1.12}$$

In the thin-lens approximation where $l \to 0$, the quadrupole transfer matrices become

$$M_{focusing} = \begin{pmatrix} 1 & 0 \\ -\frac{1}{f} & 1 \end{pmatrix} \tag{1.13}$$

$$M_{defocusing} = \begin{pmatrix} 1 & 0 \\ \frac{1}{f} & 1 \end{pmatrix} \tag{1.14}$$

where f is the focal length given by $f = \lim_{l\to 0} \frac{1}{|K|l}$.

The quadrupoles induce transverse oscillations called betatron motion. Longitudinal oscillations are called synchrotron motion.

The number of betatron oscillations in one revolution of an accelerator of circumference $C = PL$, where P is the number of identical superperiods and $P\Phi$ is the phase change per revolution, is called the betatron tune and is [13]

$$Q_x = \nu_x = \frac{P\Phi_x}{2\pi} = \frac{1}{2\pi}\int_s^{s+C} \frac{ds}{\beta_x(s)} \tag{1.15}$$

for the x direction and is

$$Q_y = \nu_y = \frac{P\Phi_y}{2\pi} = \frac{1}{2\pi}\int_s^{s+C} \frac{ds}{\beta_y(s)} \tag{1.16}$$

for the y direction. Quadrupole magnets provide the restoring force for these betatron oscillations.

It is very important that the two transverse tunes not be integer, half-integer, or even a simple fraction since this, coupled with lattice imperfections, would excite resonances that would cause beam loss. Furthermore, it is important that Q_x and Q_y are related by a real number so that the x and y oscillations won't be highly correlated.

The longitudinal motion on the other hand known as synchrotron motion has its own tune called synchrotron tune and is [13]

$$Q_s = \sqrt{\frac{heV|\eta_0 \cos(\varphi_s)|}{2\pi\beta^2 E}}. \tag{1.17}$$

where h is the harmonic number, e is the elementary charge, V is the RF cavity voltage, $\eta_0 = \gamma^{-2} - \gamma_{transition}^{-2}$, φ_s is the phase angle with respect to the RF wave for a synchronous particle, β is the velocity of the particle divided by the speed of light, and E is the energy of the particle. We also want this tune to be a real number to avoid resonances.

At KEKB, the beam lifetimes are on the order of tens of minutes which is a very long time to maintain beams after hundreds of millions of revolutions. At SuperKEKB, the beam lifetimes are much shorter therefore the beams only make around six million revolutions. The lifetime of the beam is defined as

$$\frac{1}{\tau_{Lifetime}} = \frac{1}{\tau_{Beam\ gas}} + \frac{1}{\tau_{Touschek}} + \frac{1}{\tau_{Beam-beam}}. \tag{1.18}$$

The three right hand terms describe different effects that can kick a particle off the nominal orbit and into the beam pipe, where it will suffer catastrophic energy loss and be lost. Beam gas lifetime is due to inelastic scattering with the residual gas, which is mostly degassed by the metal beam pipe as it is hit by synchrotron radiation X-rays. The Touschek effect is due to intra-beam scattering (Moller scattering). This dominates at SuperKEKB. The Touschek effect is inversely proportional to the volume of the beam. The more tightly packed the beam is, there will be a greater chance for interactions. The resulting Moller scatterings are at low momentum transfer, and most particles return to the nominal orbit eventually. The beam pipe is smaller at the interaction point and the biggest losses will be near the Interaction Region. The

last term is from repeated deflections in the same direction when one particle crosses the other beam. This effect dominated at KEKB. To make up for these losses, extra particles are continuously injected into depleted bunches of each beam at precise times.

Transverse emittances are a property of the machine. They define the total phase space occupied by the particle population in the transverse dimensions. They are for the horizontal and vertical dimensions [13]

$$\varepsilon_x = \sqrt{\sigma_x^2 \sigma_{x'}^2 - \sigma_{xx'}^2} \tag{1.19}$$

$$\varepsilon_y = \sqrt{\sigma_y^2 \sigma_{y'}^2 - \sigma_{yy'}^2} \tag{1.20}$$

where σ_u and $\sigma_{u'}$ are, respectively, the spatial transverse width and angular width, and $\sigma_{uu'}$ is the correlation. At the interaction point, ideally we want the correlation to be zero. The emittance tells us how spread out and disordered our beams are. If the entire beam can be made exactly parallel to the beam line then there is zero emittance. Low emittance will not only let us more easily confine the beam within the beam pipe but it also allows for a higher luminosity (defined below) since the particles are more tightly packed into a bunch.

Beam size σ and emittance ε are related through the beta function, which describes the local oscillation frequency around the nominal orbit, in the transverse plane. For example, in the horizontal direction

$$\beta_x(s) = \frac{\sigma_x^2}{\varepsilon_x} \tag{1.21}$$

There is a beta function everywhere along the ring but at the interaction point the beta function is given the special name β^*. This is much smaller than the beta function elsewhere in

the beam pipe. We use the beta function and emittance to find the beam widths and then use those beam widths to find things such as the luminosity which will be covered in the next section. The longitudinal phase space (along s) is dealt with differently because it is affected by different phenomena, such as quantum fluctuations in synchrotron radiation emission.

Bunches are stored in stable longitudinal regions called buckets as they oscillate ahead and behind the nominal particle. The symplectic mapping equation that realistically describes the synchrotron motion and can be used to find the bucket regions [13] is

$$\delta_{n+1} = \delta_n + \frac{eV}{\beta^2 E}(\sin(\varphi_n) - \sin(\varphi_s)) \tag{1.22}$$

$$\varphi_{n+1} = \varphi_n + 2\pi h\eta(\delta_{n+1})\delta_{n+1} \tag{1.23}$$

where δ is the off-momentum coordinate and φ is the rf phase. The mapping conserves phase space area since the Jacobian of the mapping to $(\varphi_{n+1}, \delta_{n+1})$ from (φ_n, δ_n) equals 1.

1.5 B-Factories

The specific type of collider where we work is called a B-factory and specializes in producing B mesons in the order of billions which can then be analyzed in great detail. A similar number of tauons and D mesons also are produced leading to possible analysis of their properties as well [14][15].

Back in the 1990s, a B-factory in Japan and a B-factory in the U.S. were developed and both were based around electron-positron collisions. They mainly focus on center of mass energies around the $\Upsilon(4S)$ resonance peak. An upsilon, Υ, is a meson formed from the combination of a bottom quark and its antiparticle into $b\bar{b}$. It was discovered at Fermilab outside

Chicago, IL in 1977 and was the first particle that contained a bottom quark. This was due to the fact that it is the lightest that can be produced without the need for heavier particles. Tuning the accelerator energy can create the resonances or excited states as shown in Figure 1.8.

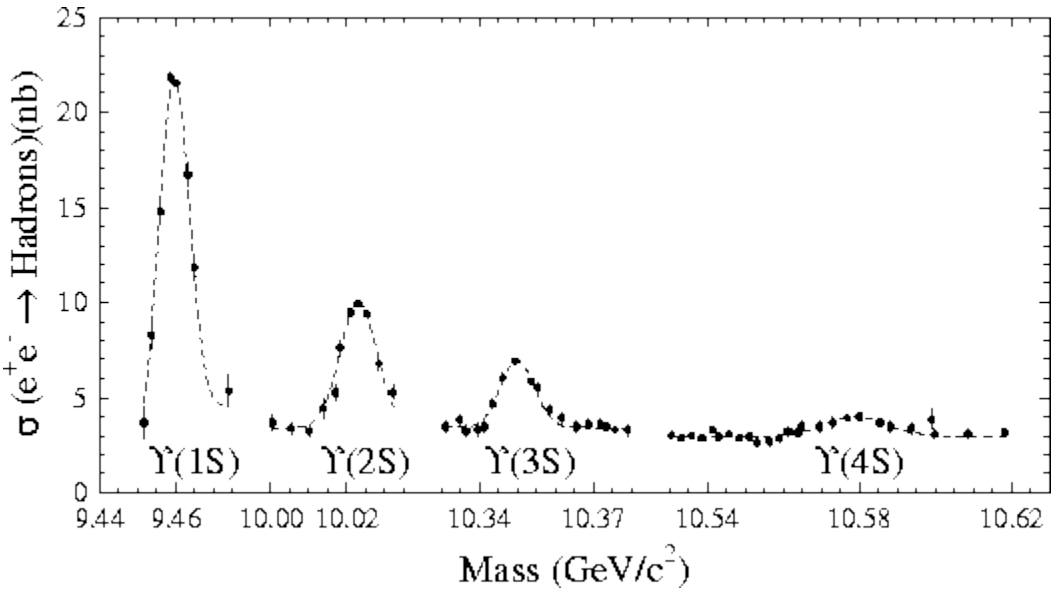

Figure 1.8: Upsilon System Resonances

We focus on the 4S resonance since the 1S, 2S, and 3S resonances only decay by the bottom and antibottom quarks annihilating. However, at the 4S resonance there is just enough energy to create a light quark/antiquark pair thus being able to produce a pair of B mesons which will decay into what we are interested in.

The B-factory in the U.S. was in California at the SLAC laboratory where the BaBar experiment at the PEP-II collider finished gathering its data in 2008. The B-factory in Japan is in the Tsukuba area where the Belle experiment at the KEKB collider completed its data in 2010.

From the gathered data from both experiments there was the first discovery of CP violation in the B system. Previously, there was only CP violation found in the K system. Figure 1.9 shows the number of events per time on the left and the raw asymmetry on the right.

The peaks in the graph on the left should be superimposed on each other if CP is not violated but as you can see there is a lack of symmetry between the two peaks. If there was no asymmetry the graph on the right would be a horizontal line at 1.

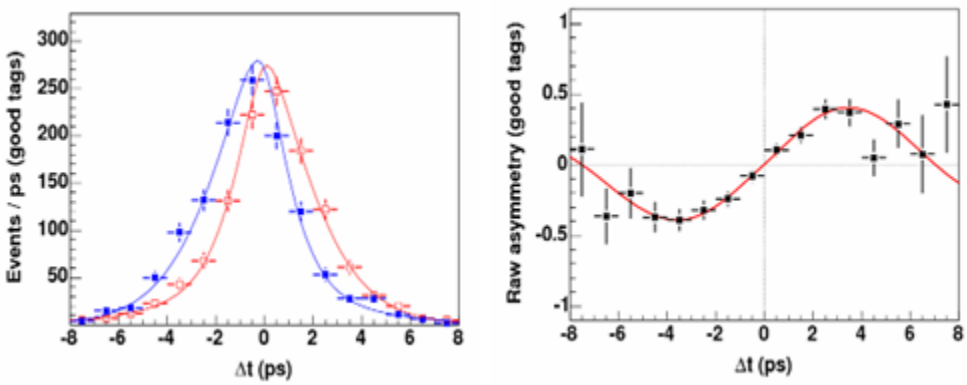

Figure 1.9: CP Violation Discovered at KEKB and PEP-II

The experiments also provided measurements of the CKM matrix parameters rho and eta.

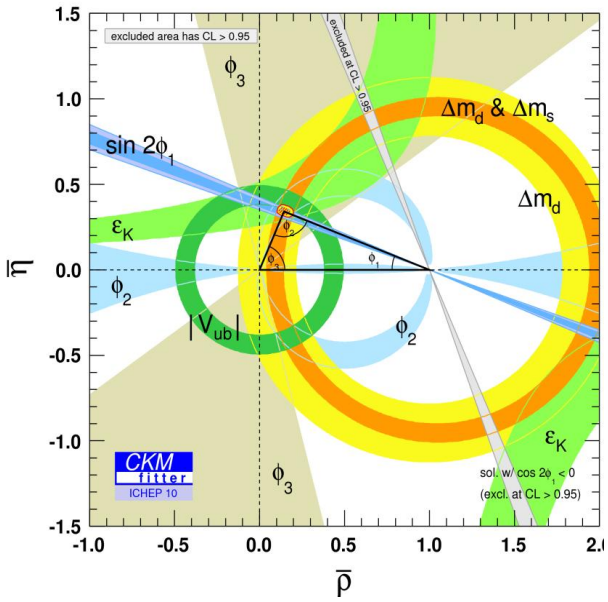

Figure 1.10: Rho and Eta Parameters for CKM Matrix

The CKM or Cabibbo–Kobayashi–Maskawa matrix contains the information that relates the strength of weak decays [16]. Specifically it comes from the mismatch between mass eigenstates and weak eigenstates [17].

$$\begin{bmatrix} d' \\ s' \\ b' \end{bmatrix} = \begin{bmatrix} |V_{ud}| & |V_{us}| & |V_{ub}| \\ |V_{cd}| & |V_{cs}| & |V_{cb}| \\ |V_{td}| & |V_{ts}| & |V_{tb}| \end{bmatrix} \begin{bmatrix} d \\ s \\ b \end{bmatrix} \tag{1.24}$$

Figure 1.11 shows the full reconstruction method of the final events leading back to the original $\Upsilon(4S)$ from the electron-positron collision.

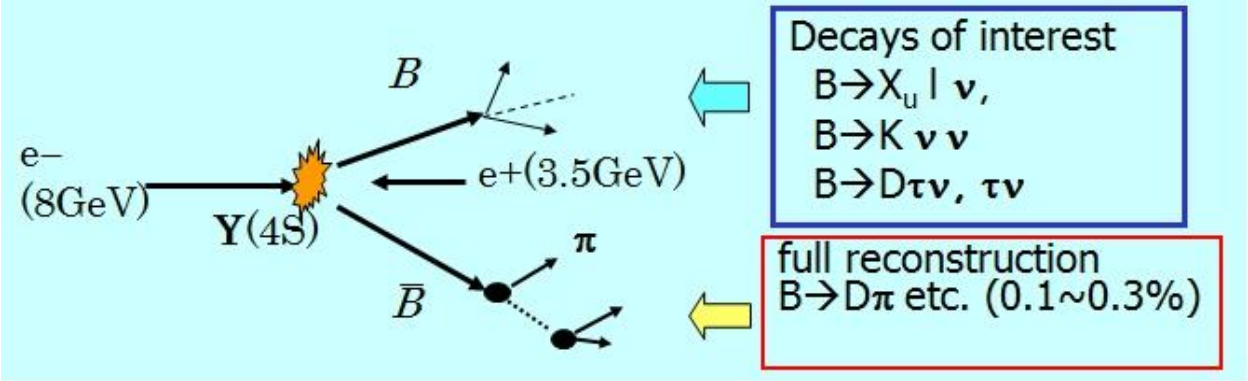

Figure 1.11: Full Reconstruction Method

The next generation of B-factories is currently underway. There was supposed to be one built in Frascati, Italy near Rome called SuperB however it has since been cancelled. However, the most promising B-factory will be the upgrade of KEKB into SuperKEKB where Belle's successor Belle II will be placed.

Chapter 2 : SuperKEKB and the Belle II Experiment

2.1 KEKB, SuperKEKB, and Belle II

KEKB and the near future SuperKEKB are ring accelerators ran by Japan's High Energy Accelerator Research Organization known as KEK. As mentioned earlier it is located in Tsukuba, Ibaraki Prefecture, Japan. Each ring's circumference is 3016 meters with four straight sections and each ring is located 10 meters underground. Figure 2.1 shows an aerial photograph of the KEKB site with the beam piping outlined in green.

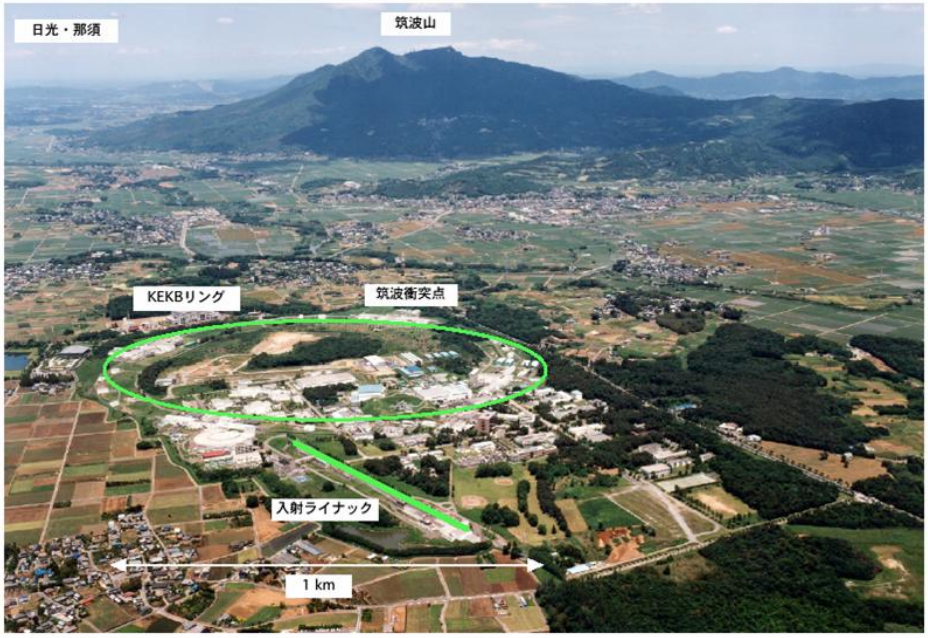

Figure 2.1: Aerial View of KEKB

KEKB/SuperKEKB is an asymmetric electron-positron collider meaning that the electrons will have a different energy than the positrons. These energies at KEKB were 8 GeV and 3.5 GeV respectively which gives a center of mass energy of 10.58 GeV. This asymmetry

allows the B meson pairs to be Lorentz boosted with $\beta\gamma = 0.425$. Therefore the distance they travel from the known collision point can aid in the measurements of their decay times.

There are two different rings that the particles travel through. The ring that houses the higher energy electrons is aptly named the high-energy ring or HER while the ring that houses the lower energy electrons is called the low-energy ring or LER. A diagram of the future SuperKEKB is shown in Figure 2.2.

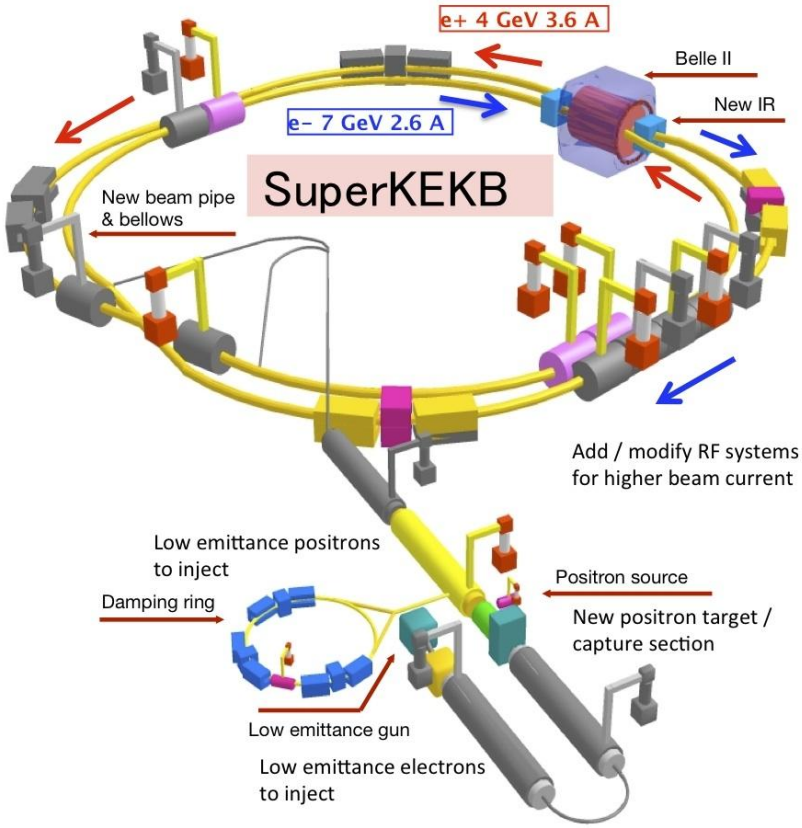

Figure 2.2: The New and Improved SuperKEKB

Note there is only one interaction point which will be at Belle II as shown above. In SuperKEKB, the electron beam will have energy of 7 GeV and the positrons will have energy of

4 GeV which still give a center of mass energy of 10.58 GeV therefore we will still be operating at the critical $\Upsilon(4S)$ resonance energy.

KEKB currently holds the world record for highest luminosity of 2.11×10^{34} cm^{-2} s^{-1}. Luminosity is the rate of particle production per unit interaction cross section. Therefore, the higher the luminosity a machine has the greater the statistics produced and the greater the chance for discovery.

The beam pipe is also getting an upgrade. A special coating of Titanium Nitride will be added to the inner surface of the beam pipe. This is one of the best degassing materials and should reduce residual gas inside the beam pipe. Also, large antechambers are added to the sides in the arcs to reduce any leeching from the metal by having any of the beam gas trapped inside of them rather than in the way of the revolving beams. A schematic of the new beam pipe is shown in Figure 2.3.

Figure 2.3: Upgraded Beam Pipe

The upgrade is also going to redesign the magnetic lattices in both the HER and LER beam pipes to squeeze the emittance even further to boost the luminosity as shown in Figure 2.4 below. In addition the short 1.2 meter dipoles in the low-energy ring will be replaced with longer 7 meter dipoles. With longer dipoles, the number of dipoles will be less in that section of pipe, thus there will be fewer fringe effects that cause imperfections.

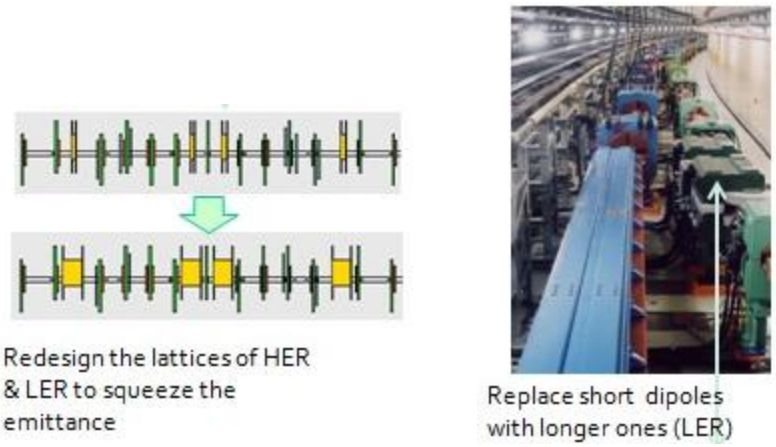

Figure 2.4: Upgrading Beam Pipe Magnets

The upgrades to KEKB to convert it into SuperKEKB are expected to boost the luminosity even further to $8x10^{35}$ cm^{-2} s^{-1}; almost 40 times greater. They plan on doing this by increasing the beam squeezing at the interaction point as shown in Figure 2.5 with much stronger superconducting magnets.

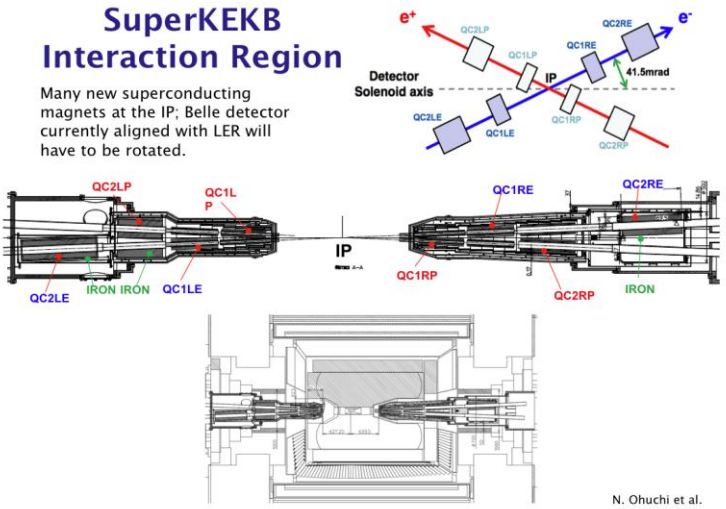

Figure 2.5: SuperKEKB's Interaction Region

The machine parameters of SuperKEKB are summarized in Table 2.1 below [18].

Quantity	HER	LER
Energy (GeV)	7	4
Luminosity $cm^{-2}s^{-1}$	$8*10^{35}$	
Circumference (m)	3016	
Beam current (A)	2.6	3.6
Beam population	$6.53*10^{10}$	$9.04*10^{10}$
Number of Bunches	2500	
Bunch separation (ns)	4	
Bunch length (mm)	5	6
Beta function @IP hor./ver. (mm)	25/0.30	32/0.27
Emittance (nm)	4.6	3.2
X-Y coupling (%)	0.28	0.27
Vertical beam size at IP (nm)	59	48
Horizontal beam at IP (μm)	10.3	7.75
Damping time: trans./long. (ms)	58/29	43/22

Table 2.1: SuperKEKB Machine Parameters

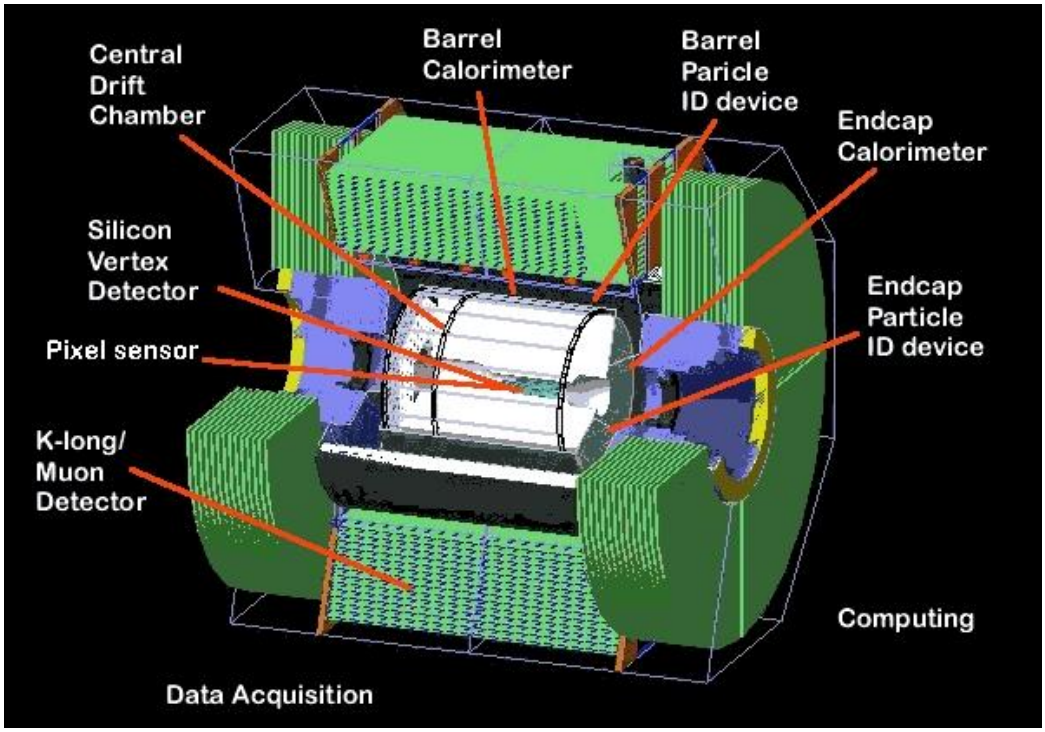

Figure 2.6: The Belle Detector

As shown above in Figure 2.6, Belle is a large multilayered detector that surrounds a solenoid. Each layer detects something different. The innermost layers capture certain events whereas other events pass through and deposit their signature in layers farther out. It has a large solid angle coverage from 17 degrees to 150 degrees. Its silicon vertex detector has a precision on the order of 10 microns of the vertex location. Its Cherenkov detector allows great pion-kaon separation for the momentum range of 100 MeV/c to a few GeV/c. Also, the CsI scintillating crystals used in its electromagnetic calorimetry have a precision of just a few percent. All of these pieces work efficiently together to study CP-violation and beyond and have lead to over 300 published papers in physics journals.

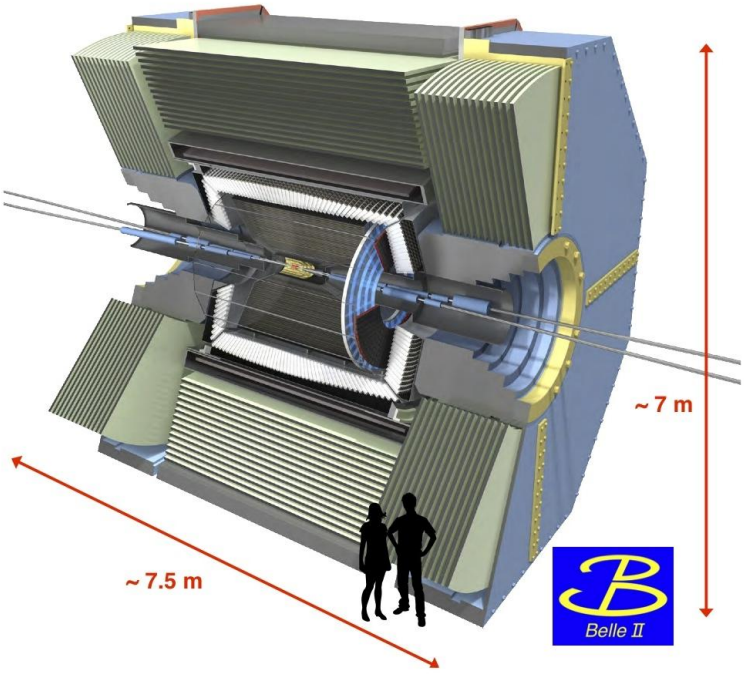

Figure 2.7: The Belle II Detector

Due to the much greater luminosity from the upgraded KEKB into SuperKEKB and thus many more events, Belle II, as shown above in Figure 2.7, is going to have to be upgraded as well. Optical fibers will be added to help increase the speed and throughput of the data acquisition. A new system will replace the trigger electronics and to improve resolution for particle tracking a pixel detector will be added. Also, to cover a larger solid angle there will be a new silicon vertex detector added in addition to a time-of-propagation chamber, a central tracking chamber, and an aerogel ring-imaging Cherenkov detector. In 2014, the first beam of SuperKEKB should happen and the physics runs should start in 2015.

2.2 Luminosity Optimization

In the world of particle physics, there are two methodologies concerning how to push the limits of our technology to discover new particles and confirm existing theories. The first method is to increase the center of mass energy of the beams, however this comes with its problems such as a greater loss of power and cost efficiency. The other method is to maximize the luminosity. To maximize the luminosity there are two methods as well. One involves increasing the beam currents and the other method involves making a large crossing angle and squeezing the beams to a nanometer scale. SuperKEKB will be increasing the beam currents slightly, increasing the crossing angle, and will squeeze the beams ever smaller. Figure 2.8 shows the difference between the beams at KEKB and the predicted beams at SuperKEKB when they collide with each other. Both beams are approximately Gaussian, but notice how the extreme focusing of the beams into hourglass shapes at SuperKEKB allows for a much higher interaction percentage thus leading to a great luminosity.

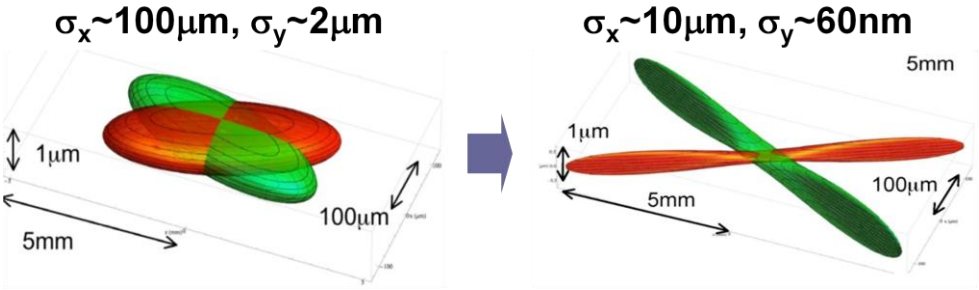

Figure 2.8: Our Electron-positron Beams Crossing, KEKB on Left, SuperKEKB on Right

We are working with a beam of electrons going around a very long circular pipe in the opposite direction of a beam of positrons in another pipe that cross at the interaction point. When the beams collide new particles can be produced and the rate of particle production per unit interaction cross section is the luminosity. The luminosity integrated over a second

therefore is the luminosity per collision times the number of collisions per second. Obviously, if we want to study new particles and their interactions we want to maximize this as best we can. Approximately 2500 bunches are going around the beam pipe at all times.

The formula for luminosity is

$$L = f|v_1 + v_2| \int \rho_1(x,y,z,t)\rho_2(x,y,z,t)dxdydzdt \tag{2.1}$$

which is a four-dimensional integral in $x, y, z,$ and t of both of the beam densities ρ_1 and ρ_2 with the collision frequency f being a constant outside the integral and the velocities v_1 and v_2 of the respective beams. To get the luminosity per collision, just divide by the collision frequency f. These densities can vary over time due to bending, small irregularities, or other small changes that build up over time; however we can ignore the dynamic changes from all of this for a good approximation.

The density function for the first beam in its rest frame is

$$\rho_1 = \frac{N_1}{(2\pi)^{\frac{3}{2}}\sigma_{\bar{x}_1}\sigma_{\bar{y}_1}\sigma_{\bar{z}_1}} e^{-\frac{1}{2}\left[\left(\frac{\bar{x}_1}{\sigma_{\bar{x}_1}}\right)^2+\left(\frac{\bar{y}_1}{\sigma_{\bar{y}_1}}\right)^2+\left(\frac{\bar{z}_1}{\sigma_{\bar{z}_1}}\right)^2\right]} \tag{2.2}$$

where N_1 is the number of particles in the first beam, $\sigma_{\bar{x}_1}$, $\sigma_{\bar{y}_1}$, and $\sigma_{\bar{z}_1}$ are the beam's rest frame rms widths, and $\bar{x}_1$, $\bar{y}_1$, and $\bar{z}_1$ are the first beam's rest frame coordinates. The density function for the second beam, ρ_2, is the same except all of the subscripts are changed from ones to twos. The beams are approximately Gaussian and modeled as such. During the interaction, the particles of one beam are bent by the electromagnetic field of the other beam, and the beams pinch each other, further modifying the luminosity. This is a relatively small effect, and the beams are considered rigid in the following. Let it be noted this equation fits much better the

KEKB scenario on the left in Figure 2.8, than on the right of Figure 2.8 with the SuperKEKB hourglass shapes. The hourglass effect will be covered later.

We will be working with beams on the order of $2 * 10^{10}$ particles with a low energy beam and high energy beam of 4 and 7 GeV respectively with laboratory rms beam widths around 10 μm for σ_x, 50 nm for σ_y, and 6 mm for σ_z. Looking at the approximate ratios of these you will find a 120,000:200:1 ratio for x, y, and z respectively. These are very long beams relative to the x and y directions that are very flat in the x-y plane like a very long, somewhat wide strip of paper as shown in Figure 2.9.

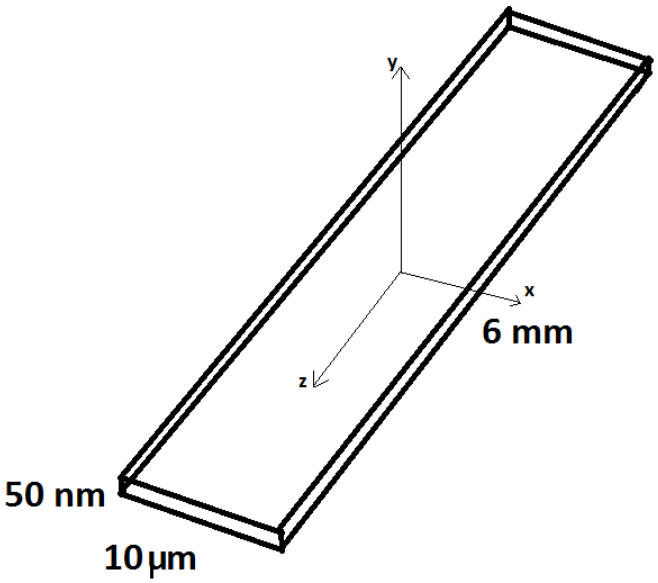

Figure 2.9: RMS Beam Widths

Inserting the density functions, the luminosity function written explicitly is

$$L_0 = \frac{2cN_1N_2f}{(2\pi)^3\sigma_{\bar{x}_1}\sigma_{\bar{y}_1}\sigma_{\bar{z}_1}\sigma_{\bar{x}_2}\sigma_{\bar{y}_2}\sigma_{\bar{z}_2}}\int e^{-\frac{1}{2}\left[\left(\frac{\bar{x}_1}{\sigma_{\bar{x}_1}}\right)^2+\left(\frac{\bar{y}_1}{\sigma_{\bar{y}_1}}\right)^2+\left(\frac{\bar{z}_1}{\sigma_{\bar{z}_1}}\right)^2+\left(\frac{\bar{x}_2}{\sigma_{\bar{x}_2}}\right)^2+\left(\frac{\bar{y}_2}{\sigma_{\bar{y}_2}}\right)^2+\left(\frac{\bar{z}_2}{\sigma_{\bar{z}_2}}\right)^2\right]}dxdydzdt \qquad (2.3)$$

In general, x_1, y_1, z_1 and x_2, y_2, z_2 are dimensions of frames that are rotated and/or boosted from one another. If the beams are crossing at an angle, have a tilt rotation, or are dipping, then you can substitute the rotated frame in for the variable, for instance x_1 would have the form ax+by+cz where a, b, and c are products of cosines and sines of the three rotation angles. In addition, if there are offsets there would be a constant term added for every dimension that there is an offset. Furthermore, if one frame is boosted from another frame we will have Lorentz transformation terms as well. If the beams are collinear then $\bar{x}_1 = \bar{x}_2 = \bar{x}$ and $\bar{y}_1 = \bar{y}_2 = \bar{y}$ which simplifies the integral. Therefore, in the collinear case we obtain

$$L_0 = \frac{2cN_1N_2f}{(2\pi)^3\sigma_{\bar{x}_1}\sigma_{\bar{y}_1}\sigma_{\bar{z}_1}\sigma_{\bar{x}_2}\sigma_{\bar{y}_2}\sigma_{\bar{z}_2}} \int e^{-\frac{1}{2}\left[\bar{x}^2\left(\frac{1}{\sigma_{\bar{x}_1}^2}+\frac{1}{\sigma_{\bar{x}_2}^2}\right)^2+\bar{y}^2\left(\frac{1}{\sigma_{\bar{y}_1}^2}+\frac{1}{\sigma_{\bar{y}_2}^2}\right)^2+\left(\frac{\bar{z}_1}{\sigma_{\bar{z}_1}}\right)^2+\left(\frac{\bar{z}_2}{\sigma_{\bar{z}_2}}\right)^2\right]} dxdydzdt \quad (2.4)$$

In the lab frame, the longitudinal dimensions become $\bar{z}_1 = \gamma_1(z - \beta_1 ct)$ and $\bar{z}_1 = \gamma_2(z + \beta_2 ct)$. The Lorentz factors will cancel out of the exponential from the length contraction of the z rms widths. When having equal sized beams in all dimensions that are collinear (with no rotations or offsets) you come to the well known luminosity equation

$$L_0 = \frac{N_1N_2f}{4\pi\sigma_x\sigma_y} \quad (2.5)$$

As you can see, to boost the luminosity for equal, collinear beams we can either increase the number of charges in each of the beams, increase the frequency, or decrease the x or y rms beam widths. However, the frequency cannot be changed since that is determined by the number of bunches which is determined by the RF bucket. N_1 and N_2 cannot be changed due to the beam-beam limit.

The beams we will be working with cross each other at a shallow angle of about 5 degrees or 83 milliradians. This therefore leads to a new formula that can be solved analytically

including offsets in all 3 spatial dimensions for each beam and three Euler rotations for each beam. If we just have a crossing angle θ, the angle made between the two beams, then we obtain

$$L_0 = \frac{N_1 N_2}{2\pi} \sqrt{\frac{1}{\left(\sigma_{y1}^2 + \sigma_{y2}^2\right)\left[\left(\sigma_{x1}^2 + \sigma_{x2}^2\right) + \left(\sigma_{z1}^2 + \sigma_{z2}^2\right)\tan^2\left(\frac{\theta}{2}\right)\right]}} \tag{2.6}$$

for the luminosity. If we also have x and y offsets for each beam then Equation 2.6 is multiplied by

$$e^{-\frac{\cos^2\left(\frac{\theta}{2}\right)\left[\left(\sigma_{y1}^2+\sigma_{y2}^2\right)\left(x_{1_{off}}-x_{2_{off}}\right)^2+\left(\sigma_{x1}^2+\sigma_{x2}^2\right)\left(y_{1_{off}}-y_{2_{off}}\right)^2\right]+\sin^2\left(\frac{\theta}{2}\right)\left[\left(\sigma_{z1}^2+\sigma_{z2}^2\right)\left(y_{1_{off}}-y_{2_{off}}\right)^2\right]}{\left(\sigma_{y1}^2+\sigma_{y2}^2\right)\left[\cos^2\left(\frac{\theta}{2}\right)\left(\sigma_{x1}^2+\sigma_{x2}^2\right)+\sin^2\left(\frac{\theta}{2}\right)\left(\sigma_{z1}^2+\sigma_{z2}^2\right)\right]}} \tag{2.7}$$

where $x_{1_{off}}$ is the distance the first beam is offset from its nominal orbit in the x-direction, $x_{2_{off}}$ is the distance the second beam is offset from its nominal orbit in the x-direction, $y_{1_{off}}$ is the distance the first beam is offset from its nominal orbit in the y-direction, and $y_{2_{off}}$ is the distance the second beam is offset from its nominal orbit in the y-direction.

The full analytical solution with all three rotations and offsets for all three dimensions is several pages long, thus it is far too large for this document. In the case of zero offsets, the complex formula becomes much simpler, yet still is very long.

As shown though in Figure 2.8, the beams at SuperKEKB will have more of an hourglass shape. This effect is caused by the high β^* at the interaction point and is shown in Figure 2.10.

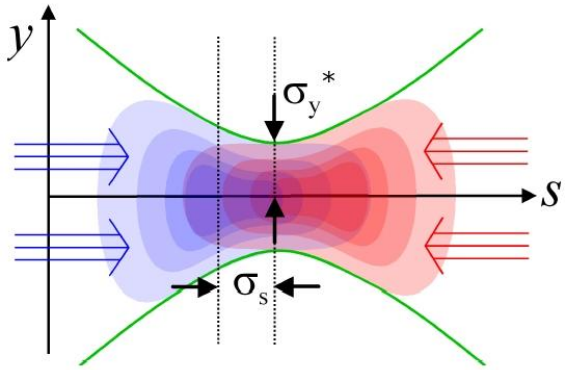

Figure 2.10: Hourglass Effect

This new geometry changes the rms beam widths by the amount

$$\sigma_u(s) = \sigma_u^* \sqrt{1 + \left(\frac{s}{\beta_u^*}\right)^2} \tag{2.8}$$

Obviously this has an effect on the luminosity. The modified luminosity is multiplied by S, the luminosity suppression factor

$$S = \frac{2}{\sqrt{\pi}\sigma_s} \int_0^\infty \frac{e^{-\left(\frac{s}{\sigma_s}\right)^2} e^{-\left(\frac{\theta_s}{\sigma_x(s)}\right)^2}}{\sqrt{1 + \left(\frac{s}{\beta_x^*}\right)^2} \sqrt{1 + \left(\frac{s}{\beta_y^*}\right)^2}} ds \tag{2.9}$$

2.3 Beam Diagnostics

Since the beams are stored for a long time in a storage ring they go around the ring millions of times a second with imperfect magnets and many other perturbing variables, such as micro-ground motion, therefore the beams at the interaction point are not always in the most ideal spot as we would like. They can be offset up, down, left, or right, bloated, or even rotated

in the transverse plane. This can lead to a significant drop in luminosity therefore reducing the effectiveness of the machine.

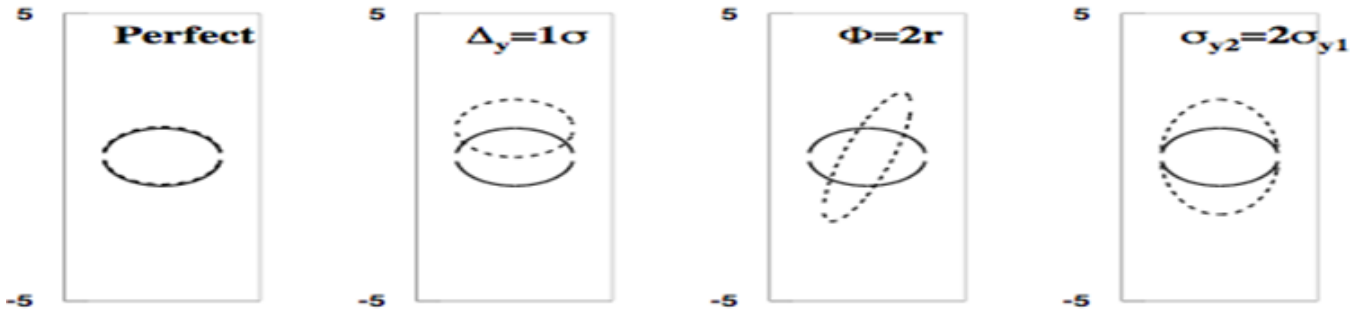

Figure 2.11: Beam Interaction Pictures for the Collinear Case in the x-y Representation

In Figure 2.11, the first diagram shows a perfect head on collision with one beam coming out of the page and the other coming into the page. The dashed ellipse represents the misaligned beam and the solid ellipse represents the correctly aligned beam. This would produce the highest luminosity out of the four diagrams. The second has one of the beams offset in the y direction causing bending in the y since one beam is higher than the other and there will be a vertical force. The third picture has a tilt which diminishes the beam-beam overlap. The fourth diagram shows one of the beams bloated therefore one of the beams will be more spread out with a wider cross sectional area decreasing the interaction density and thus lowering the luminosity.

A device that could detect these non-ideal conditions would be a great calibration technique that would let us measure the results and compare them to what we should theoretically get and then make corrections. For the three "pathologies" presented in Fig. 2.11 a dipole, sextupole, and quadrupole correction are needed, and sufficient to restore optimal collisions.

2.4 Beamstrahlung

The primary way we can do this is by measuring the beamstrahlung from the beams. Beamstrahlung is the radiation given off from one of the beams due to the interaction of the other beam when it bends it due to the Coulomb force. Using the formulae from current theory that we have we can anticipate how much power we should see and then compare that to our measurements making this beamstrahlung a great diagnostic tool.

To do this requires a multiphase project that I will undertake for my doctoral dissertation. First, I will write the simulation software that will calculate the theoretical power for in total and for each polarization in the solid angle that we are actually looking at. Then we will design, build, test, and install an optics box that that will use the beamstrahlung and analyze the spectrum and amount of light that we can compare to my simulations.

Our lab is currently working through several institutions. We are at Wayne State University and have a connection with Pacific National Labs to use their vast computer systems. The optics box for our beam-beam diagnostics will be installed and operation SuperKEKB.

Beryllium mirrors will be used to direct our beamstrahlung from the beam pipe and into our own piping path. The spectral range and solid angle are summarized in Table 2.2.

	LER	HER
Polar Angle (mrad)	$9.9 \leq \theta \leq 10.4$	$7.8 \leq \theta \leq 8.2$
Azimuthal Angle (rad)	$\frac{\pm\pi}{2} - 0.0040 \leq \varphi \leq \frac{\pm\pi}{2} + 0.0040$	$\frac{\pm\pi}{2} - 0.0040 \leq \varphi \leq \frac{\pm\pi}{2} + 0.0040$
Spectral Bandwidth (nm)	$350 \leq \lambda \leq 650$	$350 \leq \lambda \leq 650$

Table 2.2: Beamstrahlung Detector Parameters

Since no machine is perfectly symmetrical there are asymmetries that develop over many revolutions around the beam pipe for each beam. There are eight types of asymmetries that we can calculate and measure. First, there can develop an x or y-offset where one beam is displaced some distance in either the x or y direction from the other beam or both. Second, transverse bloating of the beam can occur. Each beam has two transverse dimensions therefore both beams combined have four different parameters that can bloat$\left(\sigma_{x_1}, \sigma_{y_1}, \sigma_{x_2}, \sigma_{y_2}\right)$. This can be reduced to just x-bloating or y-bloating since we only care about how much interaction the two beams have. Lastly, one of the beams can be rotated along its beam axis causing a tilt angle. Both beams could have their own tilt angle. Once again, if each beam has its own tilt angle, with respect to a beam of our choosing there is only one tilt angle between them.

These asymmetries cause non-optimal overlap of the two beams thus reducing the luminosity. Therefore, a more accurate description of luminosity is one where it evolves over time as [19]

$$L(t) = L_0(t)\big(1 - w(t)\big) \tag{2.10}$$

where $w(t)$ is a positive-defined waste parameter due to sub-optimal crossing. If $w(t)$ is a known quantity then the integrated luminosity that is wasted is

$$L_w = f \int L_0(t) w(t) dt \tag{2.11}$$

where f is the machine frequency. Solving for the waste parameter and dropping the time dependence one obtains

$$w = 1 - \frac{L}{L_0}. \tag{2.12}$$

We measure beamstrahlung because it is related to the waste parameter w. Briefly, the radiation emitted in the beam-beam collision is observed at angles much larger than the deflection angle. For this situation, the "short magnet approximation" is the best at predicting the spectrum, leading to a radiation formula [20],

$$\frac{d^2\boldsymbol{U}}{d\Omega d\omega} = \frac{r_0\gamma^2 f_i(\varphi,\theta)}{\pi c m_e c^2}\left|\tilde{\boldsymbol{F}}\left(\frac{\omega(1+\gamma^2\theta^2)}{2c\gamma^2}\right)\right|^2 \quad where\ \Omega = sin\theta d\theta d\varphi \approx \theta d\theta d\varphi \tag{2.13}$$

where $\boldsymbol{U}$ is the two-dimensional vector (U_x, U_y), r_0 is the classical radius, $f_i(\varphi,\theta)$ is an angular function depending if we want the σ or π directions (which are the polarizations parallel and perpendicular to the bending force, respectively), m_e is the mass of an electron (and positron), ω is the angular frequency of the radiation, θ is the polar angle of the emitted radiation, and Ω is the solid angle of the emitted radiation.

The angular functions $f_i(\varphi,\theta)$ are our main interest. They are

$$f_\sigma(\varphi,\theta) = \frac{[1-\gamma^2\theta^2\cos(2\varphi)]^2}{[1+\gamma^2\theta^2]^4} \quad and \quad f_\pi(\varphi,\theta) = \frac{[\gamma^2\theta^2\sin(2\varphi)]^2}{[1+\gamma^2\theta^2]^4} \tag{2.14}$$

which in the limit of $\theta \gg \frac{1}{\gamma}$ become

$$f_\sigma(\varphi,\theta) = \frac{\cos^2(2\varphi)}{[\gamma^2\theta^2]^2} \quad and \quad f_\pi(\varphi,\theta) = \frac{\sin^2(2\varphi)}{[\gamma^2\theta^2]^2}. \tag{2.15}$$

It is clear that detecting radiation at specific angles will detect force components integrated over charge distributions. Therefore the large angle beamstrahlung monitor, LABM, consists of narrow telescopes at large angles and at specific azimuthal points as in Table 2.2.

Asymmetries are defined as dimensionless quantities, created out of beamstrahlung observables, which are sensitive to w. In the definitions below, $U_{(x,y)(1,2)}$ refer to the detected radiation emitted by beam 1 or 2, due to the bending force along x or y (the indices 1 and 2 are dropped whenever they are not necessary). Different asymmetries are sensitive to different beam pathologies. For y-offset, we use

$$A_1 = \left(\frac{U_y}{U_x} - 1\right)\Theta\left(\frac{U_y}{U_x} - 1\right) \tag{2.16}$$

where Θ is the Heaviside function.

Likewise, when there is y-bloating between the two beams we define the asymmetry as

$$A_2 = \left(\frac{U_{2y}}{U_{1y}} - 1\right)\Theta\left(\frac{U_{2y}}{U_{1y}} - 1\right) \tag{2.17}$$

where U_{1y} is the energy radiated from beam 1 due to bending in the x-dimension and U_{2y} is the energy radiated from beam 2 due to bending in the y-direction.

Lastly, in the case of a tilt angle between the two beams we define the asymmetry as

$$A_3 = |\sin(\boldsymbol{U}_1, \boldsymbol{U}_2)| \tag{2.18}$$

where $\boldsymbol{U}_1$ is the two-dimensional vector constructed with the energy radiated from beam 1 and $\boldsymbol{U}_2$ is the corresponding vector from beam 2 and $\boldsymbol{U}_1, \boldsymbol{U}_2$ is the angle between the two vectors.

Figure 2.12 shows how these asymmetries relate to luminosity loss where the solid arrow is associated with beam 1 and the dashed arrow is associated with beam 2. Notice that the radiated energies have been normalized (for example, energy and beam population effects are divided out) so that we can only see the difference due to the bad beam pathologies. The relation between asymmetries and w is discussed in Chapter 3. This now needs to be done for the non-

collinear case when we have a crossing angle as well as having two or more of these pathologies at once.

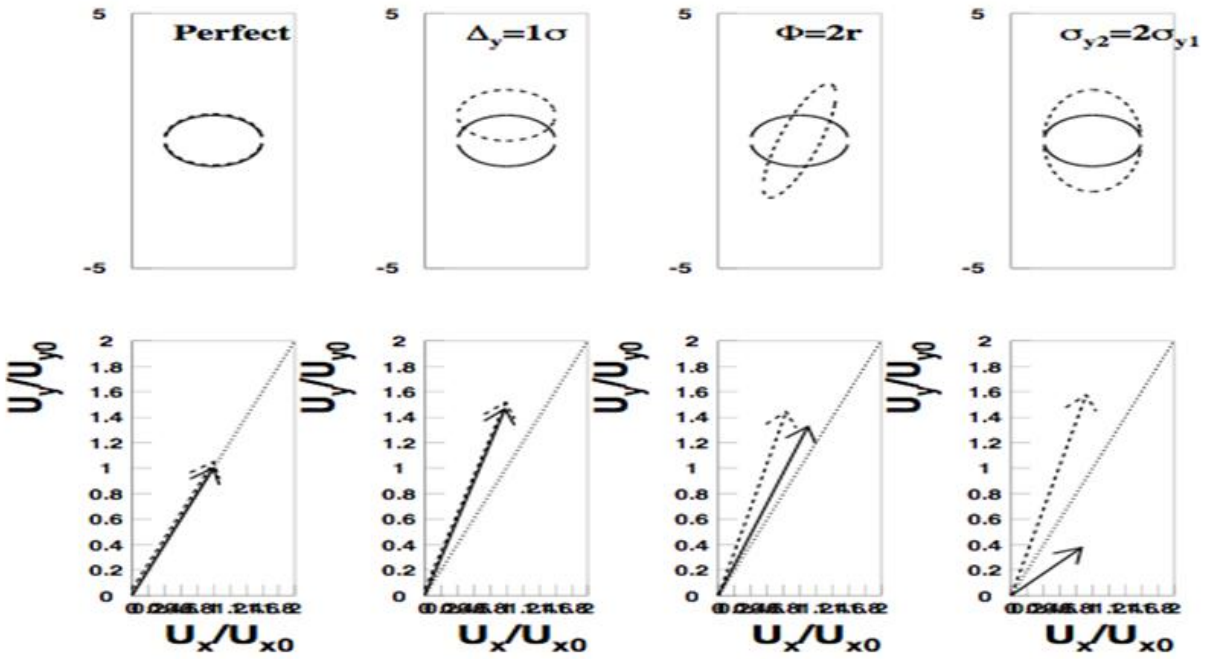

Figure 2.12: Normalized Transverse Power Beamstrahlung Diagrams

Chapter 3 : Beamstrahlung Simulation and Modeling

3.1 Total Power

3.1.1 Only Using Crossing Angle

When charged particles accelerate by an increase in speed and/or a change in direction they emit radiation. In a basic synchrotron, charged particles travel around a circular beam pipe therefore they are changing direction most of the time. This radiation that is emitted is called synchrotron radiation. The large magnets around the beam pipe are what keep the beam on course therefore they are the cause of this synchrotron radiation. This amount of this radiation can be determined by the Larmor formula [12] in SI units as

$$P = \frac{q^2 \dot{v}^2}{6\pi\varepsilon_0 c^3} \tag{3.1}$$

where q is the electric charge of the charged particle, $\dot{v}$ acceleration of the particle, ε_0 is the permittivity of free space, and c is the speed of light.

The relativistic generalization [12] in CGS units is

$$P = \frac{2q^2\gamma^6}{3c}\left[\left(\dot{\beta}\right)^2 - \left(\beta \times \dot{\beta}\right)^2\right] \tag{3.2}$$

where γ is the Lorentz factor (explained later), $\beta = \frac{v}{c}$, and $\dot{\beta} = \frac{\dot{v}}{c}$.

However, charged particles not only have an electric field when they are moving, but also have a magnetic field. Therefore, each beam is in itself a magnet. When two beams come close to each other they can cause each other to bend, therefore emitting radiation. This beam-beam radiation is called beamstrahlung.

Since we are in a circular accelerator where the momentum $\boldsymbol{p}$ changes rapidly in direction as the particle travels around the beam pipe, but there is only a small change in energy per revolution then we can approximate the radiated power from Equation 3.2 in CGS units [12] as

$$P = \frac{2}{3}\frac{e^2}{m^2c^3}\gamma^2\omega^2|\boldsymbol{p}|^2 = \frac{2}{3}\frac{e^2c}{\rho^2}\beta^4\gamma^4 \tag{3.3}$$

where $\omega = \frac{\beta c}{\rho}$ with ρ being the orbit radius.

We know that the orbit radius that a particle travels along will be related to

$$\rho = \frac{\gamma m\beta^2c^2}{F} \tag{3.4}$$

therefore solving for $\frac{1}{\rho^2}$ we obtain

$$\frac{1}{\rho^2} = \frac{F^2}{\gamma^2m^2\beta^4c^4}. \tag{3.5}$$

Substituting this into Equation 3.3 and converting to SI units we obtain the radiated power for a charged particle to be

$$P = \frac{2}{3} e^2 c \beta^4 \gamma^4 \frac{F^2}{\gamma^2 m^2 \beta^4 c^4} \rightarrow P = \frac{e^2 \gamma^2}{6\pi\varepsilon_0 m^2 c^3} F^2. \tag{3.6}$$

Therefore, the power radiated from beam 1 due to the x-direction bending is

$$W_{x1} = \frac{Q^2 \gamma_1^2}{6\pi\varepsilon_0 m^2 c^3} \int dx_{D_1} dy_{D_1} dz_{D_1} dt_{D_1} \rho_1\left(x_{D_1}, y_{D_1}, z_{D_1}, t_{D_1}\right) F_{2x}^2\left(x_{D_1}, y_{D_1}, z_{D_1}, t_{D_1}\right) \tag{3.7}$$

and the power radiated from beam 1 due to the y-direction bending is

$$W_{y1} = \frac{Q^2 \gamma_1^2}{6\pi\varepsilon_0 m^2 c^3} \int dx_{D_1} dy_{D_1} dz_{D_1} dt_{D_1} \rho_1\left(x_{D_1}, y_{D_1}, z_{D_1}, t_{D_1}\right) F_{2y}^2\left(x_{D_1}, y_{D_1}, z_{D_1}, t_{D_1}\right) \tag{3.8}$$

However, we started with the beam density, force, and the coordinates of both in different frames, therefore the power radiated from beam 1 due to the x-direction bending is

$$W_{x1} = \frac{Q^2 \gamma_1^2}{6\pi\varepsilon_0 m^2 c^3} \int dx_{D_1} dy_{D_1} dz_{D_1} dt_{D_1} \rho_{1\,Frame\ B1}(\bar{x}_1, \bar{y}_1, \bar{z}_1, \bar{t}_1) F_{2x_{Frame\ B2}}^2(\bar{x}_2, \bar{y}_2, \bar{z}_2, \bar{t}_2) \tag{3.9}$$

and the power radiated from beam 1 due to the y-direction bending is

$$W_{y1} = \frac{Q^2 \gamma_1^2}{6\pi\varepsilon_0 m^2 c^3} \int dx_{D_1} dy_{D_1} dz_{D_1} dt_{D_1} \rho_{1\,Frame\ B1}(\bar{x}_1, \bar{y}_1, \bar{z}_1, \bar{t}_1) F_{2y_{Frame\ B2}}^2(\bar{x}_2, \bar{y}_2, \bar{z}_2, \bar{t}_2) \tag{3.10}$$

Therefore we need to rotate and/or boost everything into the detector frame of the radiating beam.

To find the amount of power radiated, it is first necessary to start with the electric potential. The three dimensional electric potential in a beam's rest frame [19] is

$$\Phi(\bar{x}, \bar{y}, \bar{z}) = \frac{Q}{4\pi^{\frac{3}{2}}\varepsilon_0} \int_0^\infty \frac{e^{-\frac{\bar{x}^2}{2\sigma_{\bar{x}}^2+q} - \frac{\bar{y}^2}{2\sigma_{\bar{y}}^2+q} - \frac{\bar{z}^2}{2\sigma_{\bar{z}}^2+q}}}{\sqrt{2\sigma_{\bar{x}}^2 + q}\sqrt{2\sigma_{\bar{y}}^2 + q}\sqrt{2\sigma_{\bar{z}}^2 + q}} dq \tag{3.11}$$

where Q is the total charge of the beam, $\bar{x}$, $\bar{y}$, and $\bar{z}$ are the rest frame coordinates, and $\sigma_{\bar{x}}$, $\sigma_{\bar{y}}$, and $\sigma_{\bar{z}}$ are the rms beam widths in the rest frame of the beam.

From basic electrodynamics, the negative gradient of the electric potential gives the electric field vector

$$\boldsymbol{E} = -\boldsymbol{\nabla}\Phi. \tag{3.12}$$

The x-component of the electric field in the rest frame is

$$\overline{\mathrm{E_x}} = \frac{\partial}{\partial \bar{x}}\left[\frac{Q}{4\pi^{\frac{3}{2}}\varepsilon_0}\int_0^\infty \frac{e^{-\frac{\bar{x}^2}{2\sigma_{\bar{x}}^2+q}-\frac{\bar{y}^2}{2\sigma_{\bar{y}}^2+q}-\frac{\bar{z}^2}{2\sigma_{\bar{z}}^2+q}}}{\sqrt{2\sigma_{\bar{x}}^2+q}\sqrt{2\sigma_{\bar{y}}^2+q}\sqrt{2\sigma_{\bar{y}}^2+q}}dq\right] = \frac{Q}{2\pi^{\frac{3}{2}}\varepsilon_0}\int_0^\infty \frac{\bar{x}e^{-\frac{\bar{x}^2}{2\sigma_{\bar{x}}^2+q}-\frac{\bar{y}^2}{2\sigma_{\bar{y}}^2+q}-\frac{\bar{z}^2}{2\sigma_{\bar{y}}^2+q}}}{(2\sigma_{\bar{x}}^2+q)^{\frac{3}{2}}\sqrt{2\sigma_{\bar{y}}^2+q}\sqrt{2\sigma_{\bar{y}}^2+q}}dq \tag{3.13}$$

the y-component of the electric field in the rest frame is

$$\overline{\mathrm{E_y}} = \frac{\partial}{\partial \bar{y}}\left[\frac{Q}{4\pi^{\frac{3}{2}}\varepsilon_0}\int_0^\infty \frac{e^{-\frac{\bar{x}^2}{2\sigma_{\bar{x}}^2+q}-\frac{\bar{y}^2}{2\sigma_{\bar{y}}^2+q}-\frac{\bar{z}^2}{2\sigma_{\bar{z}}^2+q}}}{\sqrt{2\sigma_{\bar{x}}^2+q}\sqrt{2\sigma_{\bar{y}}^2+q}\sqrt{2\sigma_{\bar{y}}^2+q}}dq\right] = \frac{Q}{4\pi^{\frac{3}{2}}\varepsilon_0}\int_0^\infty \frac{\bar{y}e^{-\frac{\bar{x}^2}{2\sigma_{\bar{x}}^2+q}-\frac{\bar{y}^2}{2\sigma_{\bar{y}}^2+q}-\frac{\bar{z}^2}{2\sigma_{\bar{z}}^2+q}}}{\sqrt{2\sigma_{\bar{x}}^2+q}(2\sigma_{\bar{y}}^2+q)^{\frac{3}{2}}\sqrt{2\sigma_{\bar{y}}^2+q}}dq \tag{3.14}$$

and the z-component of the electric field in the rest frame is

$$\overline{\mathrm{E_z}} = \frac{\partial}{\partial \bar{z}}\left[\frac{Q}{4\pi^{\frac{3}{2}}\varepsilon_0}\int_0^\infty \frac{e^{-\frac{\bar{x}^2}{2\sigma_{\bar{x}}^2+q}-\frac{\bar{y}^2}{2\sigma_{\bar{y}}^2+q}-\frac{\bar{z}^2}{2\sigma_{\bar{z}}^2+q}}}{\sqrt{2\sigma_{\bar{x}}^2+q}\sqrt{2\sigma_{\bar{y}}^2+q}\sqrt{2\sigma_{\bar{y}}^2+q}}dq\right] = \frac{Q}{4\pi^{\frac{3}{2}}\varepsilon_0}\int_0^\infty \frac{\bar{z}e^{-\frac{\bar{x}^2}{2\sigma_{\bar{x}}^2+q}-\frac{\bar{y}^2}{2\sigma_{\bar{y}}^2+q}-\frac{\bar{z}^2}{2\sigma_{\bar{z}}^2+q}}}{\sqrt{2\sigma_{\bar{x}}^2+q}\sqrt{2\sigma_{\bar{y}}^2+q}(2\sigma_{\bar{z}}^2+q)^{\frac{3}{2}}}dq. \tag{3.15}$$

However, we are not working in the rest frame of the beam. The frames of interest are that of each optics box detector. These are fixed to each beam pipe therefore we need to use special relativity to boost to the correct inertial frame. The Lorentz factor is

$$\gamma = \frac{1}{\sqrt{1-\beta^2}} \;\; where\; \beta^2 = \beta_x^2+\beta_y^2+\beta_z^2 = \left(\frac{v_x}{c}\right)^2+\left(\frac{v_y}{c}\right)^2+\left(\frac{v_z}{c}\right)^2. \tag{3.16}$$

In general, the Lorentz transformation matrix for the space-time coordinates from a fixed frame S (represented by the vector on the right) to a frame S' moving in an arbitrary direction (represented by the vector on the left) is [12]

$$\begin{bmatrix} ct' \\ x' \\ y' \\ z' \end{bmatrix} = \begin{bmatrix} \gamma & -\gamma\beta_x & -\gamma\beta_y & -\gamma\beta_z \\ -\gamma\beta_x & 1+(\gamma-1)\frac{\beta_x^2}{\beta^2} & (\gamma-1)\frac{\beta_x\beta_y}{\beta^2} & (\gamma-1)\frac{\beta_x\beta_z}{\beta^2} \\ -\gamma\beta_y & (\gamma-1)\frac{\beta_y\beta_x}{\beta^2} & 1+(\gamma-1)\frac{\beta_y^2}{\beta^2} & (\gamma-1)\frac{\beta_y\beta_z}{\beta^2} \\ -\gamma\beta_z & (\gamma-1)\frac{\beta_z\beta_x}{\beta^2} & (\gamma-1)\frac{\beta_z\beta_y}{\beta^2} & 1+(\gamma-1)\frac{\beta_z^2}{\beta^2} \end{bmatrix} \begin{bmatrix} ct \\ x \\ y \\ z \end{bmatrix} \tag{3.17}$$

The electric fields are not 4-vectors and transform from the S frame to the S' frame as

$$\begin{bmatrix} E_x' \\ E_y' \\ E_z' \end{bmatrix} = \gamma \begin{bmatrix} \overline{E_x} \\ \overline{E_y} \\ \frac{1}{\gamma}\overline{E_z} \end{bmatrix} \tag{3.18}$$

assuming the direction of motion is in the z-direction for example. As you will notice the fields perpendicular to the direction of motion are multiplied by the Lorentz factor whereas the field perpendicular to the direction of motion is not. This causes a pancake-like form of the fields.

As already mentioned in the rest frame of the beam, there is only an electric field. Once the beam is boosted to the rest frame of the beam pipe that the beam is travelling in then the beam also acquires a magnetic field from the transformation of

$$\boldsymbol{B}'_{from\,1} = \frac{1}{c^2}\left(\boldsymbol{v}_1 \times \boldsymbol{E}'_{from\,1}\right) \tag{3.19}$$

where $\boldsymbol{v_1}$ is the velocity vector of the particles in the beam and $\boldsymbol{E_1'}$ is the electric field in the S' frame. Note we are now in the prime frame which is the frame of the beam pipe of the beam. I chose to show the equation for the first beam, therefore the subscripts are 1.

As the beams travel around the beam pipe and get close to each other, besides a very small gravitational force, they will feel an electric and magnetic force. These two forces are combined into the Lorentz Force

$$\boldsymbol{F}'_{from\ 1\ on\ 2} = Q\left(\boldsymbol{E}'_{from\ 1} + \boldsymbol{v_2} \times \boldsymbol{B}'_{from\ 1}\right) \tag{3.20}$$

where $\boldsymbol{v_2}$ is the velocity vector of the other beam.

When Equation 3.19 is substituted into the Lorentz Force equation we obtain

$$\begin{aligned} \boldsymbol{F}'_{from\ 1\ on\ 2} &= Q\left(\boldsymbol{E}'_{from\ 1} + \boldsymbol{v_2} \times \left(\frac{1}{c^2}\left(\boldsymbol{v_1} \times \boldsymbol{E}'_{from\ 1}\right)\right)\right) \\ &= Q\left(\boldsymbol{E}'_{from\ 1} + \frac{1}{c^2}\left[\boldsymbol{v_1}\left(\boldsymbol{v_2} \cdot \boldsymbol{E}'_{from\ 1}\right) - \boldsymbol{E}'_{from\ 1}(\boldsymbol{v_1} \cdot \boldsymbol{v_2})\right]\right). \end{aligned} \tag{3.21}$$

This further simplifies using the triple cross product rule known as BAC-CAB.

Performing the dot products and breaking the force into x, y, and z components we obtain we obtain the force in the x-direction

$$\begin{aligned} F'_{from\ 1\ on\ 2_x} &= Q\left[E'_{1x} + \beta_{1x}\left(\beta_{2x}E'_{1x} + \beta_{2y}E'_{1y} + \beta_{2z}E'_{1z}\right) - E'_{1x}\left(\beta_{1x}\beta_{2x} + \beta_{1y}\beta_{2y} + \beta_{1z}\beta_{2z}\right)\right] \\ &= Q\left[\left(1 - \beta_{1y}\beta_{2y} - \beta_{1z}\beta_{2z}\right)E'_{1x} + \beta_{1x}\beta_{2y}E'_{1y} + \beta_{1x}\beta_{2z}E'_{1z}\right] \end{aligned} \tag{3.22}$$

the force in the y-direction

$$\begin{aligned} F'_{from\ 1\ on\ 2_y} &= Q\left[E'_{1y} + \beta_{1y}\left(\beta_{2x}E'_{1x} + \beta_{2y}E'_{1y} + \beta_{2z}E'_{1z}\right) - E'_{1y}\left(\beta_{1x}\beta_{2x} + \beta_{1y}\beta_{2y} + \beta_{1z}\beta_{2z}\right)\right] \\ &= Q\left[\beta_{1y}\beta_{2x}E'_{1x} + (1 - \beta_{1x}\beta_{2x} - \beta_{1z}\beta_{2z})E'_{1y} + \beta_{1y}\beta_{2z}E'_{1z}\right] \end{aligned} \tag{3.23}$$

and the force in the z-direction

$$F'_{from\ 1\ on\ 2_z} = Q\left[E'_{1z} + \beta_{1z}\left(\beta_{2x}E'_{1x} + \beta_{2y}E'_{1y} + \beta_{2z}E'_{1z}\right) - E'_{1z}\left(\beta_{1x}\beta_{2x} + \beta_{1y}\beta_{2y} + \beta_{1z}\beta_{2z}\right)\right]$$
$$= Q\left[\beta_{1z}\beta_{2x}E'_{1x} + \beta_{1z}\beta_{2y}E'_{1y} + \left(1 - \beta_{1x}\beta_{2x} - \beta_{1y}\beta_{2y}\right)E'_{1z}\right]. \quad (3.24)$$

We're in the first beam's beam pipe's frame therefore it would appear that beam 1 is moving with velocity $\beta_1 c$ down the beam pipe's z-axis. Beam 2 is moving down its beam pipe's z-axis but in the opposite direction, thus with velocity $-\beta_2 c$. Beam 2 is rotated an angle θ from beam 1, therefore rotating about the beam's y-axis we obtain the $\beta_2$vector. The β vectors for both beams in the first beam's beam pipe frame are

$$\boldsymbol{\beta_1}_{Frame\ B'_1} = \begin{bmatrix} 0 \\ 0 \\ \beta_1 \end{bmatrix} \quad and \quad \boldsymbol{\beta_2}_{Frame\ B'_1} = \begin{bmatrix} \beta_2 sin(\theta) \\ 0 \\ -\beta_2 cos(\theta) \end{bmatrix}. \quad (3.25)$$

Substituting these β components from the β vectors into Equations 3.22-3.24 the x-component of the Lorentz force becomes

$$F'_{from\ 1\ on\ 2_{x_{Frame\ B'_1}}} = Q\left[\left(1 + \beta_1\beta_2 cos(\theta)\right)E'_{1x}\right] \quad (3.26)$$

the y-component of the Lorentz force becomes

$$F'_{from\ 1\ on\ 2_{y_{Frame\ B'_1}}} = Q\left[\left(1 + \beta_1\beta_2 cos(\theta)\right)E'_{1y}\right] \quad (3.27)$$

and the z-component of the Lorentz force becomes

$$F'_{from\ 1\ on\ 2_{z_{Frame\ B'_1}}} = Q[\beta_1\beta_2 sin(\theta)E'_{1x} + E'_{1z}]. \quad (3.28)$$

Notice that in Equations 3.26 and 3.27 the x and y-components of the force only depend on their respective electric field components. However, in Equation 3.28 the z-component of the force depends on its electric field component, but also the x-component of the electric field.

These forces are still in the beam pipe's frame, so they still need to be rotated to the detector's frame in the other beam pipe using the rotation matrix

$$\begin{bmatrix} F'_{from\ 1\ on\ 2_{x_{Frame\ D2}}} \\ F'_{from\ 1\ on\ 2_{y_{Frame\ D2}}} \\ F'_{from\ 1\ on\ 2_{z_{Frame\ D2}}} \end{bmatrix} = \begin{bmatrix} \cos(\theta) & 0 & -\sin(\theta) \\ 0 & 1 & 0 \\ \sin(\theta) & 0 & \cos(\theta) \end{bmatrix} \begin{bmatrix} F'_{from\ 1\ on\ 2_{x_{Frame\ B'_1}}} \\ F'_{from\ 1\ on\ 2_{y_{Frame\ B'_1}}} \\ F'_{from\ 1\ on\ 2_{z_{Frame\ B'_1}}} \end{bmatrix} \tag{3.29}$$

which transforms from the first beam's $B_1^{'}$ frame to the detector frame $D2$.

Performing the necessary matrix multiplication, we obtain the Lorentz Force components in the detector frame. The detector frame's Lorentz force x-component due to beam 1 is

$$F'_{from\ 1\ on\ 2_{x_{Frame\ D2}}} = F'_{from\ 1\ on\ 2_{x_{Frame\ B'_1}}} \cos(\theta) - F'_{from\ 1\ on\ 2_{z_{Frame\ B'_1}}} \sin(\theta). \tag{3.30}$$

The detector frame's Lorentz force y-component due to beam 1 is

$$F'_{from\ 1\ on\ 2_{y_{Frame\ D2}}} = F'_{from\ 1\ on\ 2_{y_{Frame\ B'_1}}}. \tag{3.31}$$

The detector frame's Lorentz force z-component due to beam 1 is

$$F'_{from\ 1\ on\ 2_{z_{Frame\ D2}}} = F'_{from\ 1\ on\ 2_{x_{Frame\ B'_1}}} \sin(\theta) + F'_{from\ 1\ on\ 2_{z_{Frame\ B'_1}}} \cos(\theta). \tag{3.32}$$

Now we can substitute in the $B_1^{'}$ force components to get the x-component

$$\begin{aligned} F'_{from\ 1\ on\ 2_{x_{Frame\ D2}}} &= Q\left[\left(1 + \beta_1\beta_2 cos(\theta)\right)E'_{1x}\right]\cos(\theta) - Q[\beta_1\beta_2 sin(\theta)E'_{1x} + E'_{1z}]\sin(\theta) \\ &= Q\left[\left(\cos(\theta) + \beta_1\beta_2(\cos^2(\theta) - \sin^2(\theta))\right)E'_{1x} - \sin(\theta)\,E'_{1z}\right] \end{aligned} \tag{3.33}$$

the y-component

$$F'_{from\ 1\ on\ 2_{y_{Frame\ D2}}} = Q\left[\left(1 + \beta_1\beta_2 cos(\theta)\right)E'_{1y}\right] \tag{3.34}$$

and the z-component

$$F'_{from\ 1\ on\ 2_{z_{Frame\ D2}}} = Q\left[\left(1+\beta_1\beta_2 cos(\theta)\right)E'_{1x}\right]\sin(\theta) + Q[\beta_1\beta_2 sin(\theta)E'_{1x} + E'_{1z}]\cos(\theta)$$
$$= Q\left[\left(\sin(\theta) + 2\beta_1\beta_2\sin(\theta)\,cos(\theta)\right)E'_{1x} + \cos(\theta)E'_{1z}\right] \tag{3.35}$$

Using Equation 3.18, we can get the Lorentz Force components in terms of the rest frame electric field components. The x-component is

$$F'_{from\ 1\ on\ 2_{x_{Frame\ D2}}} = \ Q\left[\gamma_1\left(\cos(\theta) + \beta_1\beta_2(\cos^2(\theta) - \sin^2(\theta))\right)\overline{E_{1x}} - \sin(\theta)\,\overline{E_{1z}}\right] \tag{3.36}$$

The y-component is

$$F'_{from\ 1\ on\ 2_{y_{Frame\ D2}}} = Q\left[\gamma_1\left(1+\beta_1\beta_2 cos(\theta)\right)\overline{E_{1y}}\right] \tag{3.37}$$

The z-component is

$$F'_{from\ 1\ on\ 2_{z_{Frame\ D2}}} = Q\left[\gamma_1\left(\sin(\theta) + 2\beta_1\beta_2\sin(\theta)\,cos(\theta)\right)\overline{E_{1x}} + \cos(\theta)\overline{E_{1z}}\right]. \tag{3.38}$$

Repeating what we did for the first beam's Lorentz Force, we can also find the Lorentz Force due to beam 2 on beam 1. This is equivalent to interchanging the 1 and 2 labels, while keeping track of certain signs in the rotation matrices. The results are

$$F'_{from\ 2\ on\ 1_{x_{Frame\ D_1}}} = Q\left[\gamma_2\left(cos(\theta) + \beta_1\beta_2(\cos^2(\theta) - \sin^2(\theta))\right)\overline{E_{2x}} + \sin(\theta)\,\overline{E_{2z}}\right] \tag{3.39}$$

$$F'_{from\ 2\ on\ 1_{y_{Frame\ D_1}}} = Q\left[\gamma_2\left(1+\beta_1\beta_2 cos(\theta)\right)\overline{E_{2y}}\right] \tag{3.40}$$

$$F'_{from\ 2\ on\ 1_{z_{Frame\ D_1}}} = Q\left[-\gamma_2\left(\sin(\theta) + 2\beta_1\beta_2\sin(\theta)\,cos(\theta)\right)\overline{E_{2x}} + cos(\theta)\overline{E_{2z}}\right] \tag{3.41}$$

Before substituting the rest frame electric field components into the three Lorentz Force components for each beam it will be easier to first define two quantities based from the electric fields in Equations 3.13-3.15. The quantity

$$A_1(q) = \frac{Q}{2\pi^{\frac{3}{2}}\varepsilon_0} \frac{e^{-\frac{\bar{x}_1{}^2}{2\sigma_{\bar{x}_1}^2+q} - \frac{\bar{y}_1{}^2}{2\sigma_{\bar{y}_1}^2+q} - \frac{\bar{z}_1{}^2}{2\sigma_{\bar{z}_1}^2+q}}}{\sqrt{2\sigma_{\bar{x}_1}^2+q}\sqrt{2\sigma_{\bar{y}_1}^2+q}\sqrt{2\sigma_{\bar{z}_1}^2+q}} \tag{3.42}$$

comes from the electric field due to the first beam and the quantity

$$A_2(q) = \frac{Q}{2\pi^{\frac{3}{2}}\varepsilon_0} \frac{e^{-\frac{\bar{x}_2{}^2}{2\sigma_{\bar{x}_2}^2+q} - \frac{\bar{y}_2{}^2}{2\sigma_{\bar{y}_2}^2+q} - \frac{\bar{z}_2{}^2}{2\sigma_{\bar{z}_2}^2+q}}}{\sqrt{2\sigma_{\bar{x}_2}^2+q}\sqrt{2\sigma_{\bar{y}_2}^2+q}\sqrt{2\sigma_{\bar{z}_2}^2+q}} \tag{3.43}$$

comes from the electric field due to the second beam.

Using these two quantities, the Lorentz Force equations can be simplified. The x-component of the force due to the first beam is

$$F'_{from\ 1\ on\ 2_{x_{Frame\ D2}}} = \int_0^\infty dq\ Q\left[\gamma_1\left(\cos(\theta)+\beta_1\beta_2(\cos^2(\theta)-\sin^2(\theta))\right)\frac{\bar{x}_1}{2\sigma_{\bar{x}_1}^2+q} - \sin(\theta)\frac{\bar{z}_1}{2\sigma_{\bar{z}_1}^2+q}\right]A_1(q) \tag{3.44}$$

the y-component of the force due to the first beam is

$$F'_{from\ 1\ on\ 2_{y_{Frame\ D2}}} = \int_0^\infty dq\ Q\left[\gamma_1\left(1+\beta_1\beta_2 cos(\theta)\right)\frac{\bar{y}_1}{2\sigma_{\bar{y}_1}^2+q}\right]A_1(q) \tag{3.45}$$

and the z-component of the force due to the first beam is

$$F'_{from\ 1\ on\ 2_{z_{Frame\ D2}}} = \int_0^\infty dq\ Q\left[\gamma_1\left(\sin(\theta)+2\beta_1\beta_2\sin(\theta)\,cos(\theta)\right)\frac{\bar{x}_1}{2\sigma_{\bar{x}_1}^2+q} + \cos(\theta)\frac{\bar{z}_1}{2\sigma_{\bar{z}_1}^2+q}\right]A_1(q). \tag{3.46}$$

The x-component of the force due to the second beam is

$$F'_{2x_{Frame\,D_1}} = \int_0^\infty dq\, Q\left[\gamma_2\left(cos(\theta) + \beta_1\beta_2(\cos^2(\theta) - \sin^2(\theta))\right)\frac{\bar{x}_2}{2\sigma_{\bar{x}_2}^2 + q} + \sin(\theta)\frac{\bar{z}_2}{2\sigma_{\bar{z}_2}^2 + q}\right]A_2(q) \tag{3.47}$$

the y-component of the force due to the second beam is

$$F'_{2y_{Frame\,D_1}} = \int_0^\infty dq\, Q\left[\gamma_2\left(1 + \beta_1\beta_2 cos(\theta)\right)\frac{\bar{y}_2}{2\sigma_{\bar{y}_2}^2 + q}\right]A_2(q) \tag{3.48}$$

and the z-component of the force due to the second beam is

$$F'_{2z_{Frame\,D_1}} = \int_0^\infty dq\, Q\left[-\gamma_2\left(\sin(\theta) + 2\beta_1\beta_2\sin(\theta)\, cos(\theta)\right)\frac{\bar{x}_2}{2\sigma_{\bar{x}_2}^2 + q} + cos(\theta)\frac{\bar{z}_2}{2\sigma_{\bar{z}_2}^2 + q}\right]A_2(q). \tag{3.49}$$

Now that we have found all of the Lorentz Force components from each beam we can now use those directly to find the power radiated. We are only interested in the transverse power so we'll be focusing on the x and y components of the electric field. Both sets of power equations use the force component from the other beam squared multiplied by the density of the radiating beam. Essentially, we are taking the power radiated per particle and we are integrating it over the entire radiating beam [22].

Our first approximation is applied by neglecting the z-direction forces, since their effect on emitted power is suppressed by factors of γ. The number density of the first beam in its rest frame is

$$\rho_{1_{Frame\,B1}} = \frac{N_1}{(2\pi)^{\frac{3}{2}}\bar{\sigma}_{x_1}\bar{\sigma}_{y_1}\bar{\sigma}_{z_1}}\, e^{-\frac{1}{2}\left[\left(\frac{\bar{x}_1}{\bar{\sigma}_{x_1}}\right)^2 + \left(\frac{\bar{y}_1}{\bar{\sigma}_{y_1}}\right)^2 + \left(\frac{\bar{z}_1}{\bar{\sigma}_{z_1}}\right)^2\right]} \tag{3.50}$$

and the number density of the second beam in its rest frame is

$$\rho_{2_{Frame\,B2}} = \frac{N_2}{(2\pi)^{\frac{3}{2}}\bar{\sigma}_{x_2}\bar{\sigma}_{y_2}\bar{\sigma}_{z_2}} e^{-\frac{1}{2}\left[\left(\frac{\bar{x}_2}{\bar{\sigma}_{x_2}}\right)^2+\left(\frac{\bar{y}_2}{\bar{\sigma}_{y_2}}\right)^2+\left(\frac{\bar{z}_2}{\bar{\sigma}_{z_2}}\right)^2\right]}. \tag{3.51}$$

First we start by squaring both beams' x-components of force starting with the first beam. To simplify the expression, I made a change of variables to simplify the expression

$$F_{1x}^2 = \left(\int_0^\infty dq\, Q\left[\gamma_1\left(\cos(\theta)+\beta_1\beta_2(\cos^2(\theta)-\sin^2(\theta))\right)\frac{\bar{x}_1}{2\sigma_{\bar{x}_1}^2+q} - \sin(\theta)\frac{\bar{z}_1}{2\sigma_{\bar{z}_1}^2+q}\right]A_1(q)\right)^2$$

$$= \left(\int_0^\infty dq\, Q[a_1(q)+b_1(q)]\right)^2 = \int_0^\infty dq_1 \int_0^\infty dq_2\, (Q[a_1(q_1)+b_1(q_1)])(Q[a_1(q_2)+b_1(q_2)]) \tag{3.52}$$

$$= \int_0^\infty dq_1 \int_0^\infty dq_2\, Q^2[a_1(q_1)a_1(q_2)+a_1(q_1)b_1(q_2)+a_1(q_2)b_1(q_1)+b_1(q_1)b_1(q_2)].$$

Note that, due to the fact that each q produces a separate integral, the integration variables q_1 and q_2 are introduced. Expanding the square, each force squared acquires four terms. The first term expanded is

$$a_1(q_1)a_1(q_2) = \gamma_1^2\left(\cos(\theta)+\beta_1\beta_2(\cos^2(\theta)-\sin^2(\theta))\right)^2\frac{\bar{x}_1^2}{\left(2\sigma_{\bar{x}_1}^2+q_1\right)\left(2\sigma_{\bar{x}_1}^2+q_2\right)}A_1(q_1)A_1(q_2). \tag{3.53}$$

The second term is

$$a_1(q_1)b_1(q_2) = -\gamma_1\left(\cos(\theta)+\beta_1\beta_2(\cos^2(\theta)-\sin^2(\theta))\right)\sin(\theta)\frac{\bar{x}_1}{2\sigma_{\bar{x}_1}^2+q_1}\frac{\bar{z}_1}{2\sigma_{\bar{z}_1}^2+q_2}A_1(q_1)A_1(q_2). \tag{3.54}$$

The third term is

$$a_1(q_2)b_1(q_1) = -\gamma_1\left(\cos(\theta)+\beta_1\beta_2(\cos^2(\theta)-\sin^2(\theta))\right)\sin(\theta)\frac{\bar{x}_1}{2\sigma_{\bar{x}_1}^2+q_2}\frac{\bar{z}_1}{2\sigma_{\bar{z}_1}^2+q_1}A_1(q_1)A_1(q_2). \tag{3.55}$$

The fourth term is

$$b_1(q_1)b_1(q_2) = \sin^2(\theta)\frac{\bar{z}_1^2}{\left(2\sigma_{\bar{z}_1}^2 + q_1\right)\left(2\sigma_{\bar{z}_1}^2 + q_2\right)}A_1(q_1)A_1(q_2). \tag{3.56}$$

Applying the same to the second beam's x-component of the force we obtain

$$F_{2x}^2 = \left(\int_0^\infty dq\, Q\left[\gamma_2\left(cos(\theta) + \beta_1\beta_2(\cos^2(\theta) - \sin^2(\theta))\right)\frac{\bar{x}_2}{2\sigma_{\bar{x}_2}^2 + q} + \sin(\theta)\frac{\bar{z}_2}{2\sigma_{\bar{z}_2}^2 + q}\right]A_2(q)\right)^2$$

$$= \left(\int_0^\infty dq\, Q[a_2(q) + b_2(q)]\right)^2 = \int_0^\infty dq_1 \int_0^\infty dq_2\, (Q[a_2(q_1) + b_2(q_1)])(Q[a_2(q_2) + b_2(q_2)]) \tag{3.57}$$

$$= \int_0^\infty dq_1 \int_0^\infty dq_2\, Q^2[a_2(q_1)a_2(q_2) + a_2(q_1)b_2(q_2) + a_2(q_2)b_2(q_1) + b_2(q_1)b_2(q_2)].$$

Once again, we obtain four terms after the expansion. The first term is

$$a_2(q_1)a_2(q_2) = \gamma_2^2\left(cos(\theta) + \beta_1\beta_2(\cos^2(\theta) - \sin^2(\theta))\right)^2\frac{\bar{x}_2^2}{\left(2\sigma_{\bar{x}_2}^2 + q_1\right)\left(2\sigma_{\bar{x}_2}^2 + q_2\right)}A_2(q_1)A_2(q_2). \tag{3.58}$$

The second term is

$$a_2(q_1)b_2(q_2) = \gamma_2\left(cos(\theta) + \beta_1\beta_2(\cos^2(\theta) - \sin^2(\theta))\right)\sin(\theta)\frac{\bar{x}_2}{2\sigma_{\bar{x}_2}^2 + q_1}\frac{\bar{z}_2}{2\sigma_{\bar{z}_2}^2 + q_2}A_2(q_1)A_2(q_2). \tag{3.59}$$

The third term is

$$a_2(q_2)b_2(q_1) = \gamma_2\left(cos(\theta) + \beta_1\beta_2(\cos^2(\theta) - \sin^2(\theta))\right)\sin(\theta)\frac{\bar{x}_2}{2\sigma_{\bar{x}_2}^2 + q_2}\frac{\bar{z}_2}{2\sigma_{\bar{z}_2}^2 + q_1}A_2(q_1)A_2(q_2). \tag{3.60}$$

The fourth term is

$$b_2(q_1)b_2(q_2) = \sin^2(\theta)\frac{\bar{z}_2^2}{\left(2\sigma_{\bar{z}_2}^2 + q_1\right)\left(2\sigma_{\bar{z}_2}^2 + q_2\right)}A_2(q_1)A_2(q_2). \tag{3.61}$$

The y-component of the force for each beam is much simpler to square and for the first beam is

$$F_{1y}^2 = \left(\int_0^\infty dq\, Q \left[\gamma_1 \left(1 + \beta_1 \beta_2 cos(\theta)\right) \frac{\bar{y}_1}{2\sigma_{\bar{y}_1}^2 + q} \right] A_1(q) \right)^2$$

$$= \int_0^\infty dq_1 \int_0^\infty dq_2\, Q^2 \left[\gamma_1^2 \left(1 + \beta_1 \beta_2 cos(\theta)\right)^2 \frac{\bar{y}_1^2}{\left(2\sigma_{\bar{y}_1}^2 + q_1\right)\left(2\sigma_{\bar{y}_1}^2 + q_2\right)} \right] A_1(q_1) A_1(q_2). \tag{3.62}$$

and for the second beam is

$$F_{2y}^2 = \left(\int_0^\infty dq\, Q \left[\gamma_2 \left(1 + \beta_1 \beta_2 cos(\theta)\right) \frac{\bar{y}_2}{2\sigma_{\bar{y}_2}^2 + q} \right] A_2(q) \right)^2$$

$$= \int_0^\infty dq_1 \int_0^\infty dq_2\, Q^2 \left[\gamma_2^2 \left(1 + \beta_1 \beta_2 cos(\theta)\right)^2 \frac{\bar{y}_2^2}{\left(2\sigma_{\bar{y}_2}^2 + q_1\right)\left(2\sigma_{\bar{y}_2}^2 + q_2\right)} \right] A_2(q_1) A_2(q_2). \tag{3.63}$$

Now that we have both the densities and squared force components it would seem that we could integrate and now find the power, however we are not quite able to yet. Both the densities and squared force components are in terms of each beams' rest frame for their space-time coordinates. These need to be boosted and/or rotated before we perform the integral. To determine the correct space-time coordinate transformations we will begin in the detector frame of each beam labeled D_1 and D_2. These need to be rotated into the other beam's beam pipe frame using rotational matrices. The transformation from detector 1's frame to beam 2's primed frame is

$$\begin{bmatrix} x'_{B_2} \\ y'_{B_2} \\ z'_{B_2} \end{bmatrix} = \begin{bmatrix} \cos(\theta) & 0 & \sin(\theta) \\ 0 & 1 & 0 \\ -\sin(\theta) & 0 & \cos(\theta) \end{bmatrix} \begin{bmatrix} x_{D_1} \\ y_{D_1} \\ z_{D_1} \end{bmatrix} = \begin{bmatrix} x_{D_1}\cos(\theta) + z_{D_1}\sin(\theta) \\ y_{D_1} \\ -x_{D_1}\sin(\theta) + z_{D_1}\cos(\theta) \end{bmatrix}. \tag{3.64}$$

The transformation from detector 2's frame to beam 1's primed frame is

$$\begin{bmatrix} x'_{B_1} \\ y'_{B_1} \\ z'_{B_1} \end{bmatrix} = \begin{bmatrix} \cos(\theta) & 0 & -\sin(\theta) \\ 0 & 1 & 0 \\ \sin(\theta) & 0 & \cos(\theta) \end{bmatrix} \begin{bmatrix} x_{D_2} \\ y_{D_2} \\ z_{D_2} \end{bmatrix} = \begin{bmatrix} x_{D_2}\cos(\theta) - z_{D_2}\sin(\theta) \\ y_{D_2} \\ x_{D_2}\sin(\theta) + z_{D_2}\cos(\theta) \end{bmatrix}. \tag{3.65}$$

These are now in the beam pipe frame coordinates. They now need to be boosted into the beam rest frames. Each beam is moving along the z-axis with the first beam having velocity $\beta_1 c$ and the second beam having $-\beta_2 c$. Using Equation 3.17 and having $\beta_x = \beta_y = 0$ we get the following boost from the second beam's primed frame to its rest frame

$$\begin{bmatrix} c\bar{t}_2 \\ \bar{x}_2 \\ \bar{y}_2 \\ \bar{z}_2 \end{bmatrix} = \begin{bmatrix} \gamma_2 & 0 & 0 & \gamma_2\beta_2 \\ 0 & 1 & 0 & 0 \\ 0 & 0 & 1 & 0 \\ \gamma_2\beta_2 & 0 & 0 & \gamma_2 \end{bmatrix} \begin{bmatrix} ct'_{B_2} \\ x'_{B_2} \\ y'_{B_2} \\ z'_{B_2} \end{bmatrix} = \begin{bmatrix} \gamma_2\left(ct'_{B_2} + \beta_2 z'_{B_2}\right) \\ x'_{B_2} \\ y'_{B_2} \\ \gamma_2\left(z'_{B_2} + \beta_2 ct'_{B_2}\right) \end{bmatrix}. \tag{3.66}$$

Substituting Equation 3.58's result we obtain

$$\begin{bmatrix} c\bar{t}_2 \\ \bar{x}_2 \\ \bar{y}_2 \\ \bar{z}_2 \end{bmatrix} = \begin{bmatrix} \gamma_2\left(ct_{D_1} + \beta_2\left(-x_{D_1}\sin(\theta) + z_{D_1}\cos(\theta)\right)\right) \\ x_{D_1}\cos(\theta) + z_{D_1}\sin(\theta) \\ y_{D_1} \\ \gamma_2\left(-x_{D_1}\sin(\theta) + z_{D_1}\cos(\theta) + \beta_2 ct_{D_1}\right) \end{bmatrix}. \tag{3.67}$$

Using Equation 3.17 again and having $\beta_x = \beta_y = 0$ we get the following boost from the first beam's primed frame to its rest frame

$$\begin{bmatrix} c\bar{t}_1 \\ \bar{x}_1 \\ \bar{y}_1 \\ \bar{z}_1 \end{bmatrix} = \begin{bmatrix} \gamma_1 & 0 & 0 & -\gamma_1\beta_1 \\ 0 & 1 & 0 & 0 \\ 0 & 0 & 1 & 0 \\ -\gamma_1\beta_1 & 0 & 0 & \gamma_1 \end{bmatrix} \begin{bmatrix} ct'_{B_1} \\ x'_{B_1} \\ y'_{B_1} \\ z'_{B_1} \end{bmatrix} = \begin{bmatrix} \gamma_1\left(ct'_{B_1} - \beta_1 z'_{B_1}\right) \\ x'_{B_1} \\ y'_{B_1} \\ \gamma_1\left(z'_{B_1} - \beta_1 ct'_{B_1}\right) \end{bmatrix}. \tag{3.68}$$

Substituting Equation 3.59's result we obtain

$$\begin{bmatrix} c\bar{t}_1 \\ \bar{x}_1 \\ \bar{y}_1 \\ \bar{z}_1 \end{bmatrix} = \begin{bmatrix} \gamma_1\left(ct_{D_2} - \beta_1\left(x_{D_2}\sin(\theta) + z_{D_2}\cos(\theta)\right)\right) \\ x_{D_2}\cos(\theta) - z_{D_2}\sin(\theta) \\ y_{D_2} \\ \gamma_1\left(x_{D_2}\sin(\theta) + z_{D_2}\cos(\theta) - \beta_1 ct_{D_2}\right) \end{bmatrix}. \tag{3.69}$$

We now have the correct coordinate transformation for the squared force term but we still need to convert the coordinates of the densities from the beam rest frames to the detector frames. This can be done by boosting from the detector frame to the rest frame. Boosting from detector 1's frame to its rest frame transforms like

$$\begin{bmatrix} c\bar{t}_1 \\ \bar{x}_1 \\ \bar{y}_1 \\ \bar{z}_1 \end{bmatrix} = \begin{bmatrix} \gamma_1 & 0 & 0 & -\gamma_1\beta_1 \\ 0 & 1 & 0 & 0 \\ 0 & 0 & 1 & 0 \\ -\gamma_1\beta_1 & 0 & 0 & \gamma_1 \end{bmatrix} \begin{bmatrix} ct_{D_1} \\ x_{D_1} \\ y_{D_1} \\ z_{D_1} \end{bmatrix} = \begin{bmatrix} \gamma_1\left(ct_{D_1} - \beta_1 z_{D_1}\right) \\ x_{D_1} \\ y_{D_1} \\ \gamma_1\left(z_{D_1} - \beta_1 ct_{D_1}\right) \end{bmatrix} \tag{3.70}$$

Boosting from detector 2's frame to its rest frame transforms like

$$\begin{bmatrix} c\bar{t}_2 \\ \bar{x}_2 \\ \bar{y}_2 \\ \bar{z}_2 \end{bmatrix} = \begin{bmatrix} \gamma_2 & 0 & 0 & \gamma_2\beta_2 \\ 0 & 1 & 0 & 0 \\ 0 & 0 & 1 & 0 \\ \gamma_2\beta_2 & 0 & 0 & \gamma_2 \end{bmatrix} \begin{bmatrix} ct_{D_2} \\ x_{D_2} \\ y_{D_2} \\ z_{D_2} \end{bmatrix} = \begin{bmatrix} \gamma_2\left(ct_{D_2} + \beta_2 z_{D_2}\right) \\ x_{D_2} \\ y_{D_2} \\ \gamma_2\left(z_{D_2} + \beta_2 ct_{D_2}\right) \end{bmatrix} \tag{3.71}$$

Lastly, we must not forget that when boosting between the beam rest frame and beam pipe frame that the beams undergo a length contraction as in the following way

$$\bar{\sigma}_{x_1} = \sigma_{x_1}, \bar{\sigma}_{y_1} = \sigma_{y_1}, \bar{\sigma}_{z_1} = \gamma_1\sigma_{z_1}, \bar{\sigma}_{x_2} = \sigma_{x_2}, \bar{\sigma}_{y_2} = \sigma_{y_2}, \bar{\sigma}_{z_2} = \gamma_2\sigma_{z_2} \tag{3.72}$$

We now have everything that we need to perform the total power integrals. The x, y, z, and t integrals can be solved analytically whereas the q_1 and q_2 integrals need to be solved numerically.

3.1.2 Crossing Angle with Beam Tilt

If we also want to add beam tilt then there will need to be an additional rotation matrix for going from detector frames to beam pipe frames. Rotating from detector 1's frame to beam 2's primed frame transforms as

$$\begin{bmatrix} x'_{B_2} \\ y'_{B_2} \\ z'_{B_2} \end{bmatrix} = \begin{bmatrix} \cos(\varphi_2) & -\sin(\varphi_2) & 0 \\ \sin(\varphi_2) & \cos(\varphi_2) & 0 \\ 0 & 0 & 1 \end{bmatrix} \begin{bmatrix} \cos(\theta) & 0 & \sin(\theta) \\ 0 & 1 & 0 \\ -\sin(\theta) & 0 & \cos(\theta) \end{bmatrix} \begin{bmatrix} x_{D_1} \\ y_{D_1} \\ z_{D_1} \end{bmatrix}. \tag{3.73}$$

Performing the matrix multiplication yields

$$\begin{bmatrix} x'_{B_2} \\ y'_{B_2} \\ z'_{B_2} \end{bmatrix} = \begin{bmatrix} \left(x_{D_1}\cos(\theta) + z_{D_1}\sin(\theta)\right)\cos(\varphi_2) - y_{D_1}\sin(\varphi_2) \\ \left(x_{D_1}\cos(\theta) + z_{D_1}\sin(\theta)\right)\sin(\varphi_2) + y_{D_1}\cos(\varphi_2) \\ -x_{D_1}\sin(\theta) + z_{D_1}\cos(\theta) \end{bmatrix}. \tag{3.74}$$

Rotating from detector 2's frame to beam 1's primed frame transforms as

$$\begin{bmatrix} x'_{B_1} \\ y'_{B_1} \\ z'_{B_1} \end{bmatrix} = \begin{bmatrix} \cos(\varphi_1) & \sin(\varphi_1) & 0 \\ -\sin(\varphi_1) & \cos(\varphi_1) & 0 \\ 0 & 0 & 1 \end{bmatrix} \begin{bmatrix} \cos(\theta) & 0 & -\sin(\theta) \\ 0 & 1 & 0 \\ \sin(\theta) & 0 & \cos(\theta) \end{bmatrix} \begin{bmatrix} x_{D_2} \\ y_{D_2} \\ z_{D_2} \end{bmatrix}. \tag{3.75}$$

Performing the matrix multiplication yields

$$\begin{bmatrix} x_{B_1}^{'} \\ y_{B_1}^{'} \\ z_{B_1}^{'} \end{bmatrix} = \begin{bmatrix} \left(x_{D_2}\cos(\theta) - z_{D_2}\sin(\theta)\right)\cos(\varphi_1) + y_{D_2}\sin(\varphi_1) \\ -\left(x_{D_2}\cos(\theta) - z_{D_2}\sin(\theta)\right)\sin(\varphi_1) + y_{D_2}\cos(\varphi_1) \\ x_{D_2}\sin(\theta) + z_{D_2}\cos(\theta) \end{bmatrix}. \tag{3.76}$$

Once again we have to boost from the beam pipe frames to the beam rest frames using a Lorentz transformation. Boosting from beam 2's primed frame to its rest frame transforms as

$$\begin{bmatrix} c\bar{t}_2 \\ \bar{x}_2 \\ \bar{y}_2 \\ \bar{z}_2 \end{bmatrix} = \begin{bmatrix} \gamma_2 & 0 & 0 & \gamma_2\beta_2 \\ 0 & 1 & 0 & 0 \\ 0 & 0 & 1 & 0 \\ \gamma_2\beta_2 & 0 & 0 & \gamma_2 \end{bmatrix} \begin{bmatrix} ct_{B_2}^{'} \\ x_{B_2}^{'} \\ y_{B_2}^{'} \\ z_{B_2}^{'} \end{bmatrix} = \begin{bmatrix} \gamma_2\left(ct_{B_2}^{'} + \beta_2 z_{B_2}^{'}\right) \\ x_{B_2}^{'} \\ y_{B_2}^{'} \\ \gamma_2\left(z_{B_2}^{'} + \beta_2 ct_{B_2}^{'}\right) \end{bmatrix} = \begin{bmatrix} \gamma_2\left(ct_{D_1} + \beta_2\left(-x_{D_1}\sin(\theta) + z_{D_1}\cos(\theta)\right)\right) \\ \left(x_{D_1}\cos(\theta) + z_{D_1}\sin(\theta)\right)\cos(\varphi_2) - y_{D_1}\sin(\varphi_2) \\ \left(x_{D_1}\cos(\theta) + z_{D_1}\sin(\theta)\right)\sin(\varphi_2) + y_{D_1}\cos(\varphi_2) \\ \gamma_2\left(-x_{D_1}\sin(\theta) + z_{D_1}\cos(\theta) + \beta_2 ct_{D_1}\right) \end{bmatrix} \tag{3.77}$$

Boosting from beam 1's primed frame to its rest frame transforms as

$$\begin{bmatrix} c\bar{t}_1 \\ \bar{x}_1 \\ \bar{y}_1 \\ \bar{z}_1 \end{bmatrix} = \begin{bmatrix} \gamma_1 & 0 & 0 & -\gamma_1\beta_1 \\ 0 & 1 & 0 & 0 \\ 0 & 0 & 1 & 0 \\ -\gamma_1\beta_1 & 0 & 0 & \gamma_1 \end{bmatrix} \begin{bmatrix} ct_{B_1}^{'} \\ x_{B_1}^{'} \\ y_{B_1}^{'} \\ z_{B_1}^{'} \end{bmatrix} = \begin{bmatrix} \gamma_1\left(ct_{B_1}^{'} - \beta_1 z_{B_1}^{'}\right) \\ x_{B_1}^{'} \\ y_{B_1}^{'} \\ \gamma_1\left(z_{B_1}^{'} - \beta_1 ct_{B_1}^{'}\right) \end{bmatrix} = \begin{bmatrix} \gamma_1\left(ct_{D_2} - \beta_1\left(x_{D_2}\sin(\theta) + z_{D_2}\cos(\theta)\right)\right) \\ \left(x_{D_2}\cos(\theta) - z_{D_2}\sin(\theta)\right)\cos(\varphi_1) + y_{D_2}\sin(\varphi_1) \\ -\left(x_{D_2}\cos(\theta) - z_{D_2}\sin(\theta)\right)\sin(\varphi_1) + y_{D_2}\cos(\varphi_1) \\ \gamma_1\left(x_{D_2}\sin(\theta) + z_{D_2}\cos(\theta) - \beta_1 ct_{D_2}\right) \end{bmatrix} \tag{3.78}$$

The density coordinate transformation is also a bit more complicated because instead of just applying the boost between the two frames we also have to apply the tilt rotation. Rotating and boosting from detector 1's frame to beam 1's rest frame transforms as

$$\begin{bmatrix} c\bar{t}_1 \\ \bar{x}_1 \\ \bar{y}_1 \\ \bar{z}_1 \end{bmatrix} = \begin{bmatrix} \gamma_1 & 0 & 0 & -\gamma_1\beta_1 \\ 0 & 1 & 0 & 0 \\ 0 & 0 & 1 & 0 \\ -\gamma_1\beta_1 & 0 & 0 & \gamma_1 \end{bmatrix} \begin{bmatrix} 1 & 0 & 0 & 0 \\ 0 & \cos(\varphi_1) & \sin(\varphi_1) & 0 \\ 0 & -\sin(\varphi_1) & \cos(\varphi_1) & 0 \\ 0 & 0 & 0 & 1 \end{bmatrix} \begin{bmatrix} ct_{D_1} \\ x_{D_1} \\ y_{D_1} \\ z_{D_1} \end{bmatrix} = \begin{bmatrix} \gamma_1\left(ct_{D_1} - \beta_1 z_{D_1}\right) \\ x_{D_1}\cos(\varphi_1) + y_{D_1}\sin(\varphi_1) \\ -x_{D_1}\sin(\varphi_1) + y_{D_1}\cos(\varphi_1) \\ \gamma_1\left(z_{D_1} - \beta_1 ct_{D_1}\right) \end{bmatrix}. \tag{3.79}$$

Rotating and boosting from detector 2's frame to beam 2's rest frame transforms as

$$\begin{bmatrix} c\bar{t}_2 \\ \bar{x}_2 \\ \bar{y}_2 \\ \bar{z}_2 \end{bmatrix} = \begin{bmatrix} \gamma_2 & 0 & 0 & \gamma_2\beta_2 \\ 0 & 1 & 0 & 0 \\ 0 & 0 & 1 & 0 \\ \gamma_2\beta_2 & 0 & 0 & \gamma_2 \end{bmatrix} \begin{bmatrix} 1 & 0 & 0 & 0 \\ 0 & \cos(\varphi_2) & -\sin(\varphi_2) & 0 \\ 0 & \sin(\varphi_2) & \cos(\varphi_2) & 0 \\ 0 & 0 & 0 & 1 \end{bmatrix} \begin{bmatrix} ct_{D_2} \\ x_{D_2} \\ y_{D_2} \\ z_{D_2} \end{bmatrix} = \begin{bmatrix} \gamma_2\left(ct_{D_2} + \beta_2 z_{D_2}\right) \\ x_{D_2}\cos(\varphi_2) - y_{D_2}\sin(\varphi_2) \\ x_{D_2}\sin(\varphi_2) + y_{D_2}\cos(\varphi_2) \\ \gamma_2\left(z_{D_2} + \beta_2 ct_{D_2}\right) \end{bmatrix}. \tag{3.80}$$

3.2 Angular Spectral Distribution

From the generalized relativistic Larmor formula, a formula for the angular distribution can be found which is given in CGS units as

$$\frac{dP}{d\Omega} = \frac{e^2}{4\pi c}\frac{\left|\hat{\boldsymbol{n}} \times \left[(\hat{\boldsymbol{n}} - \boldsymbol{\beta}) \times \dot{\boldsymbol{\beta}}\right]\right|^2}{(1 - \hat{\boldsymbol{n}} \cdot \boldsymbol{\beta})^5} \tag{3.81}$$

where e is the elementary electrical charge and $\hat{\boldsymbol{n}}$ is the unit vector pointing from the charged particle to the observer.

However, we also have a spectral distribution therefore the energy distribution in frequency and solid angle in CGS units is

$$\frac{d^2I}{d\omega d\Omega} = \frac{e^2}{4\pi^2 c}\left|\int_{-\infty}^{\infty} \frac{\boldsymbol{n} \times \left[(\boldsymbol{n} - \boldsymbol{\beta}) \times \dot{\boldsymbol{\beta}}\right]}{(1 - \boldsymbol{\beta} \cdot \boldsymbol{n})^2} e^{i\omega\left(t - \frac{\boldsymbol{n} \cdot \boldsymbol{r}(t)}{c}\right)} dt\right|^2 \tag{3.82}$$

where ω is the angular frequency of the radiation and $\boldsymbol{r}(t)$ is the position of the particle.

Everything from the last section is all well and good but we are not interested in the total radiated power since we are only seeing a small fraction. We only care about the small solid angle, Ω, that our detector is at, which is very large compared to both 1/γ , and the deflection angle during the beam-beam collision. Effectively, the observation angle is constant during the entire process. This has led to the development of the "short magnet approximation", leading to a radiation formula [20]

$$\frac{d^2\boldsymbol{U}}{d\Omega d\omega} = \frac{r_0\gamma^2 f_i(\varphi,\theta)}{\pi c m_e c^2}\left|\widetilde{\boldsymbol{F}}\left(\frac{\omega(1+\gamma^2\theta^2)}{2c\gamma^2}\right)\right|^2 \quad where\ \Omega = sin\theta d\theta d\varphi \approx \theta d\theta d\varphi \tag{3.83}$$

where $\boldsymbol{U}$ is the two-dimensional vector (U_x, U_y), r_0 is the classical radius, $f_i(\varphi, \theta)$ is an angular function depending if we want the σ or π directions, m_e is the mass of an electron (and positron), ω is the angular frequency of the radiation, θ is the polar angle of the emitted radiation, and Ω is the solid angle.

The $\left|\widetilde{\boldsymbol{F}}\right|^2$ contains the Fourier transform

$$\widetilde{\boldsymbol{F}}(k) = \frac{1}{\sqrt{2\pi}} \int_{-\infty}^{\infty} \boldsymbol{F}(s) e^{-iks}\, ds \quad where\ k = \frac{\omega(1+\gamma^2\theta^2)}{2c\gamma^2} \tag{3.84}$$

where s is our path direction, $\boldsymbol{F}(s)$ is our deflecting force, and k is a function of the angular frequency of our light divided by $2c\gamma^2$. We would usually use s instead of z because the beams are curved slightly and not perfectly straight, but for our purposes we can approximate them as rigid beams, therefore $s \approx z$.

The angular functions for the σ polarization component with the electric field parallel or anti-parallel to the deflecting force and π polarization component with the electric field perpendicular to the deflecting force are

$$f_\sigma(\varphi, \theta) = \frac{[1-\gamma^2\theta^2\cos(2\varphi)]^2}{[1+\gamma^2\theta^2]^4} \quad and \quad f_\pi(\varphi, \theta) = \frac{[\gamma^2\theta^2\sin(2\varphi)]^2}{[1+\gamma^2\theta^2]^4} \tag{3.85}$$

The differential power for the σ polarization component is

$$\left(\frac{d^2\boldsymbol{U}}{d\Omega d\omega}\right)_\sigma = \frac{r_0\gamma^2}{\pi c m_0 c^2} \frac{[1-\gamma^2\theta^2\cos(2\varphi)]^2}{[1+\gamma^2\theta^2]^4} \left| \int_{-\infty}^{\infty} \boldsymbol{F}(z) e^{-iz\frac{\omega(1+\gamma^2\theta^2)}{2c\gamma^2}}\, dz \right|^2 \tag{3.86}$$

and the differential power for the π polarization component is

$$\left(\frac{d^2\boldsymbol{U}}{d\Omega d\omega}\right)_{\pi} = \frac{r_0\gamma^2}{\pi c m_0 c^2}\frac{[\gamma^2\theta^2\sin(2\varphi)]^2}{[1+\gamma^2\theta^2]^4}\left|\int_{-\infty}^{\infty}\boldsymbol{F}(z)e^{-iz\frac{\omega\left(1+\gamma^2\theta^2\right)}{2c\gamma^2}}dz\right|^2 \tag{3.87}$$

Integrating Equations 3.86 and 3.87 will give us the power for our solid angle for both the parallel/antiparallel and perpendicular polarizations.

3.3 Results

Our numerical program calculates total power, differential power, and luminosity from the previous sections. First we want to characterize the observed yield in the LABM, for beam conditions such as in Table 2.1 (nominal SuperKEKB conditions).

At nominal conditions, and assuming maximally overlapping beams, the total power emitted is 1224W (LER) and 2033W (HER). Each LABM window will be illuminated by $5 * 10^{10}$ eV (LER) and $7.8* 10^{10}$ eV (HER). Further, we have computed that the extra force components in the x-direction create extra power in the x-polarization. In the collinear case, the total beamstrahlung is unpolarized if the beams collide perfectly [19]. However, we find that at SuperKEKB the total power is polarized such that $\frac{U_x}{U_y} = 2.89$ (LER) and 2.93 (HER).

At large angle, where the LABM detector works, the polarization ratio increases to 5.21 (LER) and 5.37 (HER) . The total number of photons striking each mirror in the optical band of interest are $1.37 * 10^{10}$ (LER) and $2.00 * 10^{10}$ (HER). These numbers, while large and certainly sufficient to operate the device successfully, are by themselves not enough. In the next chapter the detector distortions (acceptance, spectral efficiency) are calculated. These values are all summarized below in Table 3.1.

	LER	HER
Total Power (W)	1224	2033
Illumination (eV)	$5*10^{10}$	$7.8*10^{10}$
Collinear U_x/U_y	2.89	2.93
Large Angle U_x/U_y	5.21	5.37
Total Photons/Mirror	$1.37*10^{10}$	$2.00*10^{10}$

Table 3.1: Beamstrahlung Calculation Results

The method of relating beamstrahlung observables to wasted luminosity was described in Section 2.4. From the beamstrahlung four observed powers, we construct asymmetries which are specific to a given beam-beam mismatch, and the relation between wasted luminosity from Section 2.4 [19] and asymmetries is studied. The main goal of my calculations was to prove that sensitivity to lost luminosity was maintained, compared to the original paper, which only discussed collinear beams.

Using the beam parameters of Table 2.1 and the beamstrahlung detector parameters of Table 2.2, we have calculated the new asymmetries (triangles), when U_x is normalized further by the factors of 5.21 and 5.37 found above. We superimposed them to the results of Ref.[19] (black dots). The results show nearly identical sensitivity in the collinear and non-collinear case.

This is crucial for two reasons: first, in the case of beam-beam offset (A_1 in Fig. 3.1), another beam monitor is able to measure such offset. Therefore, it will be possible to cross check the devices against each other. Also, years of experience with automatic beam-beam feedback show that in the noisy accelerator environment false positives abound, and spoil any feedback system based on a single monitor.

Second, the accurate observation of defocusing of one beam (A_2 in Fig. 3.1), is by far the most crucial in this project. It is because of A_2 that Japanese funding authorities decided to fund Wayne State to build this device. The observation that sensitivity to beam bloating is preserved in the non-collinear case is the main result of this chapter. In Chapter 4, we will design, build,

and analyze a detector that will be able to reconstruct the true photon fluxes at the mirrors to detect these beam imperfections.

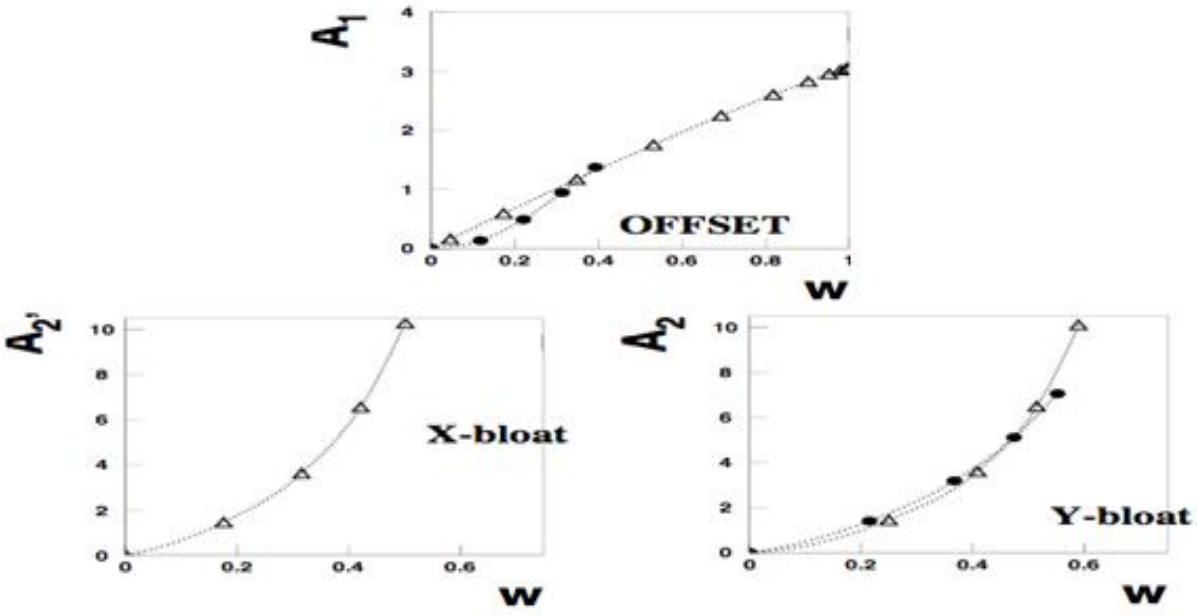

Figure 3.1: Asymmetries vs. Waste Parameter

Chapter 4 : Optics Box

As described in Chapter 3, I created a program that will calculate based on current theory exactly how much beamstrahlung should be radiated. Using the most general formula I can even focus just on the solid angle that our detector will be able to see and can determine the amount of power in different wavelength bands and polarizations. In this Chapter the instrument to detect and analyze beamstrahlung is discussed. I have made numerous contributions to the design and calibration of the instrument.

4.1 Piping Path and Elbows

Each beam of electrons/positrons travels around their own circular beam pipe in opposite directions. When the beam pipes cross the electron and positron beams collide and create the events we are interested in. Our detection is at an angle of about 10 mrad . In Figure 4.1 below, each pipe has two viewports; one on top and one on bottom. Each viewport has a 45 degrees mirror directly across from it so that the beamstrahlung radiation will hit the mirror and reflect across and into the viewport. There is a slight time delay for each beam since there is a small difference in distance for the light to travel but that can easily be calculated. The viewports are vacuum flanges with a quartz window in the center that allows the light to pass through with great efficiency.

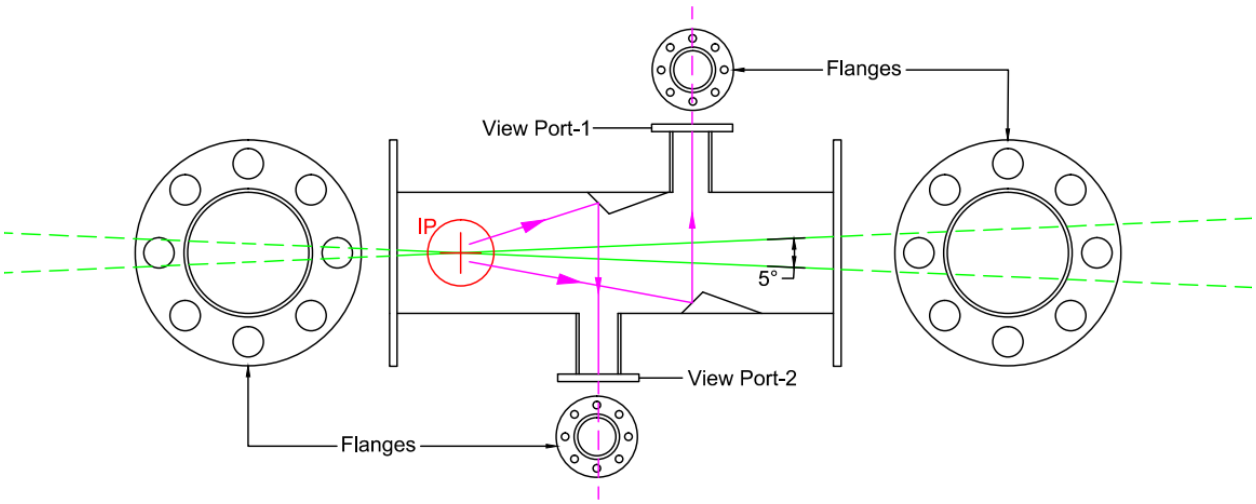

Figure 4.1: Beam Pipe Viewports

The next step is getting this light out and away from this high radiation zone near the beam pipe and to our detector to be analyzed. This is done through a series of pipes and elbow joints containing mirrors. The aluminum pipes have all been black anodized to help decrease the reflectivity. The first elbow, the primary elbow, connects 2 inch diameter pipe with 2 inch diameter pipe with a remotely controlled 45 degree mirror using a controller and stepper motors. This will allow us to make fine adjustments every so often in case there is any drift from bumping, small imperfections, earthquakes, etc. The schematic diagram of the primary elbow can be seen in Figure 4.2.

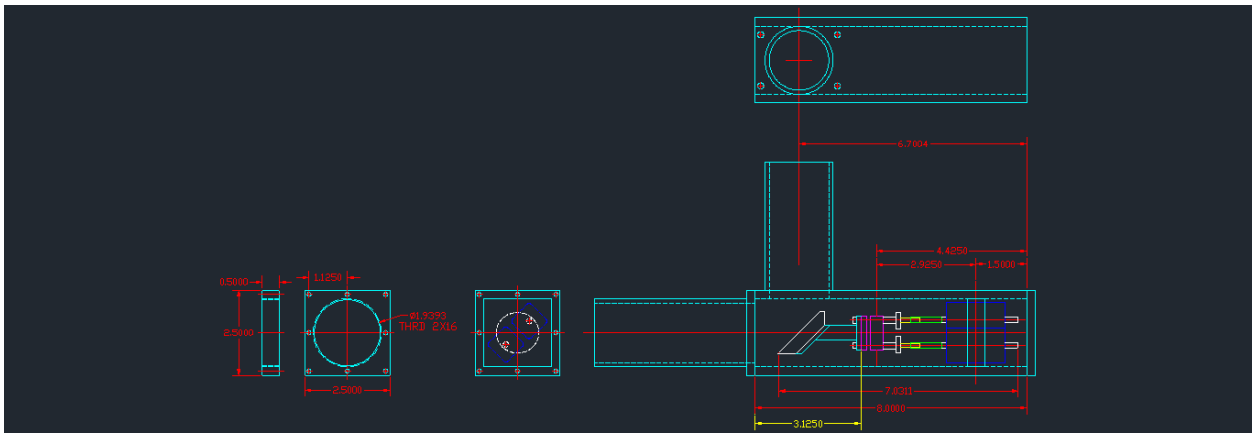

Figure 4.2: Primary Elbow Schematic

Once the light reflects off of the mirror and leaves the primary elbow it then travels down more black anodized aluminum piping to the second elbow. This elbow is different from the primary elbow in two important ways. First, the 45 degree mirror in this elbow is slightly larger and is not remotely controlled. It will be aligned once at installation. The other difference in this elbow is somewhat of a pipe adapter since 2 inch diameter pipe is coming into it, however we leave the elbow with 4 inch diameter pipe.

The light continues along the pipe pathway for another three mirrored elbows each connecting 4 inch diameter pipe with 4 inch diameter pipe until finally it reaches the optics box as shown in Figure 4.3.

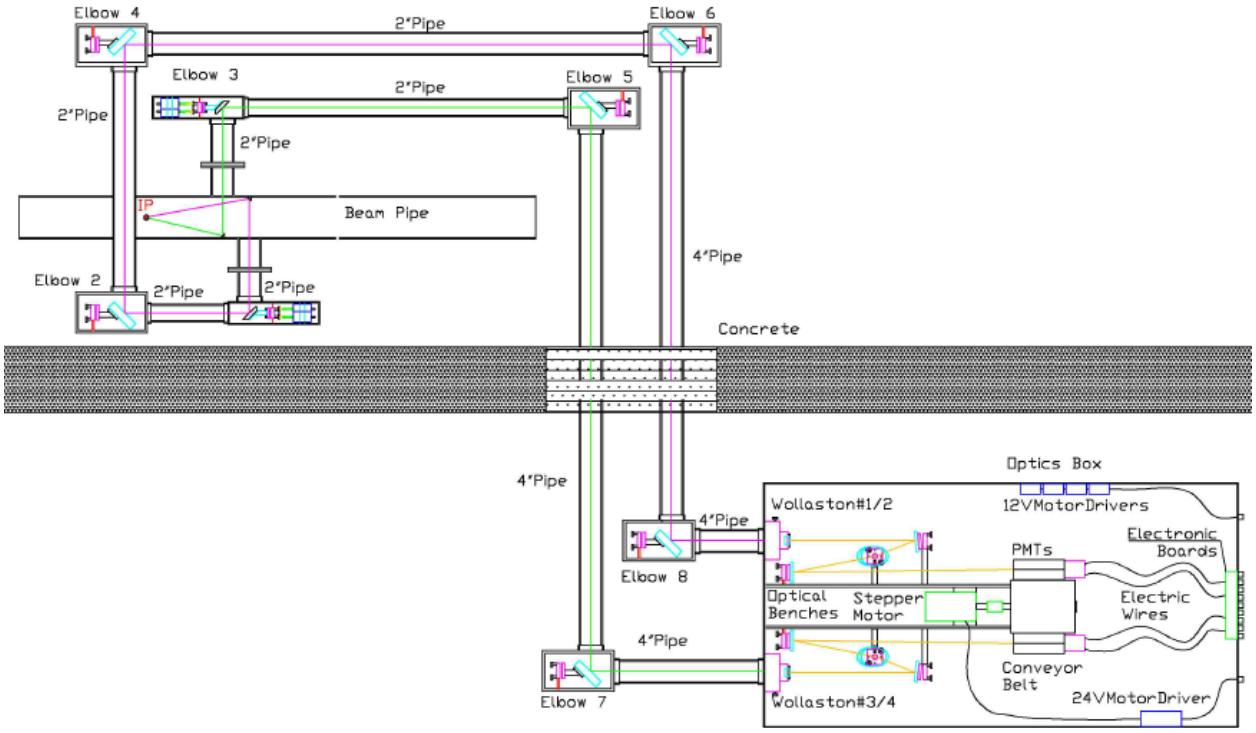

Figure 4.3: Full Optical Path

Each pipe carries the light of one viewport. Both beams of light are unpolarized and since our calculation shows that polarization is necessary to understand beam-beam mismatches we should definitely also separate polarizations. We do this with a Wollaston prism at the entry window of each pipe into the box. The Wollaston prism splits the incoming light into perpendicular and parallel polarized beams. The splitting angle is approximately ± 10 degrees from the midline of the optics box with small corrections.

This now polarized light reflects off a mirror and then reflects off another mirror until it eventually hits a ruled reflective grating. This grating unlike a mirror will split the light into many diffraction peaks generating several different rainbow-like spreads. As shown this spread will then travel across the box to be eventually collected and focused so that different

bandwidths can be detected independently using photomultiplier tubes. I will discuss the rest of the design and all of its elements in the next sections.

4.2 Photomultiplier Tubes

A photomultiplier tube (PMT) is a vacuum tube that is specially designed to take a signal of photons and amplify it into an electrical current that our instruments can discriminate and analyze. These have been used for many years in nuclear and particle physics due to several important factors. First, they have a very fast response time of the order of nanoseconds. This allows for nearly seamless data collection with a very small recovery period (dead time). This is very important since we want to have as little down time as possible so that we don't miss any photons. Secondly, they have very little noise compared to other possible devices that could be used to measure the light. Some measurements are very faint and a high amount of noise will drown the measurement. Lastly, PMTs have a very high gain, turning an electron liberated by a photon into a million electrons, which produce a usable electric signal. This means that each photon can be counted.

A photomultiplier tube works by a high energy photon impacting on a coated glass surface, a photocathode to generate an electron, a series of dynodes to cause the multiplicative effect, and finally an anode to collect the current as shown in Figure 4.4.

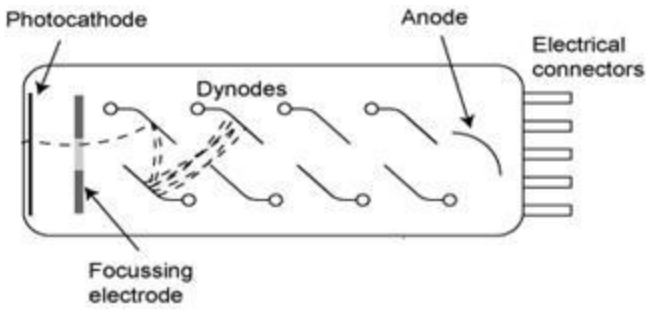

Figure 4.4: Inside a Photomultiplier Tube

The coated glass surface takes advantage of an important discovery of the twentieth century known as the photoelectric effect. Essentially a high energy photon can strike a material and the material will release an electron. One can only lower the energy of the photon so much until eventually there will not be enough energy to kick out an electron for that specific material. The maximum kinetic energy of the emitted electron is

$$K_{max} = E_\gamma - \varphi = hf - \varphi \tag{4.1}$$

where E_γ is the energy of the photon, h is Planck's constant, f is the frequency of the incident photon and φ is the work function of the material.

The coating is a super thin layer, only several molecules thick, of Caesium-activated Gallium Arsenide. Other photomultiplier tubes use different coatings, however since our wavelength range of interest is between 350 and 650 nanometers this type of coating is best suited for that range. The glass window also functions as a filter by blocking out any light of wavelength lower than close to our lower wavelength bound. This type of glass is called Borosilicate glass.

As long as the energy of the incident photon is greater than the work function of the coating then a single electron will be kicked out. This electron then is directed by a focusing

electrode towards the first of twelve dynodes. A dynode is just one of the many electrodes that will be used to multiply the electrical signal of the first electron. Each dynode down the chain has progressively higher positive voltage, usually around 100 volt increments. The initial electron has the energy of the photon minus the work function as shown in Equation 4.1 and accelerates by the electric field produced from the voltage towards the first dynode. When the electron hits the first dynode it has gained more energy and thus creates more electrons through secondary emission. These in turn accelerate toward the second dynode which creates even more electrons and so on. Eventually the electrons reach the anode at the end of the chain creating a sharp electrical pulse and the current exits out the voltage divider in the back of the PMT, through a signal cable that leads to our electronics. Assuming each dynode on average creates the same number of new electrons then

$$N_e = n^d \tag{4.2}$$

gives the estimated final number of electrons from the dynode cascade chain where N_e is the number of electrons at the end, n is the average number of new electrons made at each dynode, and d is the number of dynodes. Typically, around 3 new electrons are created at each dynode and our PMTs have 12 dynodes which gives us a total of $3^{12} = 10^6$ or a million electrons at the end all from just one initial electron.

All of this makes photomultiplier tubes sound great and easy to use, but there are some things that first need to be taken care of. Vacuum tubes can be a bit random sometimes and not every photomultiplier tube, even of the same type, necessarily has the same output for an identical signal. Therefore, determining the relative efficiencies of our PMTs and other parameters should allow for more accurate data and analysis.

4.2.1 PMT Plateaus

The first thing that is needed is to determine the optimal voltage to power the photomultiplier tubes with and the optimal voltage threshold for our signal to be used in our electronics arrangement. To facilitate this, we were in need of a perfectly dark enclosure that the PMTs could reside in and could function as our experimental zone. Therefore we built a large wooden black box with two windows on the side for easy access and a removable door on one of the ends. The box was also completely wrapped in aluminum foil to act as a Faraday cage which effectively blocks external electrical noise that could tamper with our measurements. Figure 4.5 shows a photo of the dark enclosure.

Figure 4.5: Dark Experimental Enclosure

In the removable door, two holes were bored through the wood to allow the cabling to exit the box that was attached to our circular cylinders that each had four PMTs arranged in a ring. The high voltage cabling was attached to a voltage divider so that each PMT received the

same amount of voltage to make sure that everything is equal. The signal cables were also wrapped in aluminum foil to minimize external noise.

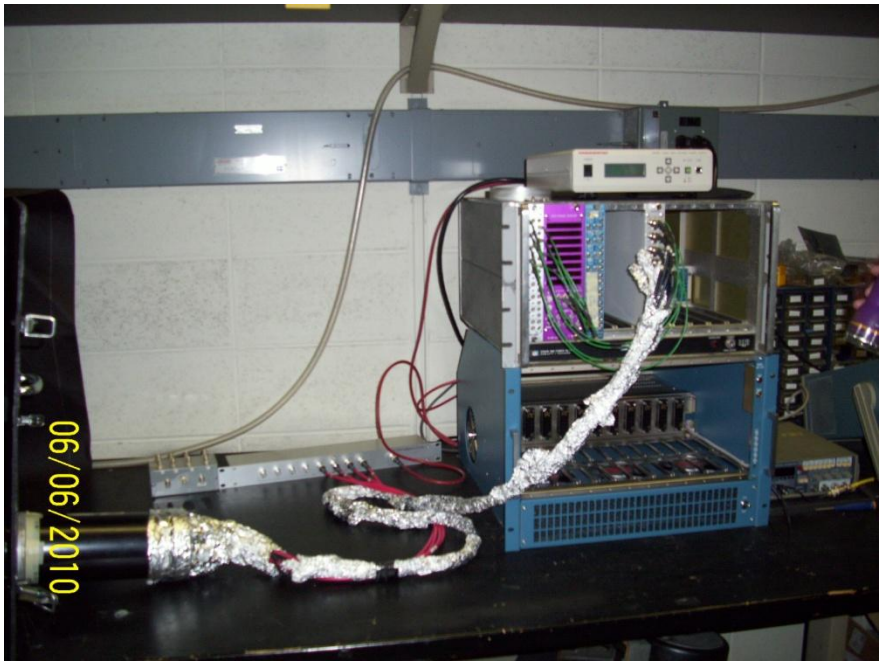

Figure 4.6: Electronics Setup

The signal cabling eventually reaches our electronics setup which consists of a 8-channel discriminator, an amplifier, and a visual scaler which can all be seen in Figure 4.6 with the high voltage power supply on top of everything. The analog signal is first amplified about ten times, then it is fed to the discriminator. The discriminator is an electronic comparator. It uses a variable voltage threshold (around 30mV in our case, corresponding to a 3mV threshold on the original pulse). Any incoming signal with a voltage below this threshold would get ignored and no pulse would be generated. Otherwise, when the signal meets the threshold or exceeds it the discriminator outputs a digital signal.

The final step for the signal is to the visual scaler. It is essentially a digital readout of the photon count over a period of time. There is the option to have the scaler automatically start and

stop using a signal gate which we take advantage of with a function generator. This way each trial we perform will have the exact same amount of time so that we can trust the counts to be reliable each trial. We generally take the count in ten second intervals therefore the count rate is the count divided ten.

The first operational step was to find the optimal threshold voltage for the discriminator. If we set the threshold too high then we will not only lose the noise but also some or all of the signal. Conversely, if we set the threshold too low then our signal will be mired with noise. We tested five different voltage thresholds starting at 20 mV and increasing by 5 mV all of the way up to 40 mV. Figure 4.7 shows the graphs of the data we collected.

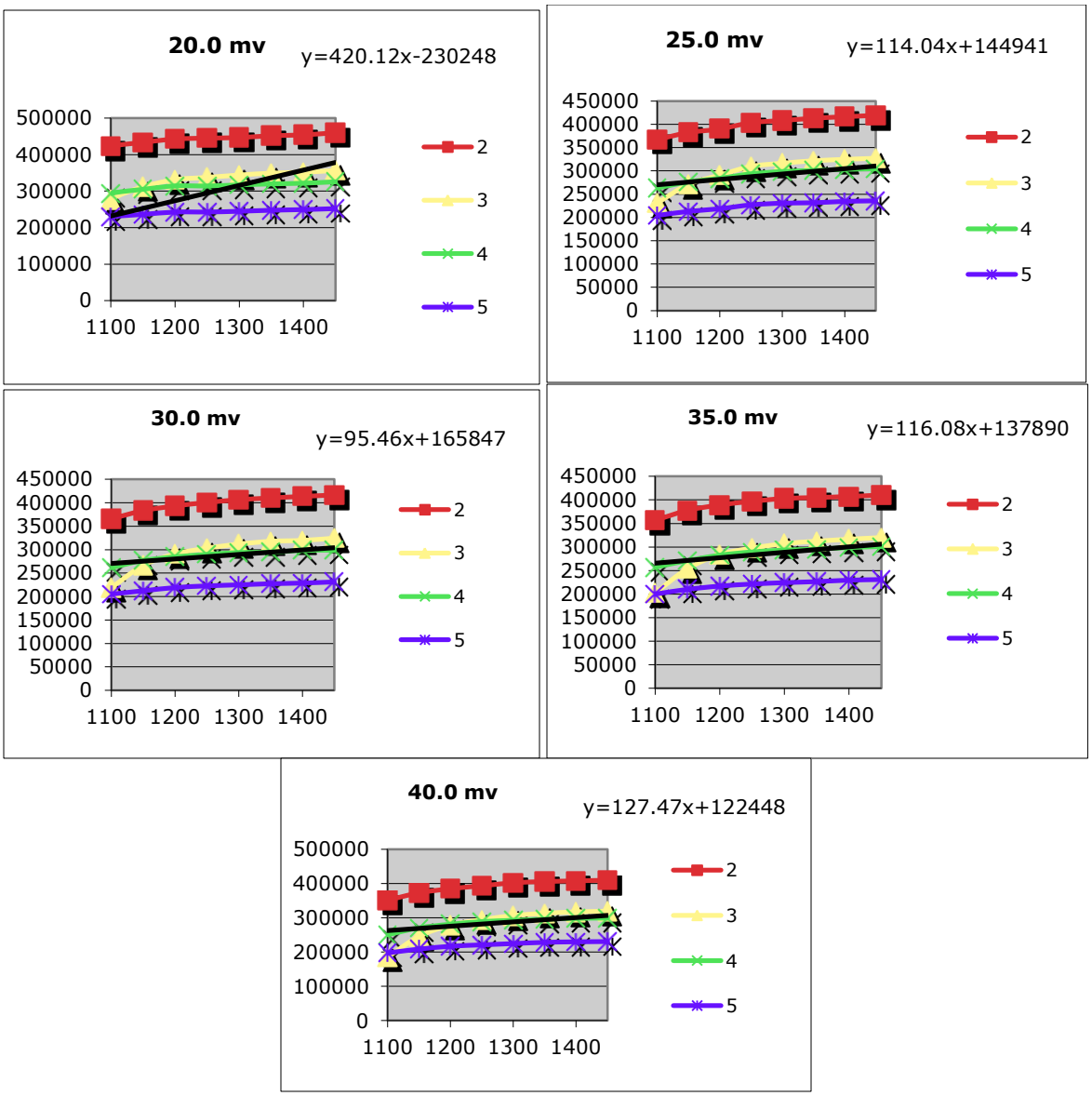

Figure 4.7: Counts vs. Voltage for Multiple Threshold Voltages

Each colored line represents the number of counts over a ten second interval for photomultiplier tubes labeled 2 through 5. For each voltage threshold being tested, the starting high voltage was always 1100 volts and would be incremented 50 volts every measurement up to a voltage of 1450 volts. Going any higher with the voltage risks burning out and destroying the PMTs. To find the optimal voltage threshold we want to first find the average count between the

four photomultipliers. Next we perform a linear regression on the average count function to find the best fit line. The best fit line with the smallest slope is the optimal threshold voltage which as you can see from the graphs is 30 mV with a slope of 95.46.

Having found the optimal threshold voltage for the discriminator we next need to find the optimal high voltage to supply to the PMTs. This voltage will be where the flattest section of the graph is located, which is called the plateau. Looking at our 30 mV graph one can see that the optimal high voltage is 1350 volts. Given the similar slopes, all our PMTs work with a voltage of 1350 Volts and a threshold of 3mV.

4.2.2 PMT Spectral Response

We've found both the optimal threshold voltage and the optimal high voltage from the power supply for the PMTs, but now we need to know if there are any differences in counting for different colors. To test this we used a mercury lamp source, which provides several well separated atomic lines, and used several of the emission lines to test the relationship between wavelength and count. We used ambient light as a control and the 340 nm, 482 nm, and 562 nm emission lines. Rather than just use the ideal 1350 volts for the high voltage supplied to the photomultipliers, we decided to test the entire voltage range once again starting from 1100 volts and adding 50 volts each time until reaching 1450 volts.

The data we collected and analyzed can be seen in Figure 4.8. To make the graphs more clear all three of the wavelength counts were normalized against the ambient light count. Also, the dark noise was subtracted out of each actual count since it is systemic background and can be ignored. You will notice that the 340 nm light has nearly no counts for all four PMTs compared

to ambient light. This makes sense since it is 10 nm below the PMT range. Next, the 482 nm light only has about 10-12% of the counts than the ambient light has. The 562 nm wavelength light on the other hand has around 30-31% of the counts as the ambient light. Therefore, it is easy to see that the photomultipliers behave differently for different wavelengths of light, but, crucially, they appear to have very similar spectral sensitivity.

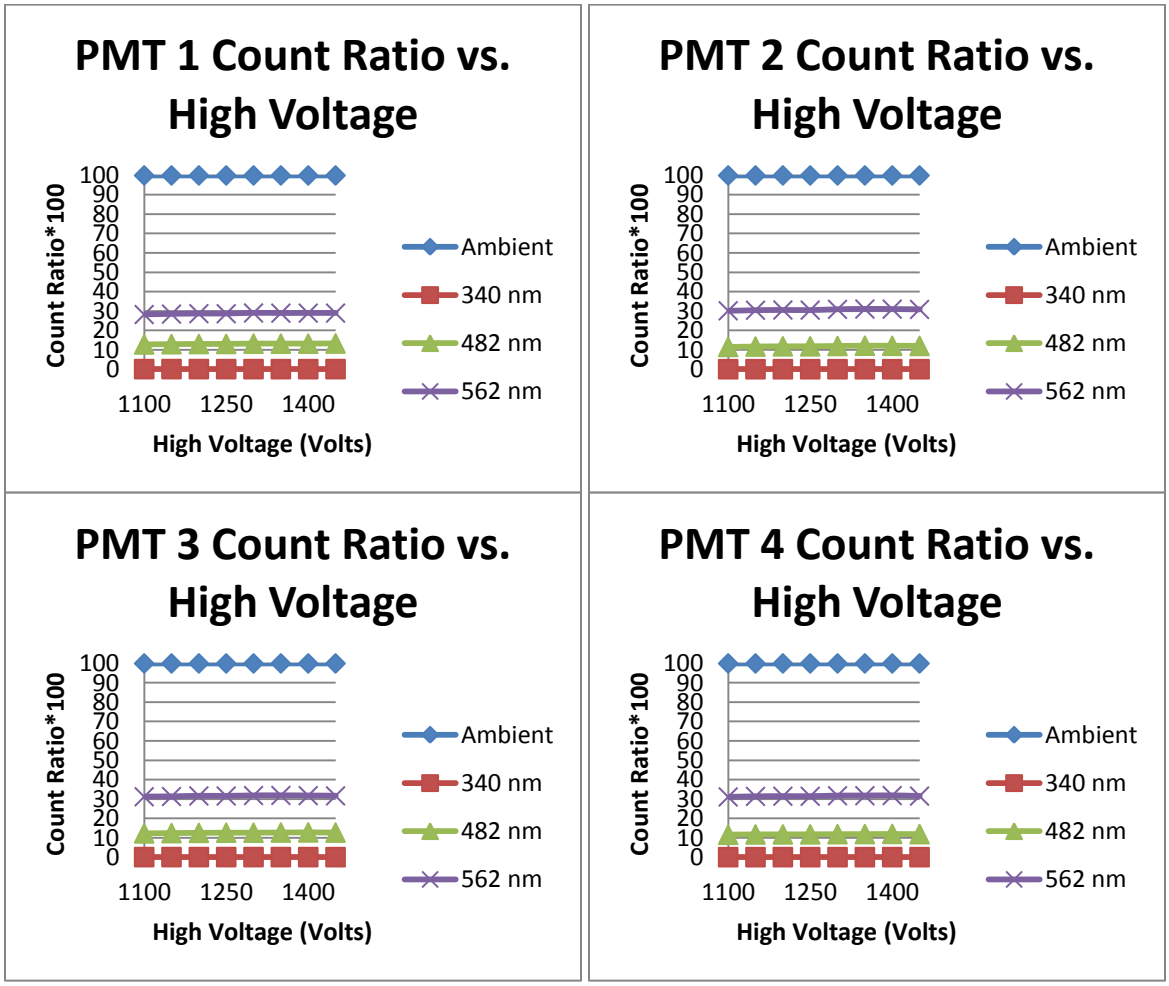

Figure 4.8: Count Ratios vs. High Voltages for Different PMTs

4.2.3 PMT Characterization

If the PMTs have the same spectral sensitivity, one can expect that they will have the same relative efficiency at all wavelengths. To answer this question we need to characterize all of our PMTs. To do this we need to have all parameters fixed and only change PMTs one at a time and see how the count varies. One PMT will be declared the master PMT which all counts will be compared against. In other words, this PMT will connect all of the other PMTs to each other and we will have a map of how each PMT behaves in the group.

To accomplish this we developed a robust experimental method using 16 photomultipliers at once. These photomultipliers were arranged in a 4x4 matrix centered within our dark box enclosure as shown in Figure 4.9.

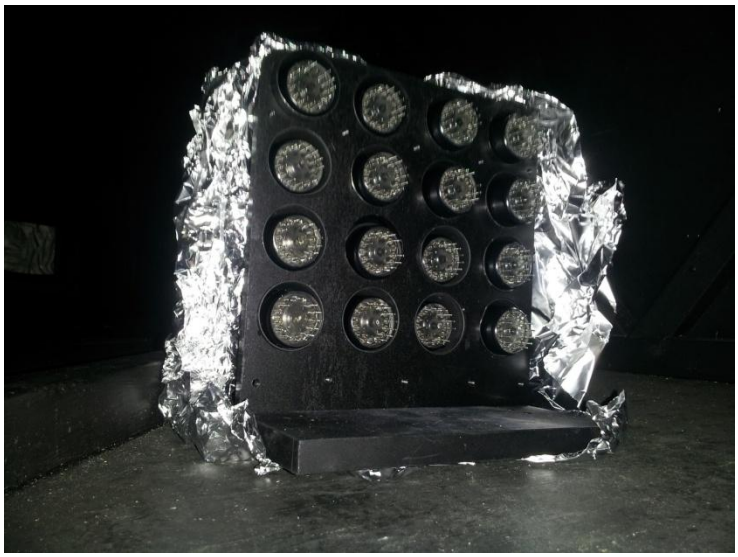

Figure 4.9: PMT Characterization 4x4 Matrix

Light will enter through a pinhole on the back door and will travel across the box and diffuse on a frosted glass panel. This diffuse light will be detected by the matrix of PMTs. This

was done with various light sources and showed that the relative efficiency of the PMTs is the same at different wavelengths.

4.3 Grating Calculations

Before we could finish designing the optics box it was crucial to figure out how long the optical table should be since we had to cut the metal and build it. The length was determined by two factors. The first important factor is the number of grooves per millimeter of the ruled grating. The diffracted angle off of the grating depends on the inverse of this quantity. The other important factor is the diameter of the PMTs. Each optical path ends in an array of four PMTs in a single column. The rainbow spread of the wavelengths of light for the range that we are interested in, specifically 350 nm - 650 nm, can be no larger than this quantity or else some of the light we want will end up outside of our view. If the spread is too tight however, we may see wavelengths outside the preferred range or even some of the PMTs may not even be illuminated.

Diffraction gratings can be either reflective or transmissive in their behavior with light. A grating can be imagined as a double-slit experiment except rather than only two slits the grating has many parallel slits. The equations governing the grating reflectivity are the same regardless of type. White light can be separated into different wavelengths and the maxima will occur according to

$$dsin(\theta_m) = m\lambda. \tag{4.3}$$

Here d is the inverse of the grating spacing, θ_m is the angle between the normal of the grating and the diffracted light, m is the order, and λ is the wavelength of light.

As one can see whenever light directly transmits or simply reflects then normal refraction as with a lens or reflection as with a mirror occurs. This is when $m = 0$, so it is the zeroth order peak. When light is not normally incident, Equation 4.3 becomes

$$d\big(sin(\theta_i) + sin(\theta_m)\big) = m\lambda \tag{4.4}$$

where θ_i is the angle of incidence.

Solving for the diffraction angle, we obtain

$$\theta_m = \sin^{-1}\left(\frac{m\lambda}{d} - \sin(\theta_i)\right). \tag{4.5}$$

The angle of the light is only dependent on the groove separation and not on the surface topology. This fact can be used to focus most of the diffracted light's energy into an order other than zeroth based on a specialized topology. A diffraction grating could have rulings or blazes which usually are triangular in shape as shown in Figure 4.10.

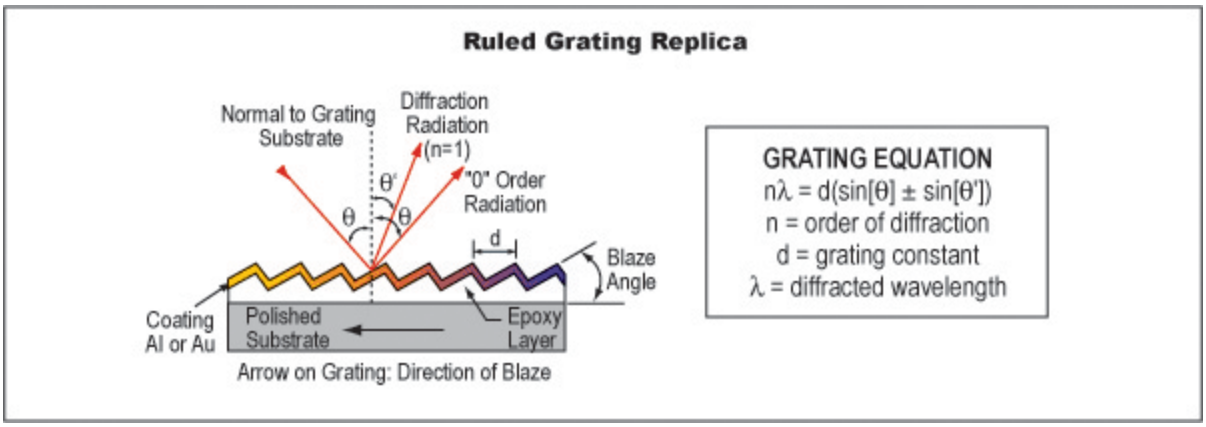

Figure 4.10: Reflective Ruled Grating

The most efficient diffraction occurs when the incident angle is at the blaze angle γ and the wavelength is at the blaze wavelength. Since we are using a select spectral range and have a

small set of possible incidence angles we can find a specialized diffraction grating that will boost our efficiency rather than just a one-size-fits-all solution. A ruled reflective grating has more stray light than a normal holographic grating, but we are more concerned about a very high peak efficiency which a ruled grating will have.

The diffracted angle can then be used to find the heights of the different wavelengths

$$h = xtan(\theta_m) \tag{4.6}$$

where h is the height from the midline of the point at which the diffracted light is leaving the grating and x is the horizontal distance from the PMT array to the point of contact of the light on the grating.

To get our desired spectral spread we will need the maximum/minimum wavelength to hit the top of the highest PMT in the array using

$$\left|h_{top/bottom\ PMT} - h_{light\ point}\right| = \left|x_{PMT} - x_{light\ point}\right| \tan\left(\sin^{-1}\left(\frac{\lambda_{min/max}}{d}\right) - \theta_i\right) \tag{4.7}$$

where the vertical distance $\left|h_{top/bottom\ PMT} - h_{light\ point}\right|$ is the difference from the top of the topmost PMT or the bottom of the bottommost PMT and where the light hits the grating. The horizontal distance $\left|x_{PMT} - x_{light\ point}\right|$ is the difference between the photomultipliers and the point at which the light hits the grating. As for the wavelengths our minimum wavelength will hit the top of the topmost PMT and the maximum wavelength will hit the bottom of the bottommost PMT for the parallel polarization. The other polarization will look like a mirror image of this with the minimum wavelength above the maximum wavelength.

Another important item to figure out was the angles of incidence, reflection, and diffraction of the ruled grating and how the width of the square beams change. Figure 4.11 shows a schematic of the ruled grating with light coming on and off of it.

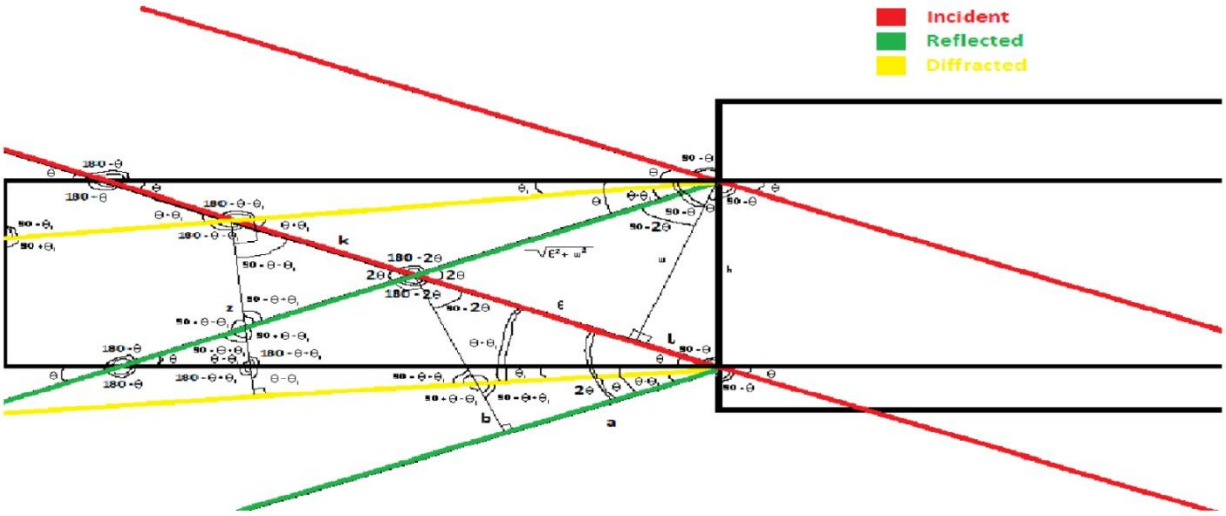

Figure 4.11: Diagram of Light at Grating Surface

The square beam drawn in red hits the ruled grating from above. The zeroth order peak comes off at an angle of $\theta_i = \theta_r$ from the horizontal which is drawn as the green square beam heading downwards and to the left. The first order peak diffracts off the ruled grating at angle θ_m and is drawn as the yellow square beam heading down and to the left. As expected the width of the incident square beam W_i and the width of the reflected square beam W_r are the same, however the diffracted square beam W_d is of different width

$$W_d = W_i \frac{\cos(\theta_m)}{\cos(\theta_i)} \; where -\frac{\pi}{2} < \theta_m < \frac{\pi}{2} \; and \; 0 \leq \theta_i < \frac{\pi}{2}. \tag{4.8}$$

To better understand this behavior we can substitute Equation 4.5 in for θ_m which leads to

$$W_d = W_i \frac{\cos\left(\sin^{-1}\left(\frac{m\lambda}{d} - \sin(\theta_i)\right)\right)}{\cos(\theta_i)}. \tag{4.9}$$

One can easily see that for non-negative orders the diffracted width varies from 0 to infinity. For a given $d, m,$ and λ as θ_i increases so does W_d and when $m = 0$ the diffracted width is identical to the incident width as previously stated.

Using these two pieces of information we can calculate the distance required for the correct spectral spread. This will be an absolute minimum for how long the optics box should be made since if it were any smaller or larger the 300 nm spread that we desire will not be so. We've calculated that the distance from the screw hole for the ruled diffraction grating's post should be 19.75 inches and we will use a 1200 grooves per millimeter grating that is optimized for 500 nm light which is the exact midpoint of our spectral range.

4.4 Laser Testing with First Optics Box

Now that we have many of the constraints that our optics box has to satisfy we can begin construction. The optics box will be made out of sheet aluminum that will be black anodized to suppress unintended reflections of light. The box will be split into two identical halves; one for the light exiting the beam pipe from the top and one for the light exiting the beam pipe from the bottom. The front face of the optics box showing the two entry ports is shown in Figure 4.12.

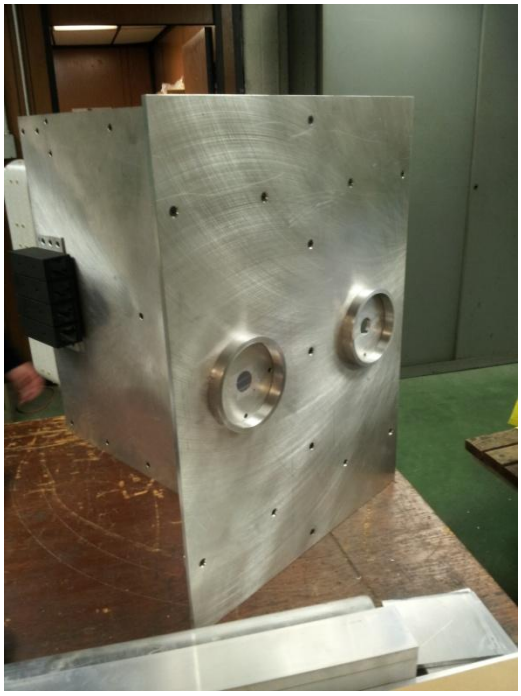

Figure 4.12: Front Face of Optics Box with Both Entry Ports

Each half will also be split into nearly identical halves; one half for perpendicular polarized light and the other half for parallel polarized light (with respect to the half plane of the Wollaston prism). Therefore, there are a total of four optical paths. Each of these paths will have two elliptical mirrors and a ruled diffraction grating which will eventually send the light to a column of photomultiplier tubes. The inside of the optics box is shown in Figure 4.13.

Figure 4.13: Inside of Optics Box

The completed box is then black anodized to help reduce any stray light that may result. Where the sides of the optics box meet, we have installed electromagnetic shielded stripping so that no electromagnetic radiation can seep in or out of the optics box. When all sealed the optics box is very dark internally thus providing a perfect environment for the experiment. There are now two completed optics boxes with one each going on either side of the Belle II detector. The first completed optics box is shown in Figure 4.14.

Figure 4.14: First Completed Optics Box

4.5 Conveyor Belt Motor Controls

Even though we are using four 4x1 arrays of photomultipliers per optics box there needs to be an efficient way to check the PMTs against each other. Once the optics box is installed, it rarely will be opened back up if ever. Therefore, manually swapping the photomultipliers as before will not be an acceptable method. Since the optics box can't be opened we will need to switch the PMTs remotely. To do this we have decided to attach the photomultipliers and their mu shields to a conveyor belt as shown in Figure 4.15.

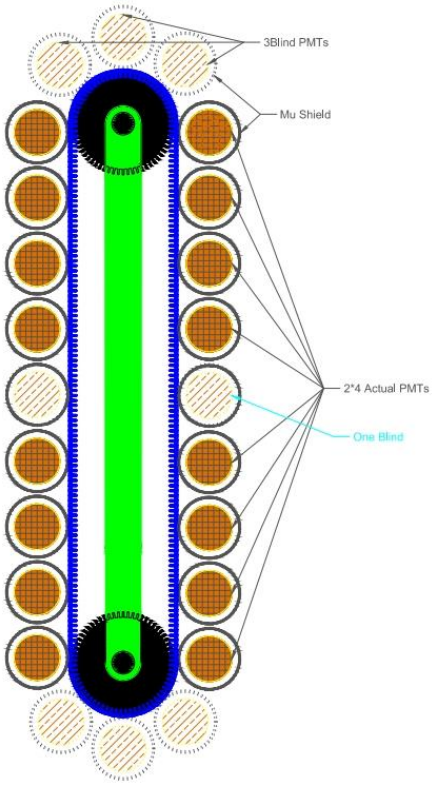

Figure 4.15: Conveyor Belt

As shown the photomultipliers will be in groups of four with just an empty mu shield on each side in the middle of the belt. The empty spaces on the turns are exactly equal to three shield widths. This makes sure that the spacing is correct and that there can be no shifting from the motion of the conveyor belt.

To rotate the conveyor belt, a large motor is used that uses a controller to direct it with the correct speed, direction, and duration of movement. The controller is controlled via USB connected to a personal computer using a communication terminal. Commands can be sent through the terminal to control the conveyor belt. Furthermore, these commands can be combined and saved into routines that can be called. I wrote and tested the routines so that the

conveyor belt can be easily and accurately rotated. The routines do not allow more than 180 degrees turns, to avoid cable entanglements.

4.6 Mirror Mount Simulation

Inside each elbow along our piping path there is a 45 degree elliptical mirror that can be adjusted with two screws on the back of an attached square mirror mount. The question then becomes what is the transformation from turning the screws a certain amount to the directionality of the mirror? Therefore, it is necessary to simulate the mirror mount to be able to calculate how much we have to rotate each of the two screws to get the desired mirror angles that we want.

Figure 4.16: Mirror Mount

First we make the reference frame where the tension spring holding the two pieces together is in the bottom left corner at coordinate $P_1 = (0,0,0)$. The first screw is in the bottom right corner at $P_2 = (L, 0,0)$ where L is the length of a side of the square mount. The other screw is in the top left corner at $P_4 = (0, L, 0)$ and the free top right corner is at $P_3 = (L, L, 0)$.

The screws have and a radius of 0.188 inches and a pitch of 64 threads per inch, which means that for every full rotation there will be an increase in length of $\Delta L = 0.0396875\ cm$ for

that screw. If we turn the first screw by an angle θ_1 then we are essentially performing a rotation about the y-axis of angle φ_1 that changes the coordinates of the points by the transformation

$$\begin{bmatrix} P_x' \\ P_y' \\ P_z' \end{bmatrix}_{1/4} = \begin{bmatrix} 1 & 0 & 0 \\ 0 & 1 & 0 \\ 0 & 0 & 1 \end{bmatrix} \begin{bmatrix} P_x \\ P_y \\ P_z \end{bmatrix}_{1/4} \text{ and } \begin{bmatrix} P_x' \\ P_y' \\ P_z' \end{bmatrix}_{2/3} = \begin{bmatrix} \cos(\varphi_1) & 0 & -\sin(\varphi_1) \\ 0 & 1 & 0 \\ \sin(\varphi_1) & 0 & \cos(\varphi_1) \end{bmatrix} \begin{bmatrix} P_x \\ P_y \\ P_z \end{bmatrix}_{2/3}. \quad (4.10)$$

where $\varphi_1 = \sin^{-1}(\frac{z_1}{L})$. The increase in height z_1 is $\Delta L \frac{\theta_1}{2\pi}$.

Likewise, if we turn the second screw by an angle θ_2 then we are essentially performing a rotation about the x-axis of angle φ_2 that changes the coordinates of the points by the transformation

$$\begin{bmatrix} P_x' \\ P_y' \\ P_z' \end{bmatrix}_{1/2} = \begin{bmatrix} 1 & 0 & 0 \\ 0 & 1 & 0 \\ 0 & 0 & 1 \end{bmatrix} \begin{bmatrix} P_x \\ P_y \\ P_z \end{bmatrix}_{1/2} \text{ and } \begin{bmatrix} P_x' \\ P_y' \\ P_z' \end{bmatrix}_{4/3} = \begin{bmatrix} 1 & 0 & 1 \\ 0 & \cos(\varphi_2) & -\sin(\varphi_2) \\ 0 & \sin(\varphi_2) & \cos(\varphi_2) \end{bmatrix} \begin{bmatrix} P_x \\ P_y \\ P_z \end{bmatrix}_{4/3}. \quad (4.11)$$

where $\varphi_2 = \sin^{-1}(\frac{z_2}{L})$. The increase in height z_2 is $\Delta L \frac{\theta_2}{2\pi}$.

However, when both screws are turned things become much more complicated but only for the free corner since it will experience both rotations. The best way to handle this is to first perform the rotation transformation for the shorter screw length increase using either Equation 4.10 if the first screw is shorter or Equation 4.11 if the second screw is shorter. We are now in the P' reference frame which once again is flat. So we can apply the long screw's transformation in this new frame. If the first screw is the shorter screw, then the free corner's coordinates become

$$\begin{bmatrix} P_x'' \\ P_y'' \\ P_z'' \end{bmatrix}_3 = \begin{bmatrix} 1 & 0 & 1 \\ 0 & \cos(\varphi_2) & -\sin(\varphi_2) \\ 0 & \sin(\varphi_2) & \cos(\varphi_2) \end{bmatrix} \begin{bmatrix} \cos(\varphi_1) & 0 & -\sin(\varphi_1) \\ 0 & 1 & 0 \\ \sin(\varphi_1) & 0 & \cos(\varphi_1) \end{bmatrix} \begin{bmatrix} P_x \\ P_y \\ P_z \end{bmatrix}_3. \quad (4.12)$$

If the second screw is the shorter screw, then the free corner's coordinates become

$$\begin{bmatrix} P_x'' \\ P_y'' \\ P_z'' \end{bmatrix}_3 = \begin{bmatrix} \cos(\varphi_1) & 0 & -\sin(\varphi_1) \\ 0 & 1 & 0 \\ \sin(\varphi_1) & 0 & \cos(\varphi_1) \end{bmatrix} \begin{bmatrix} 1 & 0 & 1 \\ 0 & \cos(\varphi_2) & -\sin(\varphi_2) \\ 0 & \sin(\varphi_2) & \cos(\varphi_2) \end{bmatrix} \begin{bmatrix} P_x \\ P_y \\ P_z \end{bmatrix}_3 . \quad (4.13)$$

Therefore, we know now that the free corner is rotated an angle

$$\psi = \cos^{-1}\left(\frac{\cos(\varphi_2)\cos(\varphi_1) + \cos(\varphi_2) + \cos(\varphi_1) - 1}{2}\right) \quad (4.14)$$

in the direction of the unit vector

$$\left(\sqrt{\frac{[\cos(\varphi_1)+1][\cos(\varphi_2)-1]}{[\cos(\varphi_1)+1]\cos(\varphi_2)+\cos(\varphi_1)-3}}, \sqrt{\frac{[\cos(\varphi_1)-1][\cos(\varphi_2)+1]}{[\cos(\varphi_1)+1]\cos(\varphi_2)+\cos(\varphi_1)-3}}, \sqrt{\frac{[\cos(\varphi_1)-1][\cos(\varphi_2)-1]}{[\cos(\varphi_1)+1]\cos(\varphi_2)+\cos(\varphi_1)-3}}\right). \quad (4.15)$$

Since we know where we want our light to go at each interaction vertex along the optical path, we can work backwards to find how much each screw for each mirror mount should be rotated to achieve the desired path.

4.7 Optics Testing

With so many optical elements, the efficiency of each has to be measured to the 0.1% level. The overall efficiency of the device is equal to the product of the efficiencies of each element that comes in contact with light. The efficiencies depend on wavelength.

We need to test many elliptical mirrors of all sizes, several gratings, and several Wollaston prisms. To do this effectively we will need robust experimental setups. In each of these setups we had access to three different wavelength laser diodes; a violet laser at 405 nm, a green laser at 532 nm, and a red laser at 635 nm. This will expose any spectral differences amongst the optical elements.

We first wanted to test how unpolarized light interacts with the mirrors and gratings and compare that to the numbers given by the manufactuers. To do this we made an experimental setup as shown in Figure 4.17.

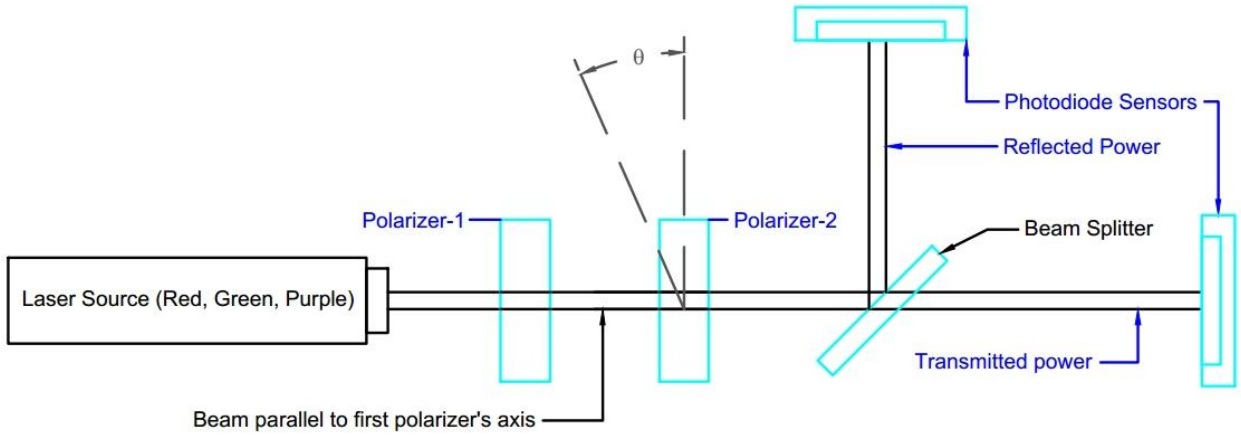

Figure 4.17: Experimental Setup to Test Optical Elements with Unpolarized Light

One of our laser diodes emits a beam that goes through the first polarizer. This is transmitted through to the second polarizer which will be rotated. After the second polarizer, the light then travels to the beam splitter at a 45 degree angle. This transmits the ordinary beam to the first photodiode power sensor and the extraordinary beam reflects orthogonally from the original beam to the second photodiode. The second polarizer is rotated until the power output at each sensor is the same. Doing this will allow us to have two identical copies of the same wavelength beam. This way in case the beam power fluctuates between different measurements fluctuations will cancel out in the ratios. This is because we have the clone beam that is constantly monitoring the power output therefore we can always just normalize to that beam and our measurements will all be accurate across all trials.

Now that we have two identical beams of the same color to test with, we can now begin testing certain optical elements. Both the different sized ellipitical mirrors and the diffraction gratings were placed on a rotating stage. This way we can test all elements at different angles of incidence. This stage will be placed where the second photodiode sensor was in the original setup and the photodiode sensor will now be placed in the path of reflected beam if using a mirror or the diffracted beam if using a diffracted grating. For both mirrors and gratings, they were rotated in 5 degree intervals from 5 to 85.

Since the optical components in the optics box will be seeing totally polarized light from the Wollaston prism then we should definitely also test the optical elements using the Wollaston prism's output. We used the same setup as before except this time we replaced the beam splitter with the Wollaston prism and the photodiode sensors will be positioned to intercept each of the two transmitted polarized beams as shown in Figure 4.18. The parallel polarization is the upper beam and the perpendicular polarization is the lower beam. The second polarizer was rotated until both polarizations had equal power outputs.

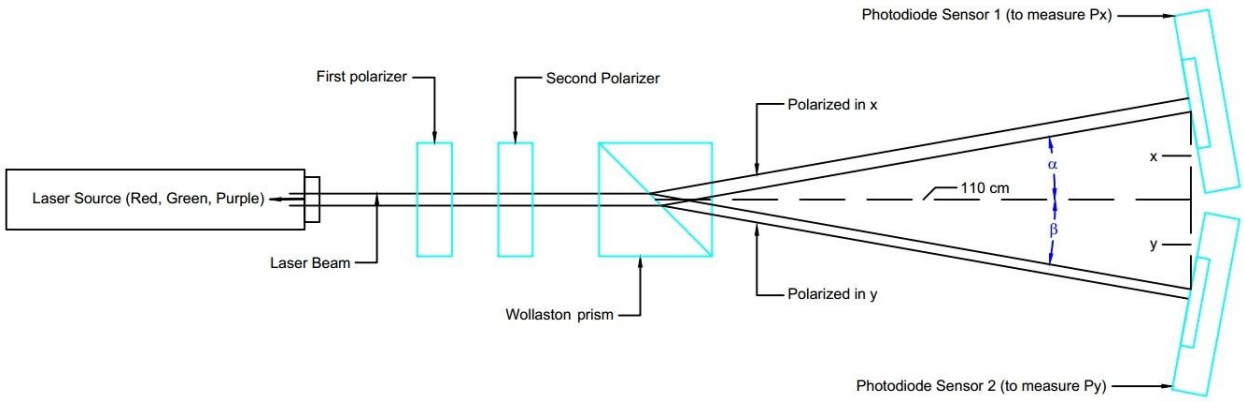

Figure 4.18: Experimental Setup to Test Optical Elements with Polarized Light

First we had to determine the efficiency of the Wollaston prism and the angular spread of the transmitted light. Both of these quantities are dependent on the wavelength. To find the efficiency of the Wollaston prism we first moved one of the photodiode sensors to the front of the Wollaston prism. This was to measure the incoming beam's power. We then put that photodiode back to where it belongs and then took measurements of the parallel and perpendicular power outputs. To compare intial with final we have to add the two final powers. The difference is the power lost due to the Wollaston prism therefore the ratio of final over intial will give the efficiency.

As for finding the angles we simply measured the horizontal distance to our photodiode sensors and then measured the distance from the midline for each of the beams. To find the angle you can simply take an arctangent. It should be noted that the angles were different for each beam even using the same wavelength.

Now that we know the efficincies and angular beam deviations we can now test the efficiencies of the mirrors and gratings but this time using polarized light. As before we will put one of the elliptical mirrors or diffraction gratings on a rotating stage with micrometer and will have one of the beams hit it. We will once again be varying the angle of incidence by rotating the stage in 5 degree increments from 5 to 85 degrees. Even though the other beam has a different polarization as the beam being tested, we can still monitor it for any change in power thus also allowing us to normalize our data between trials for consistency.

4.8 Mirror/Grating Angles Simulation

Now that we have all of the efficiencies figured out we still have the task of having the light leaving the ruled grating hit the correct spots based on certain wavelengths. It may seem trivial for the light to hit the first mirror in the optics box, but the solution set shrinks enormously by the time the light reaches the PMTs. Therefore, it is essential to simulate all of the light interactions with the optical components so that we will have a crystal clear idea of the final wavelength spread and where wavelengths are hitting the array of PMTs.

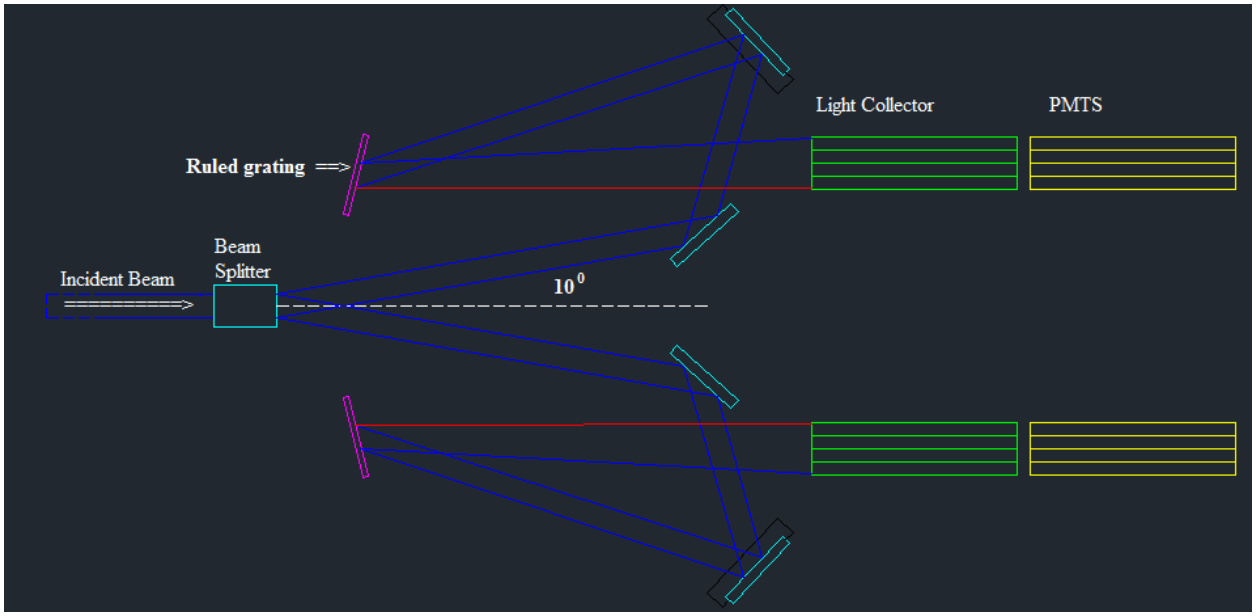

Figure 4.19: Light Paths for Both Polarizations

There are nine different parameters that must be independently changed until the solution set upper and lower bounds for each parameter is found. Both optics box mirror and the ruled gratings are on small posts. These posts can be moved closer and farther to the screw that attaches them to the optical plate. For each optical path, there are two mirrors and a ruled grating therefore there are three such posts that can be adjusted. Also, the posts can be rotated about the

attaching screw by a U-shaped attachment thus we have another three degrees of freedom. The mirrors and gratings themselves can be rotated which adds another three parameters to each optical path. As you can see for each of the four optical paths there are nine independent parameters which leads to a massively large solution set.

Each post has a range of two centimeters, each post can be rotated 2π radians, and each mirror can be rotated 2π radians yet only π radians actually matter since the backside of the mirror doesn't reflect anything. Assuming each post can be moved in increments of 5 mm and the rotations of the posts and mirrors in increments of 1 degree this leads to a solution set of size $\left(\frac{2\ cm}{0.5\ cm}\right)^3\left(\frac{360\ deg}{1\ deg}\right)^3\left(\frac{180\ deg}{1\ deg}\right)^3 = 4^3 360^3 180^3 = 259200^3 = 1.741 * 10^{16}$. This definitely cannot be done by hand in a reasonable amount of time therefore it is necessary to create a simulation and search for the correct solutions out of the full solution set. This will be done by using the following constraints. The light from the Wollaston prism first has to hit the first mirror, then has to hit the second mirror, then has to hit the grating, and finally the middle of the 350 nm light square has to hit the edge of the outer PMT and the middle of the 650 nm light square has to hit the edge of the inner PMT of the PMT array. Each successive constraint limits the solution set by many more orders of magnitude until the upper and lower limits of each parameter can be narrowed down.

The first thing we need to do is first figure out all of the angles before and after for all of the interactions. In Figure 4.20 I have made a very detailed analysis of all angles involved from the Wollaston prism, between the mirrors, and for the grating.

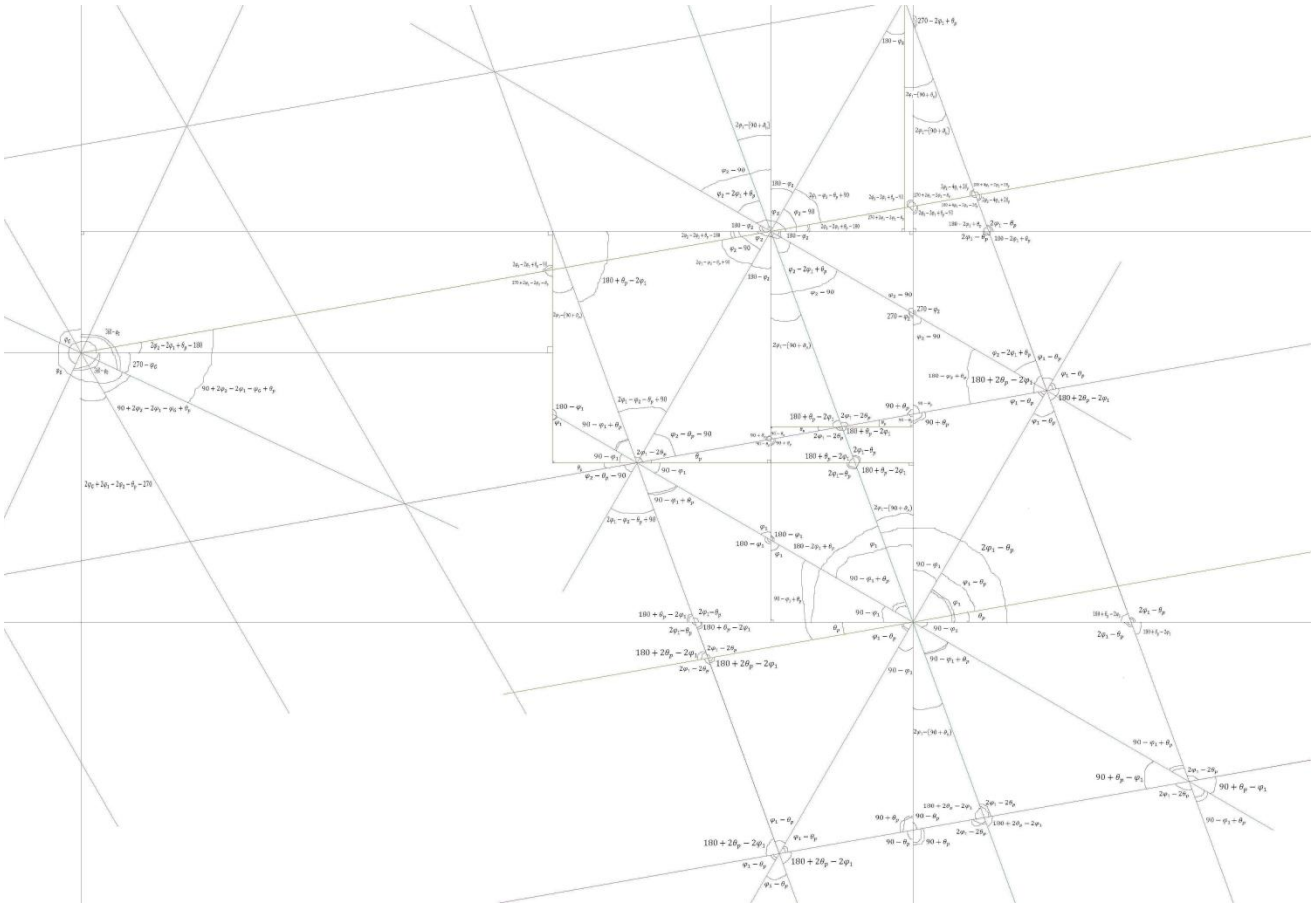

Figure 4.20: Incoming and Outgoing Angles for Mirrors and Grating

We begin by exiting the Wollaston prism at an angle θ_p from the horizontal. This light represented by the yellow line then travels across the optics box and hits the first mirror at an angle of incidence

$$\theta_{1i} = \frac{\pi}{2} - \varphi_1 + \theta_p \tag{4.16}$$

where φ_1 is the angle of the first mirror starting from 0 degrees at the horizontal.

Using the Law of Reflection one can easily find the reflecting angle

$$\theta_{1r} = 2\varphi_1 - \theta_p. \tag{4.17}$$

The light then travels to the second mirror and hits it with an angle of incidence shown

$$\theta_{2i} = \frac{\pi}{2} + 2\varphi_1 - \varphi_2 - \theta_p \tag{4.18}$$

where φ_2 is the angle of the second mirror starting from 0 degrees at the horizontal.

Once again the light reflects off of the second mirror, this time at an angle

$$\theta_{2r} = 2\varphi_2 - 2\varphi_1 + \theta_p. \tag{4.19}$$

Now the light heads to the ruled grating and hits it with an angle of incidence

$$\theta_{gi} = \frac{\pi}{2} + 2\varphi_2 - 2\varphi_1 - \varphi_g + \theta_p. \tag{4.20}$$

where φ_g is the angle of the grating starting from 0 degrees at the horizontal.

A ruled grating works much differently than a mirror in that it has several orders of reflections instead of just one. The zeroth order peak is the same as if the grating were just a mirror and leaves at an angle

$$\theta_{gr_0} = \theta_{m=0} = 2\left(\varphi_g - \varphi_2 + \varphi_1\right) - \theta_p \tag{4.21}$$

However, we are not interested in the zeroth order peak. We are interested in the first order peak because rather than all wavelengths of light still being combined in a beam, the different wavelengths separate from each other creating a rainbow like with a prism as discussed in section 4.3.

Using the diffracted angle given Equation 4.5, we can find the angle the diffracted light leaves the grating in our reference frame of 0 being the horizontal as

$$\theta_f = \varphi_g - \frac{\pi}{2} + \theta_m. \tag{4.22}$$

This exit angle in our reference frame can then be used to find the vertical coordinate for the different wavelengths after the grating.

$$y = xtan(\theta_f) \tag{4.23}$$

where y is the vertical distance between where the light hits the PMT array and where it hits the grating and x is the horizontal distance from the PMT array to the point of contact of the light on the grating.

A compressed table of all possible solutions for the parallel polarization is shown in Table 4.1 and for the perpendicular polarization in Table 4.2. Due to the compression, the angles attached with minuses are the minimums and the angles attached with pluses are the maximums. The number of solutions for each range is in the last column.

φ_1	φ_{2-}	φ_{2+}	φ_{g-}	φ_{g+}	P_{1-}	P_{1+}	P_{2-}	P_{2+}	P_{g-}	P_{g+}	Sols
42	146	148	267	269	110	113	296	340	253	281	1250
43	146	149	261	269	109	119	287	352	244	285	19262
44	146	151	256	269	107	125	274	349	242	289	75721
45	147	153	253	269	106	131	272	344	241	291	187392
46	148	155	252	269	105	142	272	356	239	292	368370
47	149	157	250	269	104	160	270	352	238	293	592340
48	150	159	249	269	103	181	269	356	236	295	824073
49	151	161	249	269	102	275	267	46	235	295	1078764
50	152	162	249	269	101	278	265	49	234	297	1441564
51	153	163	249	269	99	280	262	55	233	298	1959406
52	154	164	248	269	95	283	259	59	231	299	2584986
53	155	165	248	269	92	287	254	64	229	301	3166483
54	155	165	248	269	92	287	254	64	229	301	3174262
55	156	166	248	269	88	294	246	72	229	302	3572811
56	158	168	248	269	81	297	238	89	226	304	3613632
57	159	169	248	269	103	301	233	99	225	306	3264353
58	160	170	248	269	117	304	231	109	223	307	2755102
59	161	171	248	269	135	308	226	124	222	308	2193883
60	162	172	248	269	144	312	215	137	221	309	1638528
61	163	173	248	269	154	315	209	163	219	310	1161691
62	164	174	248	269	160	310	233	259	217	311	810218
63	165	175	248	269	166	309	10	224	217	312	567752
64	167	176	248	269	180	302	34	196	219	310	371995
65	168	177	248	267	191	299	47	165	229	307	206838
66	169	178	248	266	206	296	57	151	229	304	87950
67	170	179	249	264	210	293	72	141	229	298	31253
68	171	180	249	263	225	283	85	130	233	294	6813
69	173	178	252	262	226	273	103	127	255	280	708

Table 4.1: Solutions for Parallel Polarization

For the parallel polarization side of the optics box there were a total of 35,757,400 which is an extremely small subset of the total solutions only accounting for a fraction of $2.053 * 10^{-9}$ of the total possible.

φ_1	φ_{2-}	φ_{2+}	φ_{g-}	φ_{g+}	P_{1-}	P_{1+}	P_{2-}	P_{2+}	P_{g-}	P_{g+}	Sols
43	144	149	266	269	104	109	283	348	230	301	9574
44	145	151	261	269	103	115	260	359	225	304	77339
45	146	153	256	269	101	121	244	359	222	306	274354
46	147	155	253	269	99	127	224	78	221	309	652068
47	148	156	251	269	96	133	214	88	218	311	1215987
48	149	158	250	269	93	143	191	113	214	314	1932550
49	150	159	249	269	89	161	0	359	213	316	2718027
50	151	161	248	269	86	295	0	359	209	319	3407805
51	152	162	248	269	82	298	0	359	208	320	4090480
52	153	163	247	269	79	302	0	359	208	320	4893067
53	154	164	247	269	75	306	0	359	208	321	5763034
54	155	165	247	269	71	310	0	359	207	322	6679403
55	156	166	247	269	67	314	0	359	207	323	7392169
56	157	167	247	269	63	318	0	359	207	324	7751630
57	158	168	247	269	58	322	0	359	206	325	7754612
58	159	169	247	269	54	327	0	359	204	326	7489002
59	160	170	248	269	48	332	0	359	201	327	7026706
60	161	171	248	269	43	338	0	359	201	327	6339149
61	162	172	248	269	87	345	0	359	199	328	5463187
62	163	173	248	269	117	355	0	359	198	329	4442838
63	164	174	248	269	140	346	6	272	197	330	3466309
64	165	175	248	269	158	329	4	231	197	331	2623179
65	166	176	248	269	168	319	32	204	197	329	1856367
66	167	177	249	269	185	312	44	180	198	327	1194563
67	168	178	249	269	202	307	56	167	207	323	672314
68	169	178	250	269	202	307	56	161	209	320	424575
69	170	179	251	269	231	294	82	153	213	313	132930
70	171	180	254	269	240	280	99	148	219	306	26832

Table 4.2: Solutions for Perpendicular Polarization

For the perpendicular polarization side of the optics box there were a total of 95,770,050 which is larger than for the perpendicular side however it still only accounts for $5.500 * 10^{-9}$ of the total possible.

Figure 4.21 shows one of the solutions for the upper half and one of the solutions for the lower half of the many possible solutions for each.

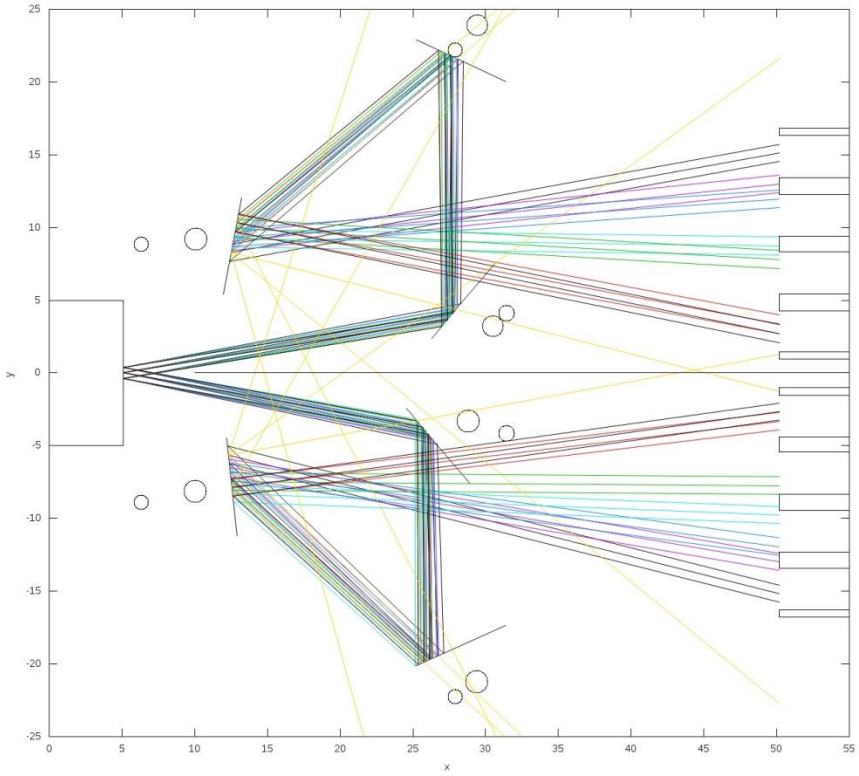

Figure 4.21: A Solution of the 9 Parameters for Both Polarizations

4.9 Prism-Lens Testing

Since different wavelengths of light are coming towards the light collectors at different angles there needs to be a much more efficient means of gathering the light to its corresponding PMT than the light collectors we originally produced. The solution was to use different angled prisms and glue those to lenses so that within a range of angles all of the wavelengths of light would end up being close to parallel and enter the PMT almost perpendicularly. A schematic of this is shown in Figure 4.22.

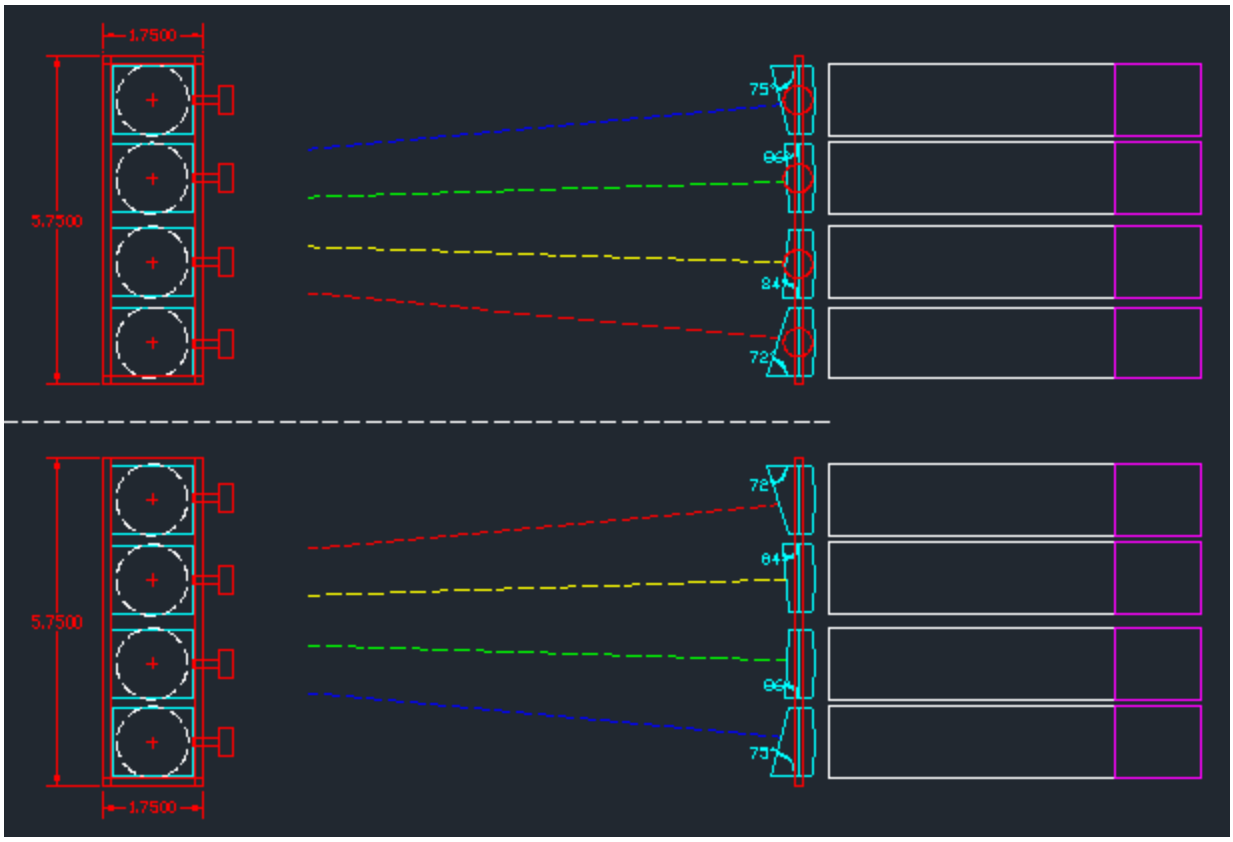

Figure 4.22: Prism-lens Arrangement and Mount

The index of refraction of air is 1, for the mirror and lens it is 1.55 and for the glue it is 1.56. Light from the grating enters the angled face of the prism at an angle depending on the wavelength of the light.

The prisms can either have their longest base on the bottom or the top. For simplification purposes we will only work out the math for the case of the longest base being on the bottom. Performing a flip so that the longest base is now on the top doesn't change any of the important math or physics.

There are three possible scenarios that we need to find the math for. The first scenario involves incoming diffracted light coming toward the prism at a positive angle and below the

normal vector of the prism's surface. The second scenario is when the incoming light now has a negative angle, however in this case it still remains below the prism surface's normal vector. The third scenario has a negative angle for the approaching light and this time it comes above the normal vector of the prism's surface.

With or without the prism-lenses we already know from the mirror/angles program all of the angles of the incoming diffracted light with the photomultiplier tubes at 0 and the Wollaston prism at π. We already know if a diffracted wavelength is going to have a positive or negative angle, but we don't know yet which wavelengths will be above or below the prism's normal vector. The normal vector direction for when the longest base is on the bottom is

$$\theta_{\hat{\boldsymbol{n}}} = \frac{\pi}{2} + \theta_p \; for \; longest \; prism \; base \; on \; bottom \tag{4.24}$$

and when the longest base is on the top (flipped) the normal vector direction is

$$\theta_{\hat{\boldsymbol{n}}} = \pi - \theta_p \; for \; longest \; prism \; base \; on \; top \; (flipped) \tag{4.25}$$

where θ_p is the angle of the prism.

Therefore, the incoming light will come above the normal if its angle is within

$$Above: \pi + \theta_p < \theta_f < \frac{3\pi}{2} + \theta_p \; for \; longest \; prism \; base \; on \; bottom \tag{4.26}$$

for the non-flipped case and if its angle is within

$$Above: 2\pi - \theta_p < \theta_f < \frac{\pi}{2} - \theta_p \; for \; longest \; prism \; base \; on \; top \; (flipped) \tag{4.27}$$

for the flipped case where θ_f is angle of the light in our chosen reference frame's horizontal.

The incoming light will come below the normal if its angle is within the range

$$Below: \frac{3\pi}{2} + \theta_p < \theta_f < \theta_p \; for \; longest \; prism \; base \; on \; bottom \tag{4.28}$$

for the non-flipped case and within the range

$$Below: \frac{\pi}{2} - \theta_p < \theta_f < \pi - \theta_p \; for \; longest \; prism \; base \; on \; top \; (flipped) \tag{4.29}$$

for the flipped case.

Obviously any angles of the incoming diffracted light between θ_p and $\pi + \theta_p$ will be neither above or below because they will miss the prism entirely. Knowing whether or not wavelengths are above or below the normal and which are positive allows us now to be able to know which of the three scenarios applies.

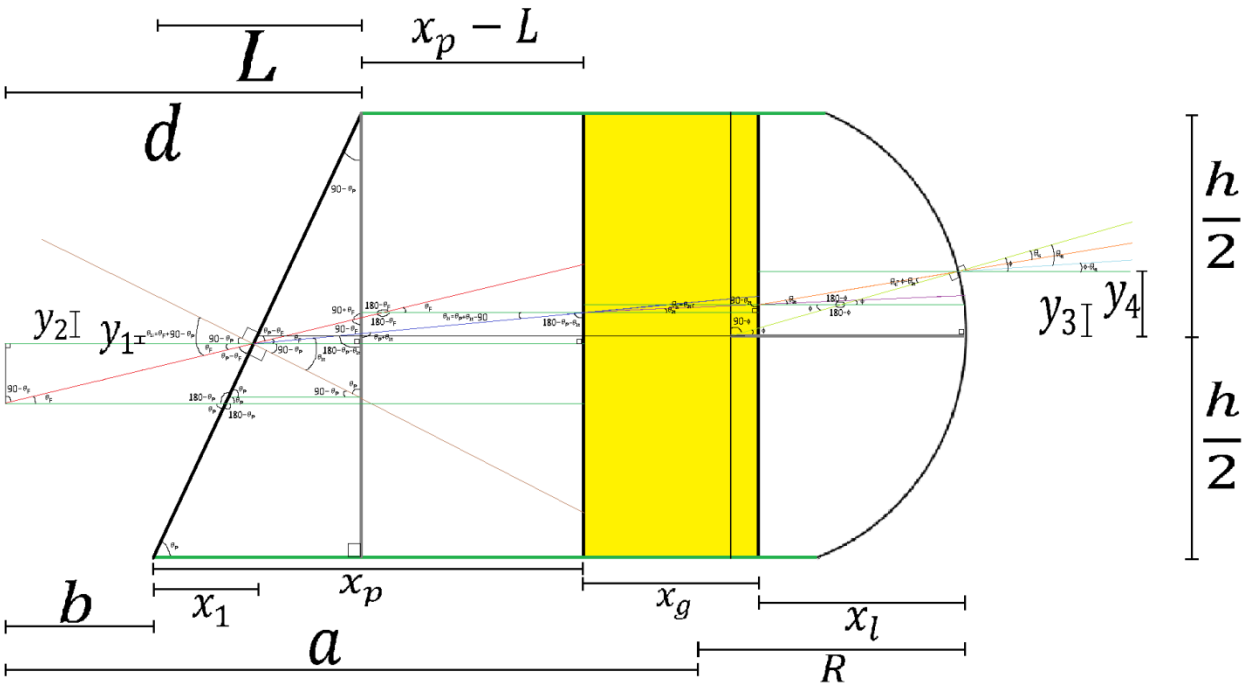

Figure 4.23: Light that is Positive and Below the Normal

Shown above in Figure 4.23 is the case of a positive angled beam below the prism's normal vector. Since the index of the prism is higher than that of air it will slow and will bend towards the horizontal according to Snell's Law

$$n_i \sin(\theta_i) = n_t \sin(\theta_t) \tag{4.30}$$

where n_i is the index of refraction of the incident medium, θ_i is the angle of incidence, n_t is the index of refraction of the transmitted medium, and θ_t is the angle of transmission. Our first angle of incidence is

$$\theta_{1i} = \left|\theta_f + \left(\frac{\pi}{2} - \theta_p\right)\right| \tag{4.31}$$

where θ_{1i} is the angle of incidence on the prism's angled surface, θ_f is the incoming light's angle in our reference frame and θ_p is the angle of the prism.

Using Equation 4.24, we can solve for the angle of transmission θ_{1t}.

$$\theta_{1t} = \sin^{-1}\left(\frac{n_{air}}{n_{prism}}\sin(\theta_{1i})\right) = \sin^{-1}\left(\frac{1}{1.55}\sin(\theta_{1i})\right) \tag{4.32}$$

The incoming diffracted light from the grating hits the prism at x-coordinate x_1 where 0 is at the front wall and at y-coordinate y_1 where 0 is the midline of the box. To find this one can solve the equations of the two lines: the incoming light ray and the slope of the prism

$$y_1 = y_{grating} + \tan(\theta_f)\,(x_1 - x_{grating})\ and\ y_1 = p_{top} + \tan(\theta_p)\,(x_1 - d) \tag{4.33}$$

where $y_{grating}$ is the y-coordinate of where the light diffracts off of the grating, $x_{grating}$ is the x-coordinate of where the light diffracts off of the grating, p_{top} is the y-coordinate of the top of the prism, and d is the horizontal distance from the front plate of the optics box to the end of the

sloped portion of the prism. Solving this equation yields the point in our reference frame where the light hits the prism

$$(x_1, y_1) = \left(\frac{(p_{top} - y_{grating}) - (d\tan(\theta_p) - x_{grating}\tan(\theta_f))}{\tan(\theta_f) - \tan(\theta_p)}, y_{grating} + \tan(\theta_f)(x_1 - x_{grating}) \right) \tag{4.34}$$

Furthermore, in our reference frame the light makes an angle while in the prism of

$$\theta_{1f} = \theta_p - \frac{\pi}{2} + \theta_{1t} \tag{4.35}$$

The light then reaches the prism-glue barrier at an angle of incidence

$$\theta_{2i} = |\theta_{1f}| \tag{4.36}$$

since the normal is horizontal and at a point in our reference frame of

$$(x_2, y_2) = \big(d + (x_p - L), y_1 + \big(d + (x_p - L) - x_1\big)\tan(\theta_{1f})\big) \tag{4.37}$$

where $x_p - L$ is the length of the rectangular section of the prism.

The absolute value is needed for θ_{2i} since the angle would become negative for $\theta_f < 0$ from the grating which will be discussed shortly. Therefore the absolute value takes care of the invalid negative angle and is the correct global solution.

Once again the light slows down and bends towards the horizontal according to Snell's Law due to the higher index of refraction of the glue with a transmitted angle

$$\theta_{2t} = \sin^{-1}\left(\frac{1.55}{1.56}\sin(\theta_{2i})\right) \tag{4.38}$$

The light quickly passes through the thin glue layer of thickness x_g and becomes incident on the surface of the lens with angle of incidence

$$\theta_{3i} = \theta_{2t} \tag{4.39}$$

and at a point in our reference frame of

$$(x_3, y_3) = \left(d + \left(x_p - L\right) + x_g, y_2 + x_g \tan\left(\theta_{2f}\right)\right) \tag{4.40}$$

where x_g is the thickness of the glue, which is very thin.

Also, the light within the glue in our reference frame will be at an angle of

$$\theta_{2f} = \theta_{2t}\ for\ \theta_{1f} \geq 0\ and\ \theta_{2f} = -\theta_{2t}\ for\ \theta_{1f} < 0 \tag{4.41}$$

After leaving the glue medium and entering the lower index of refraction medium of the lens the light has the transmission angle

$$\theta_{3t} = \sin^{-1}\left(\frac{1.56}{1.55}\sin(\theta_{3i})\right). \tag{4.42}$$

In our reference frame, the light makes in angle within the lens of

$$\theta_{3f} = \theta_{3t}\ for\ \theta_{2f} \geq 0\ and\ \theta_{3f} = -\theta_{3t}\ for\ \theta_{2f} < 0. \tag{4.43}$$

The light finally reaches the last interface which is spherically shaped with angle of incidence

$$\theta_{4i} = |\varphi - \theta_{3t}| \tag{4.44}$$

The angle φ is the angle from the center of the radius of curvature to the exit point. We take the absolute value since the radius of curvature, R, can make $\theta_{3t} > \varphi$ which would make θ_{4i} negative which isn't valid. This happens when the $R > y_3$ which leads to swapping the terms in the equation to $\theta_{3t} - \varphi$. Therefore an absolute value satisfies a general solution. The value of φ can be found solving a system of equations using the equation of the line from where the light from the glue strikes the lens at (x_3, y_3) to where the light leaves the lens into the air at (x_4, y_4)

$$y_4 = y_3 + (x_4 - x_3)\tan(\theta_{3f}) \tag{4.45}$$

and the equations for the x and y-coordinate of the circle that describes the curve of the lens

$$x_4 = x_{max} + R(\cos(\varphi) - 1) \; and \;\; y_4 = (p_{bot} + h) + R\sin(\varphi) \tag{4.46}$$

where $x_{max} = d + (x_p - L) + x_g + x_l$ is the distance from the front plate to the farthest point of the lens of thickness x_l, R is the radius of curvature, p_{bot} is the y-coordinate of the bottom of the lens, and h is half of the height of the lens.

Solving these equations yields

$$\sin(\varphi) - \tan(\theta_{3f})\cos(\varphi) = \frac{(y_3 - (p_{bot} + h)) - (x_3 - (x_{max} - R))\tan(\theta_{3f})}{R} \tag{4.47}$$

and using the relation

$$A\sin(x) - Bcos(x) = \sqrt{A^2 + B^2}\sin\left(x - \tan^{-1}\left(\frac{B}{A}\right)\right) \tag{4.48}$$

we obtain the value of φ

$$\varphi = \sin^{-1}\left(\frac{(y_3 - (p_{bot} + h))\cos(\theta_{3f}) + (x_3 - (x_{max} - R))\sin(\theta_{3f})}{R}\right) + \theta_{3f} \tag{4.49}$$

Now that we know the angle φ, we can insert it into Equation 4.39 to find the point of interaction between the lens and air.

After passing through the lens the light exits into the air with a transmitted angle

$$\theta_{4t} = \sin^{-1}\left(\frac{1.55}{1}\sin(\theta_{4i})\right) \tag{4.50}$$

The exit angle in our reference frame is then

$$\theta_{4f} = \varphi - \theta_{4t} \; when \; \varphi \geq \theta_{3f} \; and \; \theta_{4f} = \varphi + \theta_{4t} \; for \; \varphi < \theta_{3f} \; .$$

The light travels a short distance to the coated glass surface of the PMT to be collected at the point in our reference frame of

$$(x_{final}, y_{final}) = (x_{PMT}, y_4 + (x_{PMT} - x_4)\tan(\theta_{4f})) \tag{4.51}$$

where x_{PMT} is the distance from the front plate to the glass of the PMTs.

When the diffracted angle is negative and below the normal of the prism some of the previous equations change. This scenario is shown below in Figure 4.24.

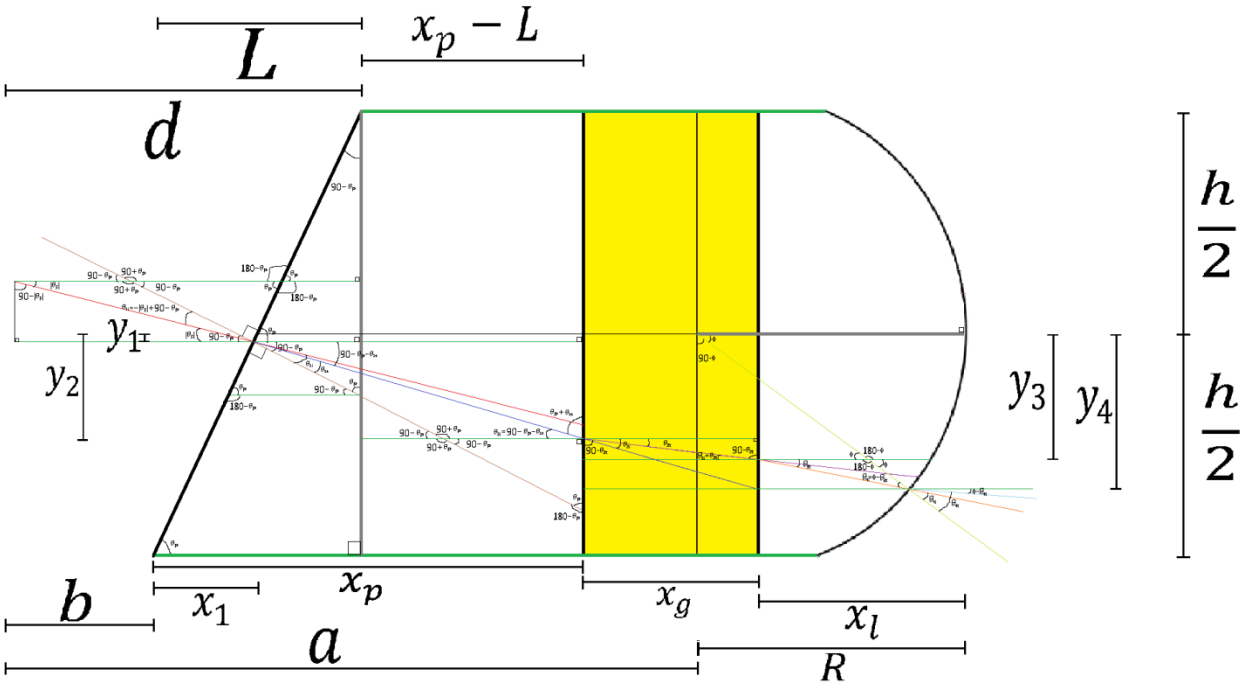

Figure 4.24: Light that is Negative and Below the Normal

All of the transmitted angle equations remain the same since they simply use Snell's Law and will use the modified incident angles. Also, all of the reference frame angles will remain the same since the conditions for negative angles are already taken into account. The first angle of incidence is

$$\theta_{1i} = \left|\theta_f + \left(\frac{\pi}{2} - \theta_p\right)\right| \tag{4.52}$$

which is the same as in the previous scenario. Remember our angle θ_f is now negative. The angle of incidence at the prism-glue interface is also the same as Equation 4.30.

Everything else from the scenario before will be the same except the slopes will be negative due to the negative reference frame angles.

Lastly, we have the scenario of the incoming diffracted light having a negative angle and also this time the light is above the prism's normal vector. We have to make a few slight changes to just only a few of the formulas. Figure 4.25 shows what this case would look like.

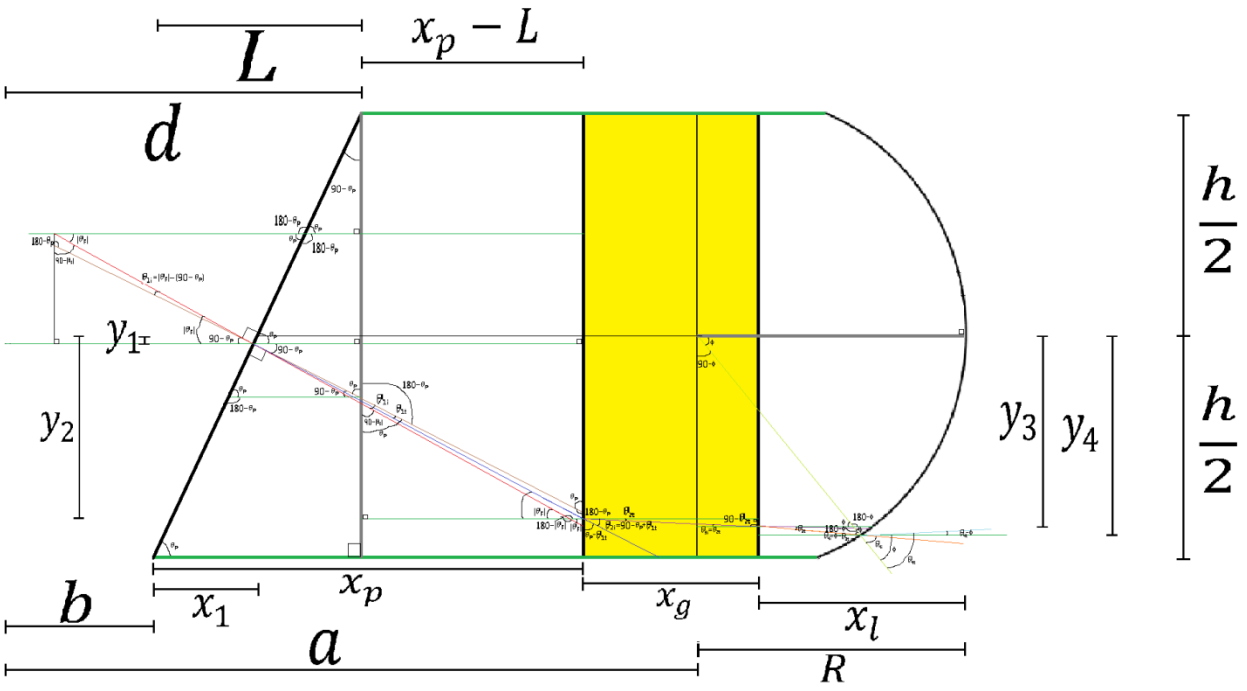

Figure 4.25: Light that is Negative and Above the Normal

The only equation that changes is for the reference angle of the light while inside the prism

$$\theta_{1f} = \theta_p - \frac{\pi}{2} - \theta_{1t}. \tag{4.53}$$

The only thing that has been altered was a sign change of the θ_{1t} term since we are now on the other side of the sloped face of the prism's normal.

It may have occurred to you that all of these cases were just for the non-flipped scenarios and that the flipped scenarios seem to have been omitted. The explanation is that the flipped cases are simply a vertical reflection of the non-flipped cases therefore almost all of the math is the same.

The positive angle, below the normal scenario becomes a negative angle, above the normal scenario yet one of the only things that are altered is a sign change of the θ_f term in Equation 4.25. Also, we just take the negative of Equation 4.29 to get the reference angle of the light while inside the prism. Everything else is the same though.

The negative angle, below the normal scenario becomes a positive angle, above the normal scenario. This will use the same small transformations as above for Equations 4.25 and 4.29.

The negative angle, above the normal scenario becomes the positive angle, below the normal scenario. Since we have performed a flip and a cross of the normal then the transformations for those two equations are slightly more complicated. The angle of incidence at the air-prism interface is

$$\theta_{1i} = \left|\frac{\pi}{2} - \theta_p - \theta_f\right| \tag{4.54}$$

and the reference angle of the light within the prism is

$$\theta_{1f} = \frac{\pi}{2} - \theta_p + \theta_{1t}. \tag{4.55}$$

Now that we know all of the angles and coordinates of interaction we now have to choose the best arrangement of prism-lenses that will give the most collimated transmitted light since that will be directly heading to our photomultipliers.

4.10 Prism-Lens Transmission Efficiencies

We now need to know the efficiencies of our new optical elements which we can find using the Fresnel equations [12].

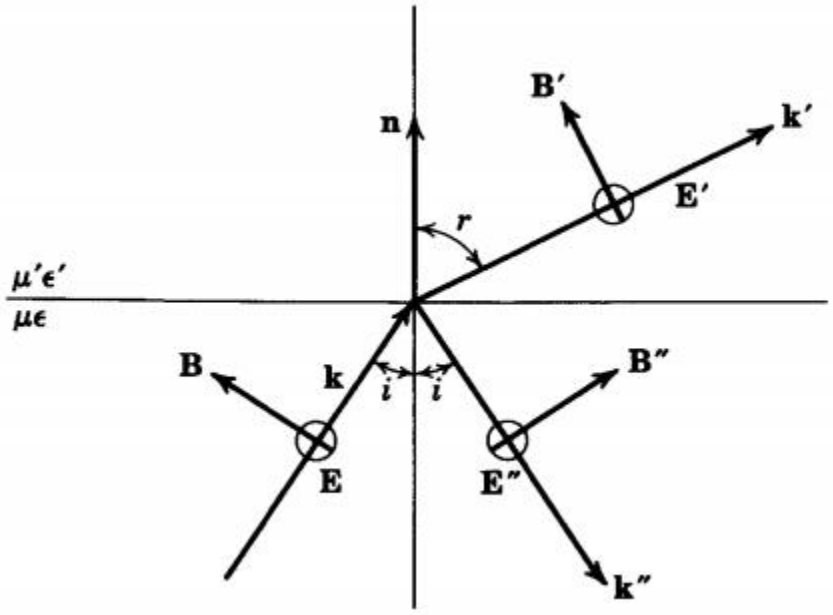

Figure 4.26: Electric Field Perpendicular to the Plane of Incidence

The ratio of the transmitted amplitude over the incident amplitude for E perpendicular to the plane of incidence is

$$t_\perp = \frac{E_0^{'}}{E_0} = \frac{2ncos(\theta_i)}{ncos(\theta_i) + \frac{\mu}{\mu'}\sqrt{n'^2 - n^2\sin^2(\theta_i)}} \approx \frac{2ncos(\theta_i)}{ncos(\theta_i) + \sqrt{n'^2 - n^2\sin^2(\theta_i)}} \tag{4.56}$$

where n is the index of refraction and μ is the magnetic permeability of the material we are leaving, n' is the index of refraction and μ' is the magnetic permeability of the material we are entering, and θ_i is the angle of incidence. For our materials $\mu \approx \mu'$ which slightly simplifies our equations.

The ratio of the reflected amplitude over the incident amplitude for E perpendicular to the plane is

$$r_\perp = \frac{E_0^{''}}{E_0} = \frac{ncos(\theta_i) - \frac{\mu}{\mu'}\sqrt{n'^2 - n^2\sin^2(\theta_i)}}{ncos(\theta_i) + \frac{\mu}{\mu'}\sqrt{n'^2 - n^2\sin^2(\theta_i)}} \approx \frac{ncos(\theta_i) - \sqrt{n'^2 - n^2\sin^2(\theta_i)}}{ncos(\theta_i) + \sqrt{n'^2 - n^2\sin^2(\theta_i)}} \tag{4.57}$$

The transmission amplitude squared gives the transmission coefficient $T_\perp = |t_\perp|^2$ and the reflection amplitude squared gives the reflection coefficient $R_\perp = |r_\perp|^2$ where $T_\perp + R_\perp = 1$ since the incident light either transmitted or reflected so they should add up to one. Therefore our transmission coefficient for the perpendicular polarization is

$$T_\perp = |t_\perp|^2 = \left|\frac{2ncos(\theta_i)}{ncos(\theta_i) + \sqrt{n'^2 - n^2\sin^2(\theta_i)}}\right|^2 \tag{4.58}$$

and our reflection coefficient for the perpendicular polarization is

$$R_\perp = |r_\perp|^2 = \left|\frac{ncos(\theta_i) - \sqrt{n'^2 - n^2\sin^2(\theta_i)}}{ncos(\theta_i) + \sqrt{n'^2 - n^2\sin^2(\theta_i)}}\right|^2. \tag{4.59}$$

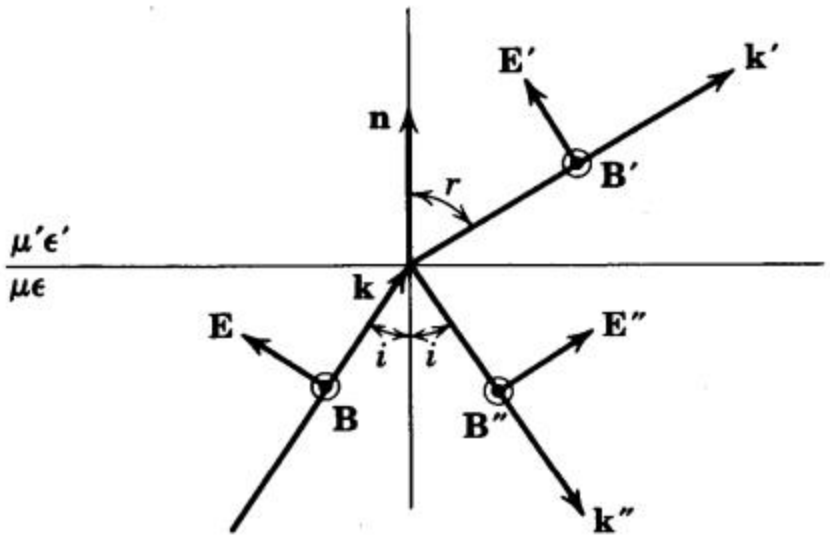

Figure 4.27: Electric Field Parallel to the Plane of Incidence

For E parallel to the plane of incidence, the ratio of the transmitted amplitude over the incident amplitude is

$$t_{\parallel} = \frac{E_0^{'}}{E_0} = \frac{2nn^{'}cos(\theta_i)}{\frac{\mu}{\mu^{'}}n^{'2}cos(\theta_i) + n\sqrt{n^{'2} - n^2\sin^2(\theta_i)}} \approx \frac{2nn^{'}cos(\theta_i)}{n^{'2}cos(\theta_i) + n\sqrt{n^{'2} - n^2\sin^2(\theta_i)}}. \tag{4.60}$$

The reflected amplitude over the incident amplitude ratio for E parallel to the plane of incidence is

$$r_{\parallel} = \frac{E_0^{''}}{E_0} = \frac{\frac{\mu}{\mu^{'}}n^{'2}cos(\theta_i) - n\sqrt{n^{'2} - n^2\sin^2(\theta_i)}}{\frac{\mu}{\mu^{'}}n^{'2}cos(\theta_i) + n\sqrt{n^{'2} - n^2\sin^2(\theta_i)}} \approx \frac{n^{'2}cos(\theta_i) - n\sqrt{n^{'2} - n^2\sin^2(\theta_i)}}{n^{'2}cos(\theta_i) + n\sqrt{n^{'2} - n^2\sin^2(\theta_i)}}. \tag{4.61}$$

Likewise for the parallel polarization $T_{\parallel} = \left|t_{\parallel}\right|^2$ and $R_{\parallel} = \left|r_{\parallel}\right|^2$ where $T_{\parallel} + R_{\parallel} = 1$. Therefore our transmission coefficient for the parallel polarization is

$$T_{\parallel} = \left|t_{\parallel}\right|^2 = \left|\frac{2nn^{'}cos(\theta_i)}{n^{'2}cos(\theta_i) + n\sqrt{n^{'2} - n^2\sin^2(\theta_i)}}\right|^2 \tag{4.62}$$

and our reflection coefficient for the perpendicular polarization is

$$R_{\parallel} = \left|r_{\parallel}\right|^2 = \left|\frac{n'^2 cos(\theta_i) - n\sqrt{n'^2 - n^2 \sin^2(\theta_i)}}{n'^2 cos(\theta_i) + n\sqrt{n'^2 - n^2 \sin^2(\theta_i)}}\right|^2. \tag{4.63}$$

The power transmitted is

$$T = \frac{n_t \cos(\theta_t)}{n_i \cos(\theta_i)}|t|^2 = \frac{\sqrt{n_t^2 - n_i^2 \sin^2(\theta_i)}}{n_i \cos(\theta_i)}|t|^2. \tag{4.64}$$

We also want to find the ratios of perpendicular over parallel for both transmitted and reflected to see how large of a difference there is to determine if it is worth worrying about. For transmitted, the ratio is

$$\frac{\perp'}{\parallel'} = \frac{2ncos(\theta_i)}{ncos(\theta_i) + \sqrt{n'^2 - n^2 \sin^2(\theta_i)}} \frac{n'^2 cos(\theta_i) + n\sqrt{n'^2 - n^2 \sin^2(\theta_i)}}{2nn'cos(\theta_i)} = \frac{n'cos(\theta_i) + \frac{n}{n'}\sqrt{n'^2 - n^2 \sin^2(\theta_i)}}{ncos(\theta_i) + \sqrt{n'^2 - n^2 \sin^2(\theta_i)}} \tag{4.65}$$

and for reflected, the ratio is

$$\frac{\perp''}{\parallel''} = \frac{ncos(\theta_i) - \sqrt{n'^2 - n^2 \sin^2(\theta_i)}}{ncos(\theta_i) + \sqrt{n'^2 - n^2 \sin^2(\theta_i)}} \frac{n'^2 cos(\theta_i) + n\sqrt{n'^2 - n^2 \sin^2(\theta_i)}}{n'^2 cos(\theta_i) - n\sqrt{n'^2 - n^2 \sin^2(\theta_i)}}. \tag{4.66}$$

4.11 Full Optical Path Simulation and Efficiencies

Now that we can predict how much power each beam will radiate depending on the beam properties it is important to know how much light we can actually detect. The entire optical path is many meters long. Before the light reaches the optics box there is a 45 degree elliptical mirror at each of the five elbows. The light then enters the optics box through a Wollaston prism. After the light is split into x and y polarizations it then reflects off two more mirrors inside of the optics box before finally hitting a ruled grating. None of these interactions are 100% efficient

therefore it is imperative to find all of the efficiencies so that we can use those and the initial light to find how much light reaches the end.

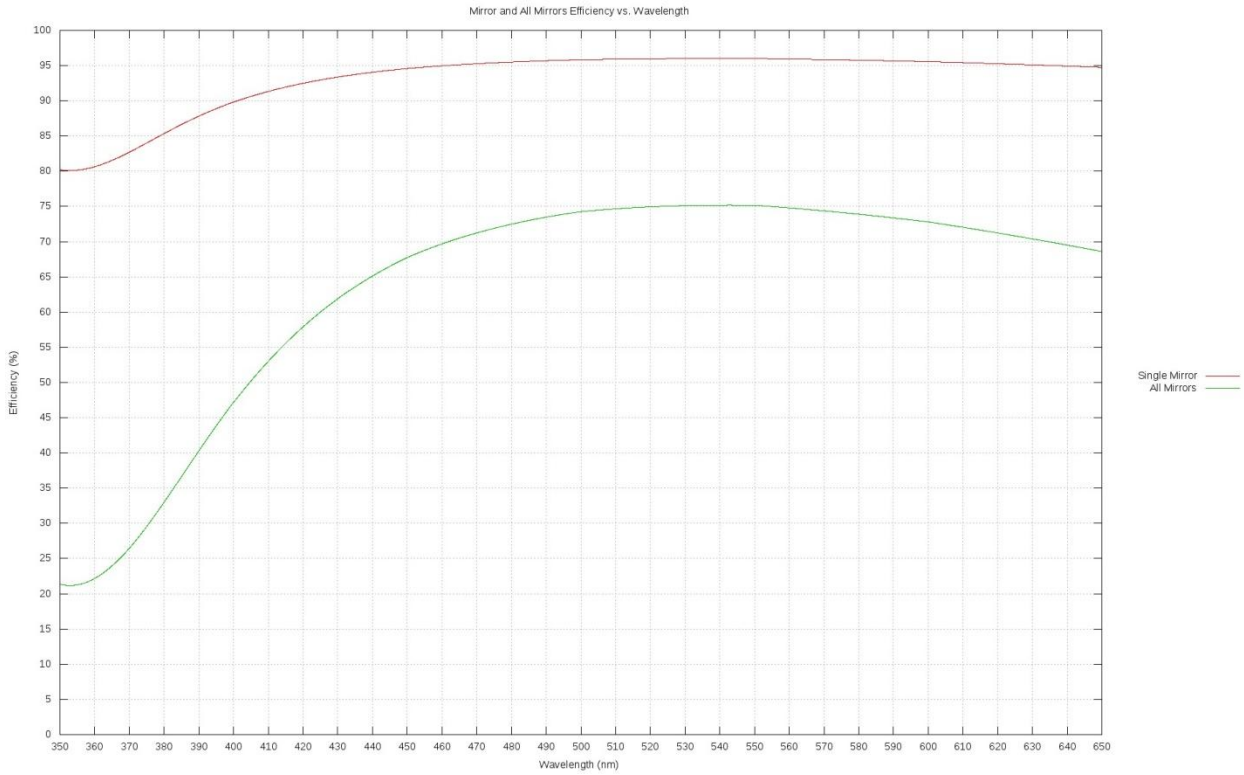

Figure 4.28: Mirror Efficiencies

The entire light path involves seven mirrors. Five of the mirrors are in the pipe path leading to the optics box and two of them are in the box itself. The red line of Figure 4.28 shows the efficiency of just one of the mirrors. All of the mirrors were extremely close to each other in efficiency therefore one mirror can represent all of them. The green line shows the efficiency of all seven mirrors combined.

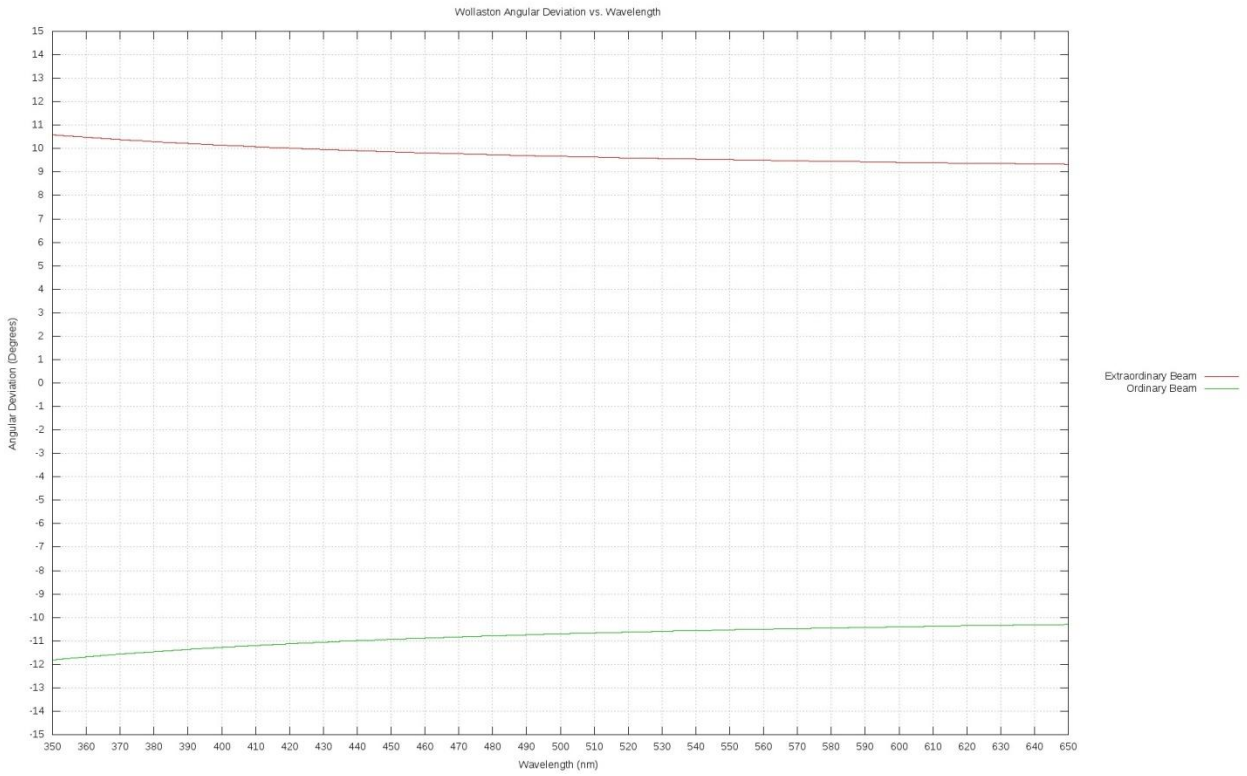

Figure 4.29: Wollaston Prism Beam Deviation

Once the light has travelled through the pipes and elbows with mirrors it reaches the optics box where it first passes through the Wollaston prism. The Wollaston prism separates the light into parallel and perpendicular polarizations at an advertised angle of $\pm 10°$ from the horizontal. However, it is not quite that simple. There is a dependence on wavelength as you can clearly see from the graph; it is not a flat line. Therefore we will have to take into account this initial spreading out caused by the Wollaston prism. To make matters even more complicated, the beam deviations are asymmetric between the two polarizations. Therefore, as evidenced in the asymmetric solution tables for each polarization, things will have to be arranged differently for each polarization to get the same light entering our PMT arrays. The red line is the parallel polarization beam deviation and the green line is the perpendicular polarization beam deviation.

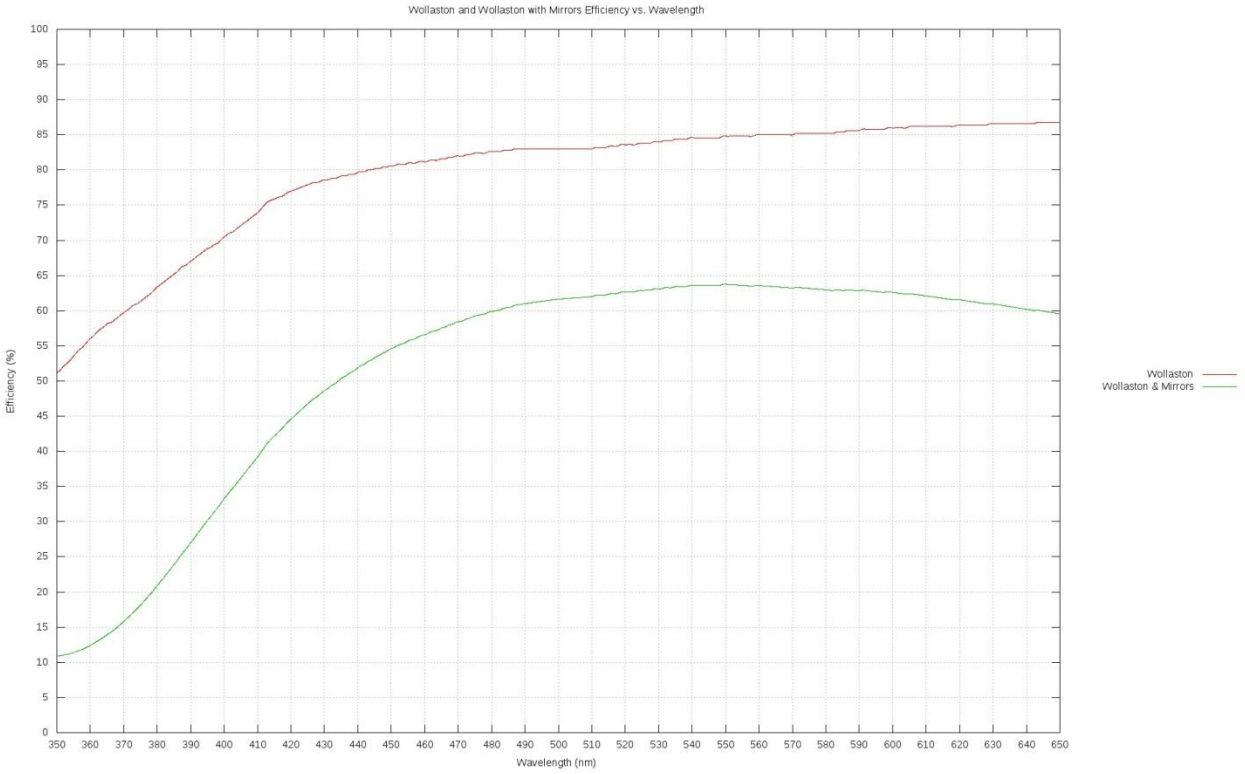

Figure 4.30: Wollaston Prism and Wollaston Prism with Mirrors Efficiencies

Besides the beam deviation issues, the Wollaston prism also has a wavelength varying efficiency as shown in Figure 4.30. The red line represents just the efficiency of the Wollaston prism whereas the green line is the combination of the Wollaston prism's efficiency and the efficiency of all seven mirrors combined.

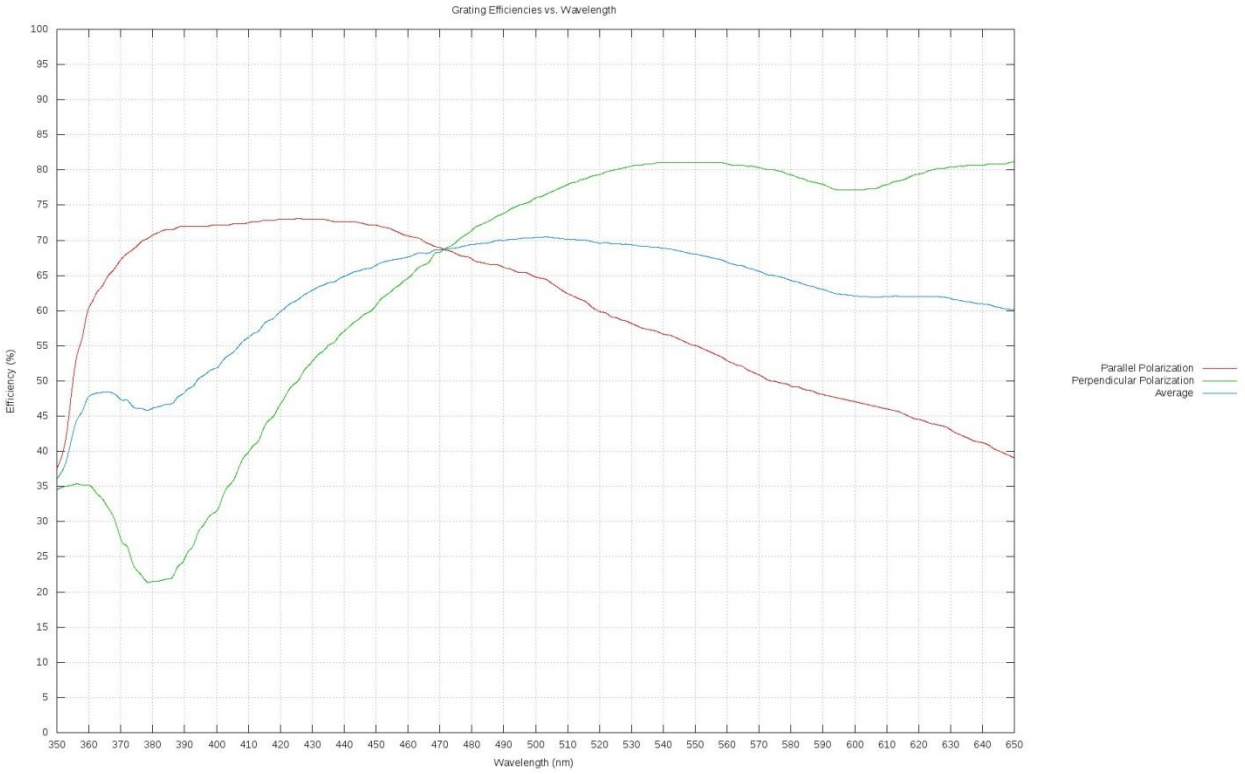

Figure 4.31: Grating Efficiencies

After the light leaves the Wollaston prism and reflects off the last two mirrors it comes to the reflective ruled grating. Remember, we have two different polarizations therefore they will have different efficiencies as shown in Figure 4.31. The red line is the grating's efficiency for parallel polarization, while the green line is the grating's efficiency for perpendicular polarization. The average efficiency between the two polarizations is shown by the blue line.

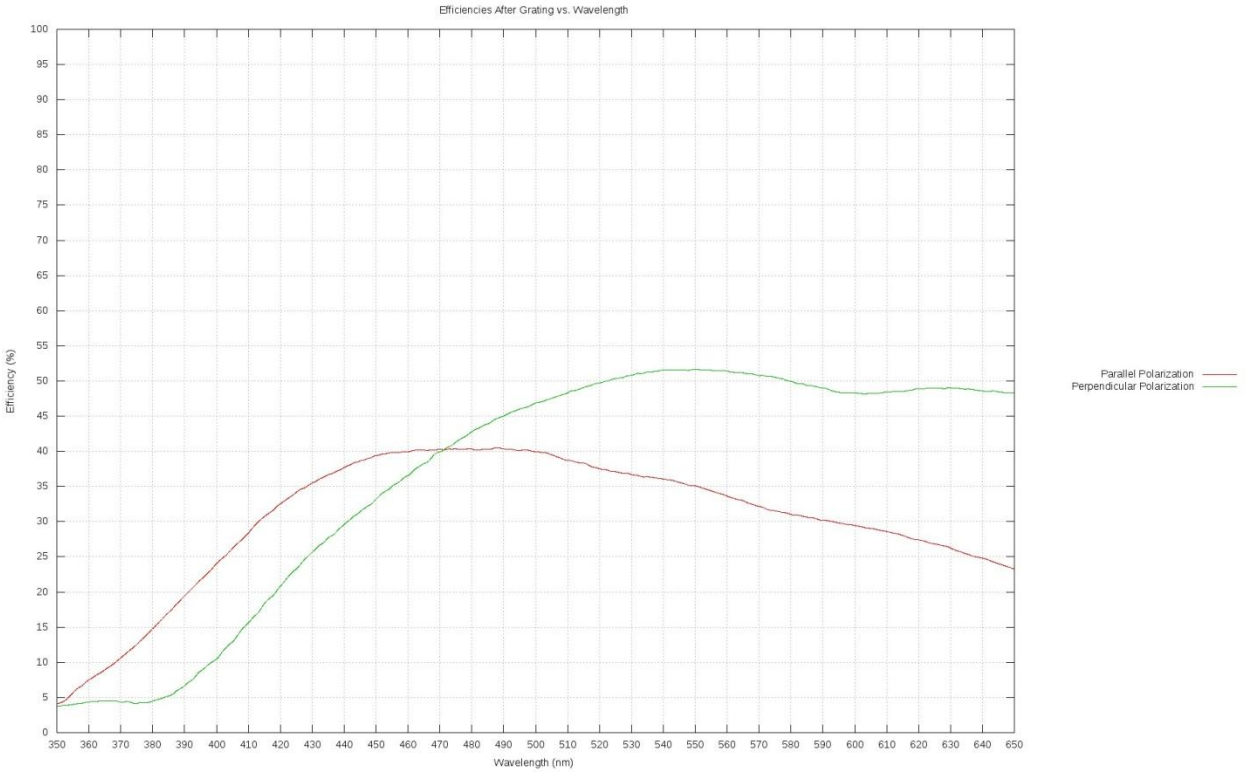

Figure 4.32: Efficiencies After the Grating for Both Polarizations

Figure 4.32 shows the combination of all seven mirrors, the Wollaston prism, and the grating efficiencies. The parallel polarization is in red and perpendicular polarization is in green. After the grating the light is then headed towards our prism-lenses however there are spaces between the prisms where some light will be lost. Remember, the light is not point like for each wavelength but instead a square therefore depending on the size of the gap a particular wavelength might lose only some of its power rather than all of it if it were completely in a gap. The easiest way to figure out the prism-lens acceptance was to find the ratio between the width of the beam that hits a prism face and the width of the beam in flight from the grating.

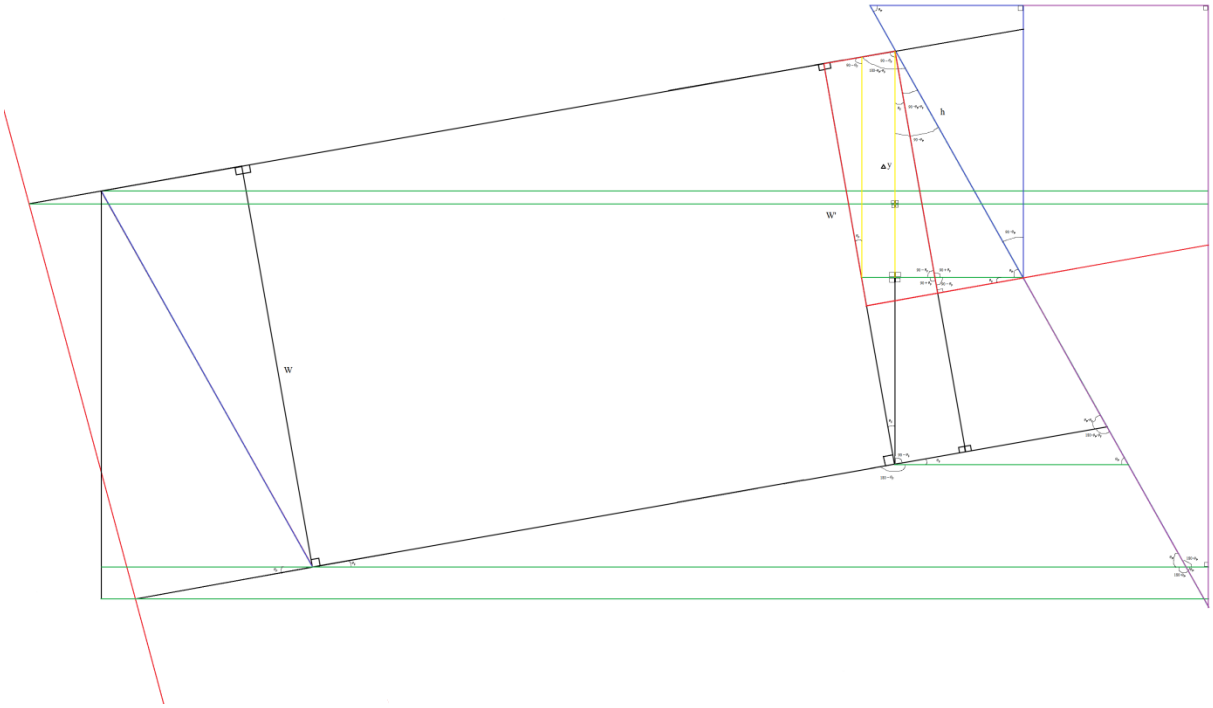

Figure 4.33: Positive Angle with Flipped Prism

There are four possible scenarios that can happen influencing the acceptance amount. First, the top and bottom of the square beam for a particular wavelength can be completely on a prism therefore the acceptance will be 100%. However, the top of the beam could be on a prism but the bottom of the beam could be in the gap between prisms therefore there will be a decrease in acceptance. Likewise, the bottom of the beam could be on a prism but the top of the beam could now be instead in the gap. Lastly, the top and bottom of the beam could span the gap and be partially on the prism above and below the gap. In our case, the gaps are small enough that this can happen.

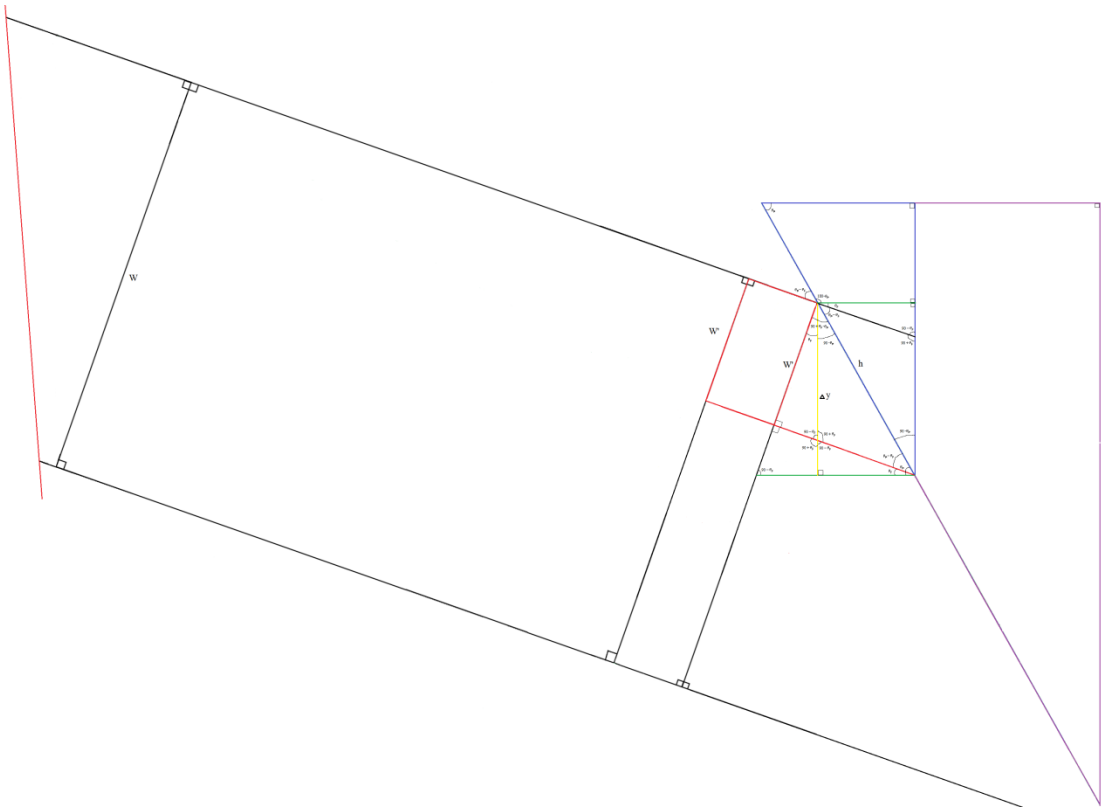

Figure 4.34: Negative Angle with Flipped Prism

The width accepted for a non-flipped prism is

$$w_a = hsin(\theta_p) - \theta_f \tag{4.67}$$

whereas for a flipped prism is

$$w_a = hsin(\theta_p) + \theta_f. \tag{4.68}$$

In these equations w_a is the accepted width, h is the hypotenuse the light makes when striking the angled surface of angle θ_p, and θ_f is the angle in our reference frame from the grating towards the prism.

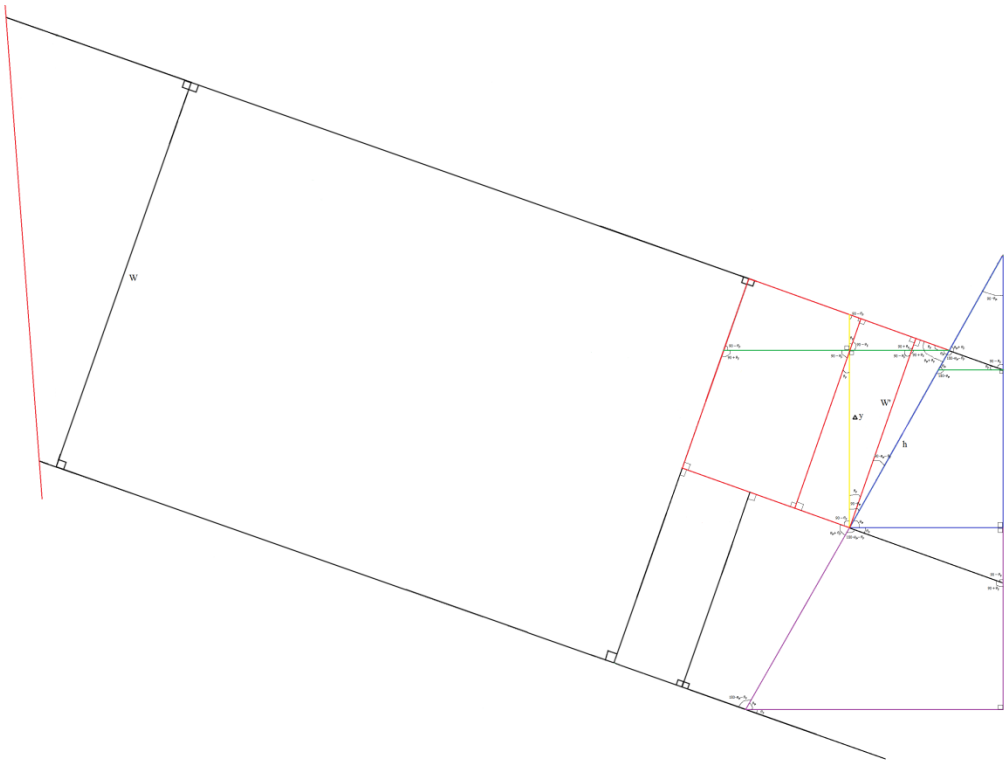

Figure 4.35: Negative Angle with Non-Flipped Prism

As can be seen with all of these arrangements in the last three figures, the equations remain the same except the reference frame angle changes sign when we flip the prism. When we divide this width with the width of the incoming beam of light that we found in Equation 4.8 and multiply by 100 we get the percent acceptance as shown in Figure 4.36. As you can see none of the wavelengths in our range ever lose all efficiency. The pattern appears to be alternating trapezoids which represent prism, gap, prism, gap, etc. The red line shows the parallel polarization and the green line is for the perpendicular polarization. As you can see they are not symmetrical because our asymmetry from the Wollaston prism was only exacerbated at every reflection leading to the greater than 5% discrepancies.

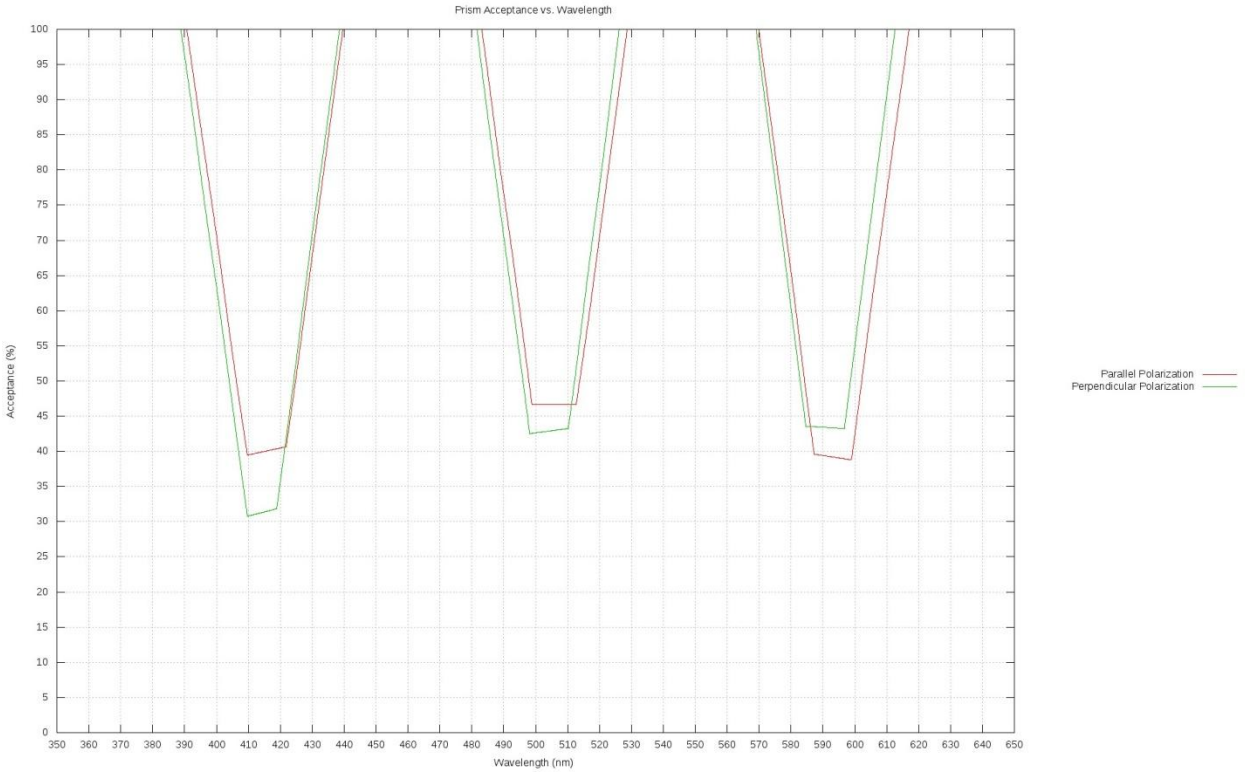

Figure 4.36: Prism-Lens Acceptance for Both Polarizations

Now that we know how much of the light actually makes it to the prism, we now have to find the efficiencies for all of the wavelengths in our range using the Equation 4.61 from the last section for each polarization. There are four transitions for the light from the start to the end of the prism-lens. Figure 4.37 shows the efficiencies at each interaction for the parallel polarization. The red line is for the air to prism transition and hovers in the mid 90s. The green line is for the prism to glue transition and the blue line is for the glue to lens transition and are virtually 100%. This is due to the extremely small difference between the index of refractions of the glass (1.55) and glue (1.56) and the very small angles of incidence. The purple line is for the lens to air transition and has a curved shape as expected for the curved side of the lens. The black line is the product of all of the efficiencies from start to finish.

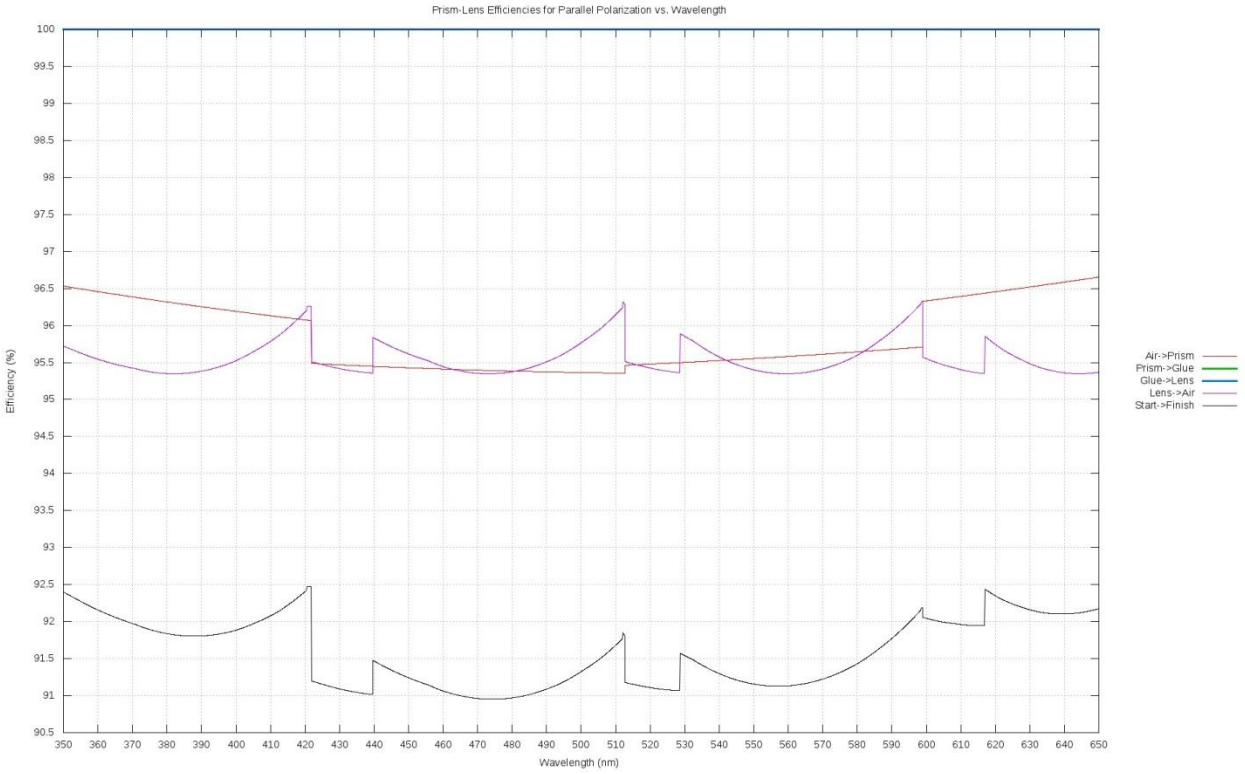

Figure 4.37: Prism-Lens Efficiencies for Parallel Polarization

Figure 4.38 shows the same efficiencies as above however for the perpendicular polarization instead. As you may notice the air to prism and lens to air efficiencies have been vertically reflected which is exactly what we would expect. Once again the black line is the product of all of the other efficiencies from the beginning of the prism-lens to the end.

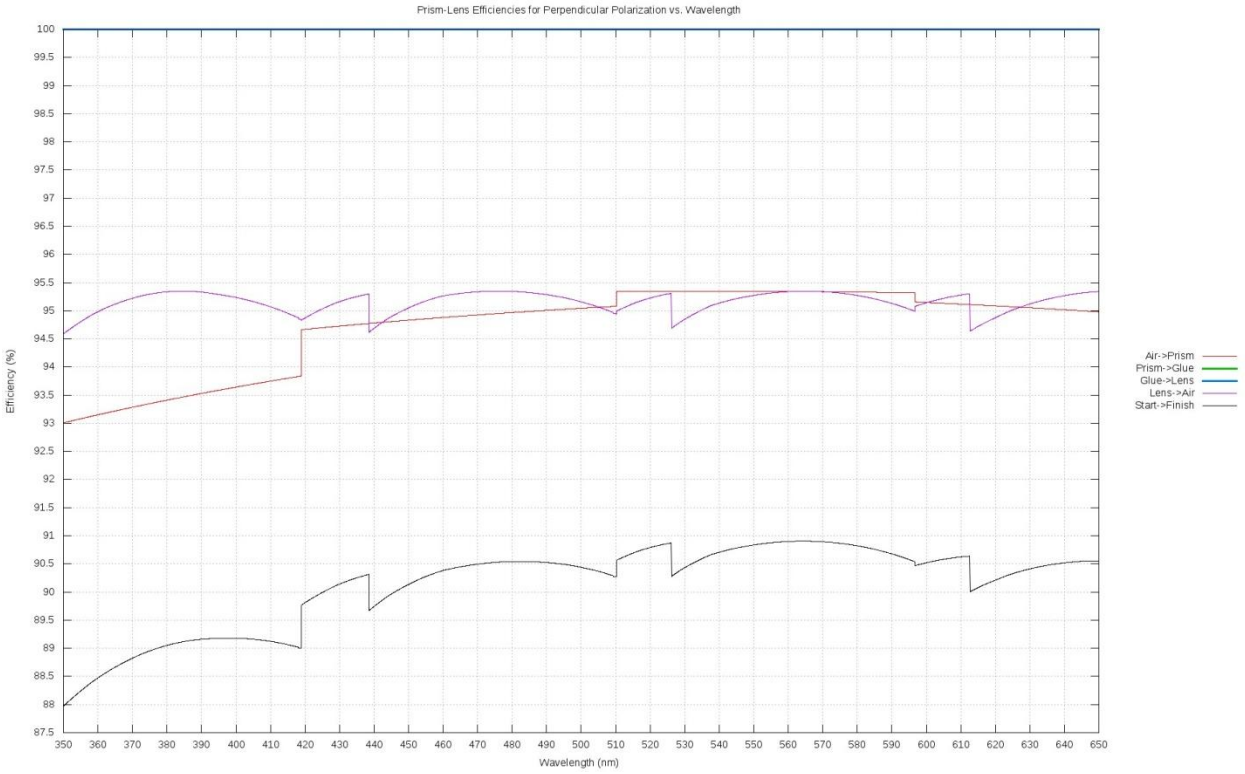

Figure 4.38: Prism-Lens Efficiencies for Perpendicular Polarization

Combining the start to finish efficiencies of the prism-lenses with the prism acceptances will give the true power dissipation for the prism-lens portion of our optical path. Combining this with the seven mirrors, Wollaston prism, and grating before the prism-lens will give you the efficiency of the whole system thus far which is shown in Figure 4.39. The parallel polarization is shown in red and the perpendicular polarization is shown in green. Notice, that for smaller wavelengths there is a far worse efficiency.

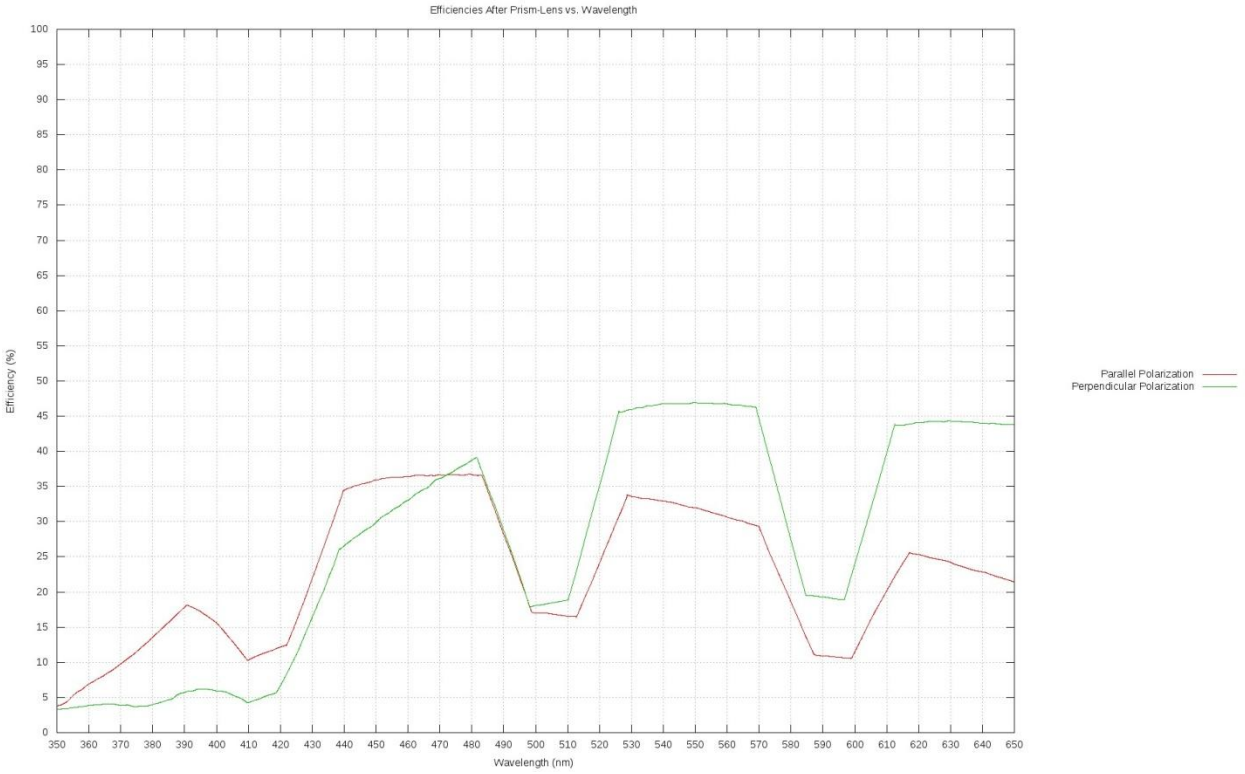

Figure 4.39: Prism-Lens Efficiencies for Both Polarizations

The last step in our journey is the array of photomultiplier tubes. Just like some of our other optical components the efficiency is not constant and can vary wildly for different wavelengths as shown in Figure 4.40.

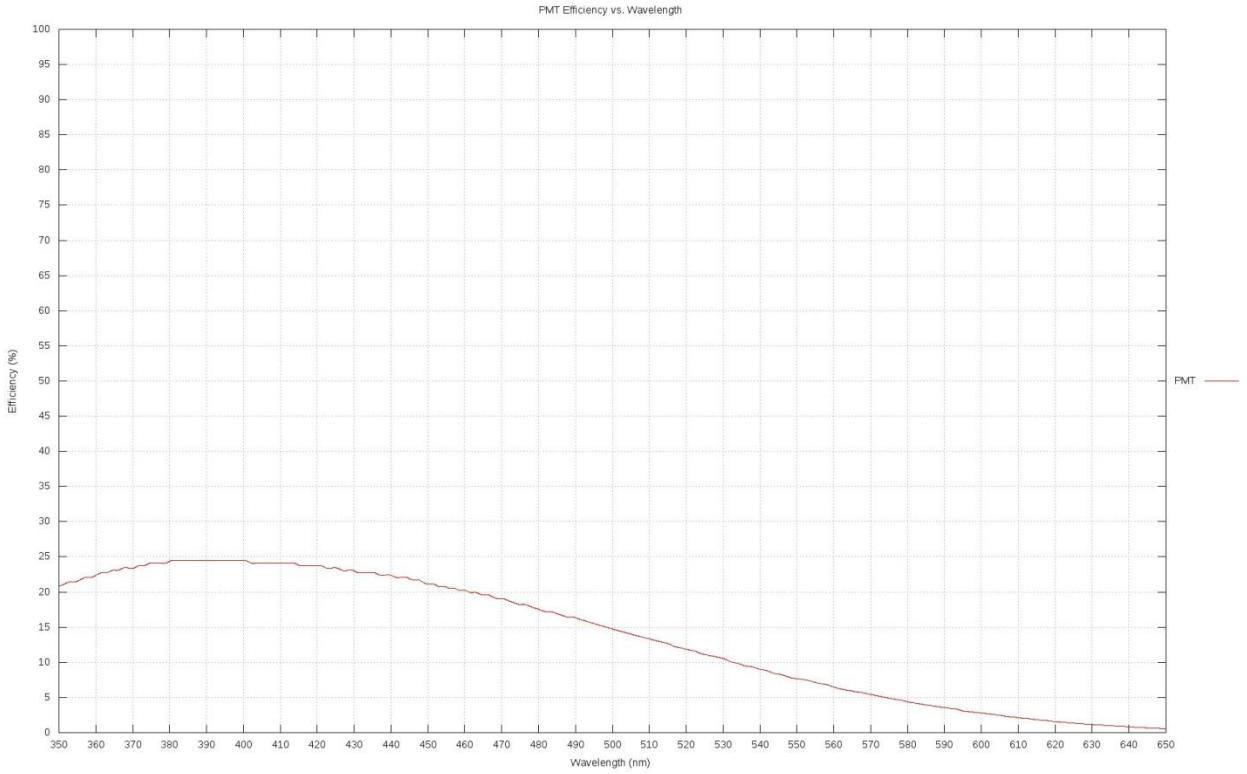

Figure 4.40: PMT Efficiencies

Finally we can combine the efficiencies of all of the components of our optical path into one total efficiency which is shown in Figure 4.41. The red line is for parallel polarization and the green line is for the perpendicular polarization. It would appear that we are in trouble since our total efficiency never even reaches 10% and for some wavelengths is far below that. However, the amount of light produced in the beam pipe is so intense that this factor of 10+ loss is beneficial for us so that we don't saturate our photomultiplier tubes or worse.

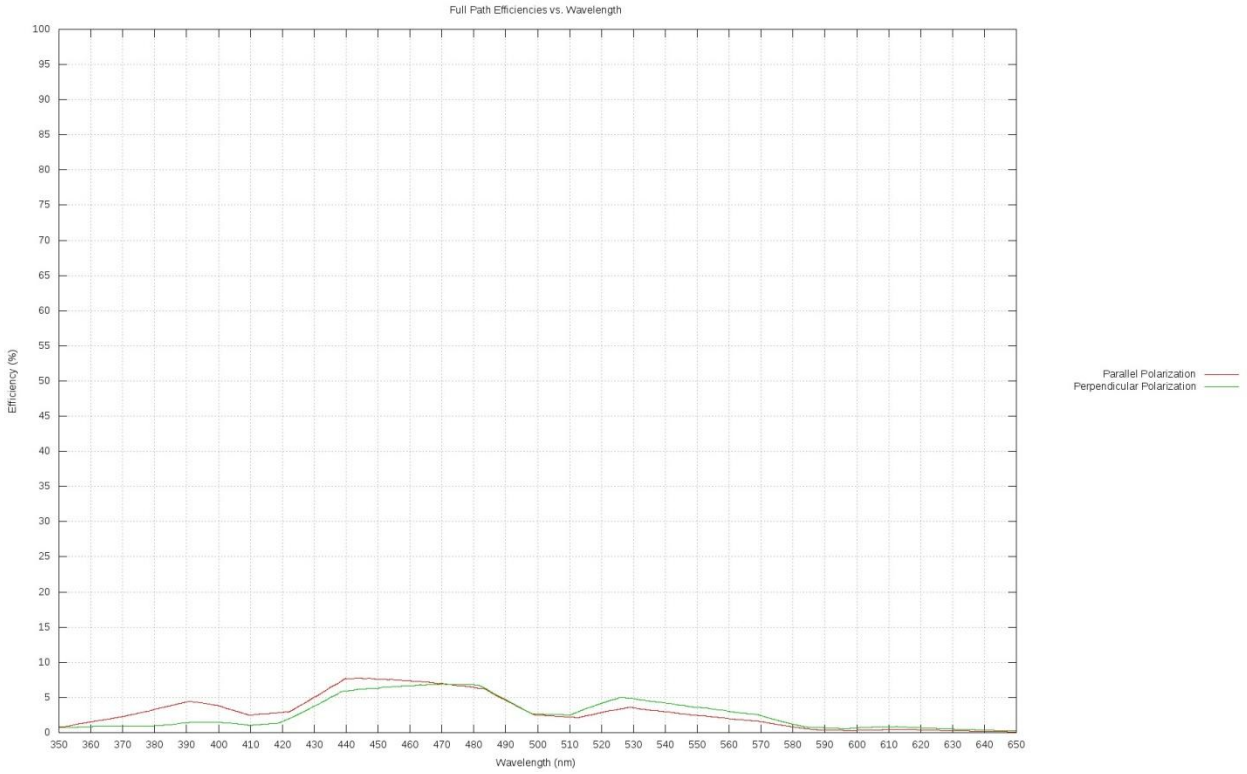

Figure 4.41: Full Path Efficiencies for Both Polarizations

We have completely simulated the entire light path inside of the optics box and know all of the positions of the optical components, their interaction points, and their efficiencies. Figure 4.42 shows exactly how our light will behave in the box for a chosen solution from the many in those solution tables. As I've said before you can see how the small asymmetry of the Wollaston prism gets larger and larger with each reflection, however our carefully chosen parameters for the mirrors and grating get the light correctly to the prisms for them to focus just the right way into the photomultiplier tubes. The simulation was very complex however it has provided valuable information on exactly how to arrange things in the box and the numbers to compare with.

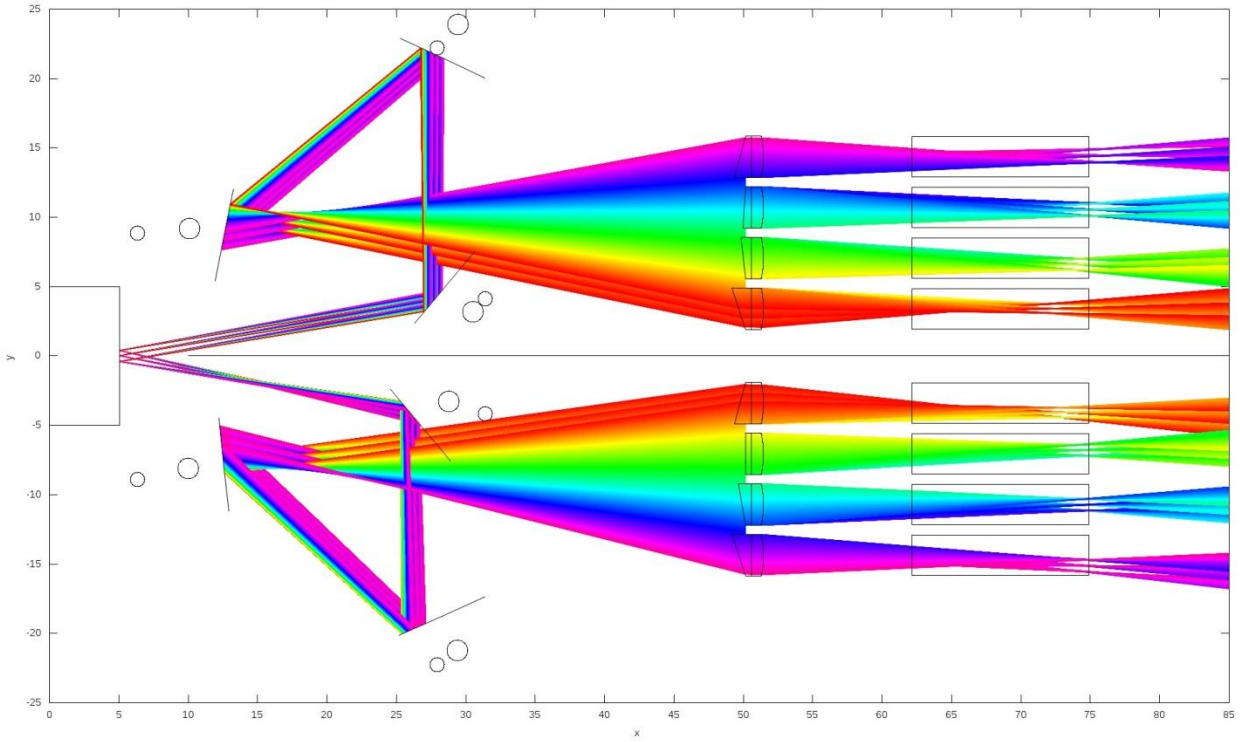

Figure 4.42: Optics Box Full Light Path

Chapter 5 : Conclusion

In our search for new physics it is crucial to maximize the chance for discovery. Therefore, luminosity optimization is of utmost importance so that we don't waste any opportunities. Our large-angle beamstrahlung monitor will be able to reconstruct the actual photon fluxes on the mirrors after collecting the spectral and polarization data at the end of the full optical path. With this being done in tandem with the results of our beamstrahlung simulations we will have a much better understanding of the beam collision geometry which remains elusive from other methods. Using this information to finely tune corrector magnets we will be able to setup an automatic feedback loop to make the collision geometry more ideal. This will lead to much better beam intersection, resulting in greater luminosity. With less luminosity being wasted due to these former imperfections there will be much more data with a higher probability of long sought after events and cutting edge physics.

At the conclusion of my research, we have two fully operational large-angle beamstrahlung monitors with associated piping paths (except for the connections to the beam pipe) that will be installed at KEK next year. Furthermore, we have detailed simulation software for many components of the full optical path as well as a working calculation for beamstrahlung due to beam collision imperfections which can all be used and added to during future research.

REFERENCES

[1] N. Cabibbo, *Physical Review Letters* 10 (12): 531533 1963

[2] S. L. Glashow, *Nucl. Phys.* 22:579, 1961

[3] S. Weinberg, *Phys. Rev. Lett.* , 19: 1264, 1967

[4] A. Salam, *Elementary Particle Theory*, N. Svartholm, ed., Stockholm: Almguist and Wiksell, 1968

[5] D.J. Gross, F.Wilczek, *Phys. Rev. Lett*, 30:1343, 1973

[6] H.D. Politzer, *Phys. Rev. Lett*, 30:1346 1973

[7] M.L. Perl *et al.*, *Physics Review Letters*, 35(22):1489, 1975

[8] J.Iliopoulos, L.Maiani, S.L. Glashow, *Phys. Rev. D*, 2:1285, 1970

[9] E. Noether, *Math. Phys.*, 235-257, 1918

[10] T. D. Lee and C.N. Yang, *Phys. Rev.* , 104:254-258, 1956

[11] C.S. Wu, E. Ambler, R.W. Hayward, D.D. Hoppes and Hudson, *Phys. Rev.* 105:4, 1957

[12] J. D. Jackson, Classical Electrodynamics, 2nd ed. (Wiley, New York, 1975)

[13] S.Y. Lee, Accelerator Physics, 3rd ed. (World Scientific, New Jersey, 2012)

[14] J.E. Augustin *et al.*, *Physical Review Letters*, 33(23): 1406, 1974

[15] J.J.Aubert *et al.*, *Physical Review Letters*, 33(23): 1404, 1974

[16] K. Nakamura *et al.*, *Journal of Physics*, 37(75021):150, 2010

[17] M. Kobayashi and T. Maskawa, *Progr. Theor. Phys.*, 49: 652-657, 1973

[18] M. Arinaga, J.W. Flanagan, H. Fukuma, H. Ikeda, H. Ishii, S. Kanaeda, K. Mori, M. Tejima, M. Tobiyama, G. Bonvicini *et al.*, *IBIC-2012-MOCB01*, 2013

[19] G. Bonvicini, D. Cinabro, E. Luckwald *Physical Review E 59*, 4584, 1999

[20] M. Bassetti et al., IEEE Trans. Nucl. Science 30: 2182, 1983

[21] M. Bassetti, G.A. Erskine, CERN-ISR-TH/80-06 (1980).

[22] G. Bonvicini *et al.*, *Phys.Rev.Lett.* 62:2381,1989

ABSTRACT

LARGE-ANGLE BEAMSTRAHLUNG: SIMULATION AND DIAGNOSTICS

by

RYAN S. GILLARD

May 2014

Advisor: Giovanni Bonvicini

Major: Physics

Degree: Doctor of Philosophy

Luminosity is paramount in high energy physics research, therefore it is critical to optimize it. Particle beams are complex and orbit in a complicated fashion therefore they don't always collide as intended thus reducing our chance of discovery. Simulations and calculations of the beam-beam radiation or beamstrahlung can provide crucial insight into the collision geometry. Combined with an optics box that can collect and analyze this radiation, this could be an extremely valuable tool leading to correction of the collision imperfections and greater discovery.

AUTOBIOGRAPHICAL STATEMENT

Name: Ryan S. Gillard

I was born in Warren, MI, USA on November 12th, 1986. I received a Bachelor of Science in Neuroscience from the University of Michigan-Ann Arbor in May 2009. I began my graduate studies in September 2009 at Wayne State University in Detroit, MI. I joined Prof. Giovanni Bonvicini's research group in May 2010. In the summer of 2012 I received my Masters of Science in Physics while continuing to work on my PhD.